PEOPLE'S DEMOCRATIC REPUBLIC OF ALGERIA
MINISTRY OF HIGHER EDUCATION AND SCIENTIFIC RESEARCH
FERHAT ABBAS UNIVERSITY – SETIF -1-

THESIS

Submitted to Institute of Optics and Precision Mechanics
For the degree

Doctorate 3rd Cycle -LMD
In Optics and Photonics
By

Lazhar LALAOUI

Title

Development and characterization of structures and materials applied in photovoltaics, and in photonics

Defended on: 17/11/2022 **In front of the composed committee of**

Chairman	**Aïssa Manallah**	**Professor**	**F.A.U Setif -1**
Supervisor	**Mohamed Bouafia**	**Professor**	**F.A.U Setif -1**
Co-Supervisor	**Saïd Bouzid**	**Professor**	**F.A.U Setif -1**
Examiner	**Bouzid Belloui**	**Professor**	**F.A.U Setif -1**
Examiner	**Abderrahmane Bouabellou**	**Professor**	**M.B.U Constantine-1**

Acknowledgment

This study was carried out with both the financial assistance of the Algerian Ministry of Higher Education and Scientific Research MESRS (**TASSILI Research Project 14MDU921**) France-Algeria and the financial assistance of **CIS-DAAD** Germany-Algeria.

I would like to thank many people for their help and support during the realization of this work.

My first and big appreciation goes to my first supervisor, Professor Mohamed Bouafia, for his marvelous supervision, guidance, and encouragement. Sincere gratitude is extended to his generous participation in guiding, constructive feedback, kind support, and advice. Thank you very much, Professor Mohamed Bouafia. Also, I greatly appreciate my second supervisor, Prof Said Bouzid for his excellent encouragement. Thanks a lot, you both.

My gratitude extends to the Institute of Optics and Precision Mechanics (**IOMP**)- Ferhat Abbas University Setif-1- for awarding me a dissertation completion fellowship, and providing me with the financial means to complete this project.

I would like also to thank the members of my dissertation committee: Professor Aïssa Mannallah (F.A.U Setif -1), Professor Bouzid Belloui (F.A.U Setif -1), and Professor Abderrahmane Bouabellou (M.B.U Constantine-1) - not only for their time and extreme patience, but for their interest in my work and the intellectual contributions to my development as a scientist.

I thank Prof. Dr. rer. nat. Stefan Krischok and Prof. Dr. Gerhard Gobsch for welcoming me to the institute of physics, Institute of Micro- and Nanotechnologies MacroNano®, University of technologies Ilmenau, Germany, and to CIS Research, institute for the micro-sensors GmbH in Erfurt, Germany as well. Thank you both for having initiated this project.

I would like also to extend my sincerest thanks to the whole staff in the department of Technical Physics-I, Dr. Dirk Schulze, Dr. rer. nat. Marcel Himmerlich, Anja Himmerlich, Dr. Anna Dimitrova, Dr. Stephanie Reiß, Annette Hartung, Katja Tonisch, and also in the Institut für Mikro- und Nanotechnologien MacroNano (**ZMN**) at Ilmenau Technical University for providing me with this opportunity to do this internship.
I would like to thank also the CiS Forschungsinstitut für Mikrosensorik und Photovoltaik GmbH Erfurt-Germany, for the preparation of samples (Black Silicon).

My appreciation also goes out to Professor Marc Lamy de la Chapelle and Dr. Nadia Djaker for welcoming me to the **CSPBAT** laboratory, University Paris 13, Thank you for sharing your knowledge of biophotonics with me, particularly through the correlation spectroscopy platform.

Special thanks must go to the members of my research team Dr. Aicha Medjahed and Dr. Dihia Isaadi for their kind collaboration and support throughout the project, from you all have been invaluable.

Last, but not least, my warm and heartfelt thanks go to my mother, my wife, family, and all friends for the tremendous support and hope they had given to me, thanks for all your support, without that hope, this work would not have been possible.

Thank you all for the strength you gave me.

Lazhar Lalaoui

Publications list

-Issaad, D., Medjahed, A., Lalaoui, L., et al. Refractive effects of the Gaussian beam on the volume confinement for fluorescence correlation spectroscopy: Experimental and numerical study. Optik-International Journal for Light and Electron Optics, 2017, vol. 145, p. 534-542.

-Issaad, D., Moustaoui, H., Medjahed, A., Lalaoui, L., et al. Scattering correlation spectroscopy and Raman spectroscopy of thiophenol on gold nanoparticles: comparative study between nanospheres and nano-urchins. The Journal of Physical Chemistry C, 2017, vol. 121, no 33, p. 18254-18262.

-Lalaoui, L., Bouafia, M., Bouzid, S., et al. Indoor and Outdoor Measurements of PV Module Performance of Different Manufacturing Technologies. In: International Conference on Electrical Engineering and Control Applications. Springer, Cham, 2017. p. 238-250.

-Lalaoui, L., Bouafia, M., Issaad, D., & Medjahed, A. Axial point spread function modeling by application of effective medium approximations: Widefield microscopy. Optik-International Journal for Light and Electron Optics, 2020 .164646.

Figure list

Table list

Abbreviation list

ALD: Atomic Layer Deposition

APD: Avalanche Photodiode

AR: Antireflection

ARC: Antireflection Coating

B.E: Binding Energy

BP: Bio-Photonics

BSi or **B-Si:** Black Silicon

CCD: Charge-Coupled Device

CCP: Capacitive Coupled Plasma

CLSM: Confocal Laser Scanning Microscopy

DRIE: Deep Reactive Ion Etching

EDX: Energy-Dispersive X-ray Spectroscopy

Eg: Energy gap in [eV]

EMA: Effective Medium Approximation

EMT: Effective Medium Theory

EQE: External Quantum Efficiency

FCS: Fluorescence Correlation Spectroscopy

FWHM: Full Width at Half Maximum

IC: Integrated Circuits

ICP-RIE: Inductively Coupled Plasma Reactive Ion Etching

IR: Infra-Red

LPCVD: Low-Pressure Chemical Vapor Deposition

MCEE: Metal-Catalyzed Electroless Etching

MEMS: Micro-Electro-Mechanical Systems

NA: Numerical Aperture

NIR: Near-Infrared wavelength

OAG: Oxide Assisted Growth

OPD: Optical Path Difference

PL: Photoluminescence

PSF: Point-Spread Function

PV: Photovoltaic

REM: Reflection Electron Microscopy

RF: Radio Frequency

RI: Refractive Index (indices)

SE: Spectroscopic Ellipsometer

SEM: Scanning Electron Microscopy

SERS: Surface-Enhanced Raman Spectroscopy

UV-Vis: Ultraviolet-Visible

VIS: Visible

VLS: Vapor-Liquid-Solid growth

WFM: Wide-field Microscope

XPS: X-Ray Photoelectron Spectroscopy

XRD: X-Ray Diffraction

Table of content

B- Theoretical part

Chapter I – Photovoltaic materials

Chapter II– Biophotonic materials

C- Experimental Part

Chapter III– Photovoltaic materials

Chapter IV– Effective medium for biophotonics

Introduction and state-of-the-art

Due to the enormous progression in the materials domain and the overlapping of many technological domains, the characterization techniques have a great development too [1–3]. In this context, a systematic study of materials fields has been carried out. Photovoltaic (black silicon solar cells) and biophotonic (fluorescent molecules and microspheres) materials are the focus area of this thesis whose characterizations are at the nanometric scale.

The characteristics of the materials from which photovoltaics solar cells are made are intimately linked to their performance, and many materials science issues are encountered in studying existing solar cells and developing more efficient, less expensive, and more stable cells. A material is said to be "photovoltaic" when the exposure of the material to light can be absorbed and this latter is able to transform this energy of light photons into electrical energy in the form of current and voltage. The concept is simple, and the variety of materials able of producing photovoltaic characteristics is enormous. As long as silicon is the most widely used semiconductor in microelectronic (especially solar cells) and many other fields. However, silicon surfaces have high natural reflectance of around 30% to 40 % in the visible range which reduces the efficiency for applications such as photovoltaic devices and sensor photodetectors [4]. At this stage, the black silicon fabricated by ICP-RIE [5–7] could offer a solution that combines both broadband AR properties and strong near bandgap light trapping. The increased surface area of BSi requires the ability to cover conformally the pits or walls of nanostructure with a high aspect ratio. This is extremely challenging for most thin film deposition methods. It is well known that only Atomic Layer Deposition ALD method, can uniformly coat each pit over the surface of the black silicon. Therefore, coating of BSi with Alumina Al_2O_3 or Al:ZnO by ALD would be the ideal approach to realize the surface passivation.

Black or Grass Silicon is a Nano-scale surface modification formed by self-organizing processes in plasma etching. It can be actively used to enable new functionalities or enhance the performance of Micro-Electro-Mechanical-Systems (MEMS), Biological MEMS (BioMEMS) or Micro-Opto-Electro-Mechanical-Systems (MOEMS). Its low-cost generation with standard fabrication equipment makes it a promising research subject, which still is time-consuming and only applicable to monocrystalline material.

Black silicon is very attractive for use in a variety of applications as a sensitive layer of the photodetector [3], solar cells [3,8–10], field emission [8,11], and luminescence [3,12], and other photoelectric devices. Other applications include enhanced Raman scattering [13] and even anti-bacterial surfaces as biological applications [2].

During the last decades, bioimaging is a major axis of biophotonic materials characterization that provides microscopic, high sensitivity, and resolution information of a wide range of biological specimens (from cells to tissues) [14–16], which various optical techniques have been developed a single-molecule detection level. To achieve the full potential of biophotonic technology, the availability of suitable optical materials is of crucial importance, as their optical properties, mechanical properties, chemical structures, and biological functionalities significantly affect the device's performance [17–19]. The Fluorescence correlation spectroscopy FCS was first proposed by Magde *et al.* in 1972, which is a powerful tool for detecting molecular dynamics through analyzing the intensity fluctuation emitted by biomolecules diffusing in and out of a focused light [15,20]. The local concentration, hydrodynamic radius, diffusion coefficient [21], local temperature [22], etc. can be accurately measured with FCS [13,23]. Compared with other dynamics-orientated approaches, FCS has a broader measurable time range spanning practically from nanoseconds to second, and a higher sensitivity that can be up to a single-molecule level.

It is the purpose of the present thesis to characterize effective media (nanomaterial), and materials (nanostructure) applied in photovoltaic, photonic, and biophotonic. Afterward, in order to better organize the study and outline a better research methodology, the whole work was divided into two parts as follows:

Photovoltaic part a collaboration has been planned between the Department of Technical Physics I at the University of Ilmenau in Germany and the Institute of Optics and Precision Mechanics University of Ferhat Abbas Setif -1- in Algeria.

The work project revolves on analytical methods for study the optical properties such as absorbance, reflectance, dielectric properties (refractive index, extinction coefficient, thickness), structural (needle size, high aspect ratios, roughness, interface defects, conformal coatings), and electronic (electronic band structure, crystal orientation, and chemical composition) of black silicon samples «Silicon grass» fabricated by inductively coupled plasma reactive ion etching "ICP-RIE" with regard to solar cell applications. Hence, an investigation of the influence of the deposited thin films (transparent conductor oxide TCO), which were grown on highly doped p-Si (100) and n-Si (100) black silicon respectively by atomic layer deposition (ALD), and then, characterize their morphologies by means available at the host laboratory at Institute of Physics, Institute of Micro-and Nanotechnologies MacroNano®, Technische Universität Ilmenau.

Biophotonic part this work section is part of an inter-university collaboration project called "*TASSILI*" between the university of Paris, France and the University of Ferhat Abbas Setif -1- in Algeria, financed by the EIGIDE organization.

This part starts with investigation of two different methods (known and unknown solution's concentration) to determine the optical effective detection volume from fluorescence correlation spectroscopy measurements of diluted fluorophore solution (Alexa Fluor) and then compared their results by the effective volume resulting from fluorescent microsphere imaging with applying the point spread function PSF (optical system calibration). The basic principle, implementation schemes, and data analysis of the FCS versus PSF are first elaborated.

Secondly, the applications of FCS in chemistry and biology are described by applying quantitative parameters derived from an autocorrelation curve to deduct the local temperature in viscous solutions.

Finally, the biophotonic part that focused on widefield microscope imaging of fluorescent microparticles and characterization of non-homogeneous media by applying the theory of effective media adopted with the PSF model of Gibson and Lanni and its effect on the resolution as a simulation part has been done.

Within this framework, the thesis contains three chapters:

The first chapter consists of a description of the materials applied in photovoltaic field and different techniques to improve their photonic performance.

A second chapter is dedicated to introduce the photonic/biophotonic materials and different characterization techniques used focused on the FCS and PSF technique.

A third chapter started the experimental study for the two fields of photovoltaics and biophotonics.

The manuscript concludes with a review of the results obtained, highlighting the relevance of the different nanostructure characterization technique and also fluorescence spectroscopy a wide-field microscopy in the study of biophotonic materials characterization of the optical system itself, and medium too.

References

[1] S.-T. Yang, L. Cao, P.G. Luo, F. Lu, X. Wang, H. Wang, M.J. Meziani, Y. Liu, G. Qi, Y.-P. Sun, Carbon Dots for Optical Imaging in Vivo, J. Am. Chem. Soc. 131 (2009) 11308–11309. https://doi.org/10.1021/ja904843x.

[2] P.W. May, M. Clegg, T.A. Silva, H. Zanin, O. Fatibello-Filho, V. Celorrio, D.J. Fermin, C.C. Welch, G. Hazell, L. Fisher, A. Nobbs, B. Su, Diamond-coated 'black silicon' as a promising material for high-surface-area electrochemical electrodes and antibacterial surfaces, J. Mater. Chem. B. 4 (2016) 5737–5746. https://doi.org/10.1039/C6TB01774F.

[3] J. Lv, T. Zhang, P. Zhang, Y. Zhao, S. Li, Review application of nanostructured black silicon, Nanoscale Research Letters. 13 (2018) 1–10.

[4] M. J. McCann, K. R. Catchpole, K. J. Weber, A. W. Blakers, A review of thin-film crystalline silicon for solar cell applications. Part 1: Native substrates, Solar Energy Materials and Solar Cells. 68 (2001) 135–171. https://doi.org/10.1016/S0927-0248(00)00242-7.

[5] X. Liu, P.R. Coxon, M. Peters, B. Hoex, J.M. Cole, D.J. Fray, Black silicon: fabrication methods, properties and solar energy applications, Energy Environ. Sci. 7 (2014) 3223–3263. https://doi.org/10.1039/C4EE01152J.

[6] S. Leopold, C. Kremin, A. Ulbrich, S. Krischok, M. Hoffmann, Formation of silicon grass: Nanomasking by carbon clusters in cyclic deep reactive ion etching, Journal of Vacuum Science & Technology B: Microelectronics and Nanometer Structures. 29 (2011). https://doi.org/10.1116/1.3521490.

[7] M. Kroll, T. Käsebier, M. Otto, R. Salzer, R. Wehrspohn, E.-B. Kley, A. Tünnermann, T. Pertsch, Optical modeling of needle like silicon surfaces produced by an ICP-RIE process, in: Photonics for Solar Energy Systems III, SPIE, 2010: pp. 36–45. https://doi.org/10.1117/12.854596.

[8] J.S. Yoo, I.O. Parm, U. Gangopadhyay, K. Kim, S.K. Dhungel, D. Mangalaraj, J. Yi, Black silicon layer formation for application in solar cells, Solar Energy Materials and Solar Cells. 90 (2006) 3085–3093. https://doi.org/10.1016/j.solmat.2006.06.015.

[9] Y. Xia, B. Liu, J. Liu, Z. Shen, C. Li, A novel method to produce black silicon for solar cells, Solar Energy. 85 (2011) 1574–1578. https://doi.org/10.1016/j.solener.2011.03.012.

[10] C.-H. Hsu, J.-R. Wu, Y.-T. Lu, D.J. Flood, A.R. Barron, L.-C. Chen, Fabrication and characteristics of black silicon for solar cell applications: An overview, Materials Science in Semiconductor Processing. 25 (2014) 2–17. https://doi.org/10.1016/j.mssp.2014.02.005.

[11] C. Langer, C. Prommesberger, R. Ławrowski, R. Schreiner, P. Serbun, G. Müller, F. Düsberg, M. Hofmann, M. Bachmann, A. Pahlke, Field emission properties of p-type black silicon on pillar structures, Journal of Vacuum Science & Technology B. 34 (2016) 02G107. https://doi.org/10.1116/1.4943919.

[12] A. Serpengüzel, A. Kurt, I. Inanc, J.E. Cary, E.D. Mazur, Luminescence of black silicon, JNP. 2 (2008) 021770. https://doi.org/10.1117/1.2896069.

[13] R.F. Peters, L. Gutierrez-Rivera, S.K. Dew, M. Stepanova, Surface enhanced Raman spectroscopy detection of biomolecules using EBL fabricated nanostructured substrates, J Vis Exp. (2015). https://doi.org/10.3791/52712.

[14] D. Issaad, H. Moustaoui, A. Medjahed, L. Lalaoui, J. Spadavecchia, M. Bouafia, M.L. de la Chapelle, N. Djaker, Scattering Correlation Spectroscopy and Raman Spectroscopy of Thiophenol on Gold Nanoparticles: Comparative Study between Nanospheres and Nanourchins, J. Phys. Chem. C. 121 (2017) 18254–18262. https://doi.org/10.1021/acs.jpcc.7b05355.

[15] E.L. Elson, D. Magde, Fluorescence correlation spectroscopy. I. Conceptual basis and theory, Biopolymers. 13 (1974) 1–27. https://doi.org/10.1002/bip.1974.360130102.

[16] A. Polman, M. Knight, E.C. Garnett, B. Ehrler, W.C. Sinke, Photovoltaic materials: Present efficiencies and future challenges, Science. 352 (2016) aad4424. https://doi.org/10.1126/science.aad4424.

[17] Introduction to Biophotonics, in: Biophotonics, WORLD SCIENTIFIC, 2017: pp. 1–11. https://doi.org/10.1142/9789813235694_0001.

[18] J.L. West, N.J. Halas, Engineered nanomaterials for biophotonics applications: improving sensing, imaging, and therapeutics, Annu Rev Biomed Eng. 5 (2003) 285–292. https://doi.org/10.1146/annurev.bioeng.5.011303.120723.

[19] D. Issaad, A. Medjahed, L. Lalaoui, M. Bouafia, M.L. de la Chapelle, N. Djaker, Refractive effects of the Gaussian beam on the volume confinement for fluorescence correlation spectroscopy: Experimental and numerical study, Optik. 145 (2017) 534–542. https://doi.org/10.1016/j.ijleo.2017.08.049.

[20] A. Goetzberger, C. Hebling, Photovoltaic materials, past, present, future, Solar Energy Materials and Solar Cells. 62 (2000) 1–19. https://doi.org/10.1016/S0927-0248(99)00131-2.

[21] C. Cruickshank Miller, The Stokes-Einstein Law for Diffusion in Solution, Proceedings of the Royal Society of London Series A. 106 (1924) 724–749.

[22] S. Ito, T. Sugiyama, N. Toitani, G. Katayama, H. Miyasaka, Application of Fluorescence Correlation Spectroscopy to the Measurement of Local Temperature in Solutions under Optical Trapping Condition, J. Phys. Chem. B. 111 (2007) 2365–2371. https://doi.org/10.1021/jp065156l.

[23] M. Martinez-Moro, D. Di Silvio, S.E. Moya, Fluorescence correlation spectroscopy as a tool for the study of the intracellular dynamics and biological fate of protein corona, Biophysical Chemistry. 253 (2019) 106218. https://doi.org/10.1016/j.bpc.2019.106218.

CHAPTER I

Photovoltaic materials

Chapter I – Photovoltaic materials

1. Background

Photovoltaics, which directly converts solar energy into electricity, offers a practical and sustainable solution to the meeting challenge of the increasing global energy demand. Most materials used in photovoltaic devices are usually silicon (monocrystalline, polycrystalline, or amorphous),

The latest advancements in photovoltaic materials have led to an overall efficiency increase. Although we know from solid-state physics that silicon is not the ideal material for photovoltaic conversion, a significant portion of the thesis will be about it. Only photons with energy from the bandgap can be absorbed with high efficiency by a semiconductor, but the photons with lower energy are not absorbed [1]. Whereas higher-energy photons are reduced to the energy gaps by thermalization. As a consequence, the curve of efficiency versus bandgap goes through a maximum (**Fig.I.1**). It can be seen that silicon is not at the maximum but it is near. The Shockley–Queisser limit (also known as the detailed balance limit, Shockley Queisser Efficiency Limit or SQ Limit, or in physical terms, the radiative efficiency limit) is the theoretical maximum efficiency of a solar cell that used a single p-n junction to collect power from the cell, with radiative recombination as the only loss mechanism [2,3].

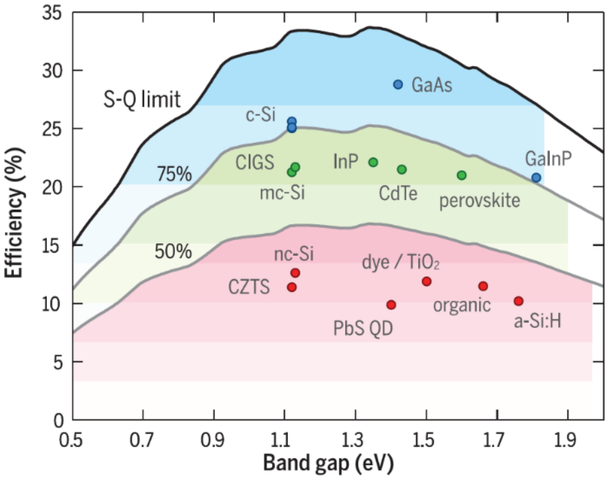

Fig.I.1- Conversion efficiency of solar cell materials versus bandgap for single-junction cells [2].

It is not surprising that a great deal of effort has been and continues to be expended in the search for new materials. The requirements for the ideal solar cell material are:

- Bandgap between 1.1 and 1.7 eV.
- Direct band structure.
- Consisting of readily available, nontoxic materials.

- Easy, reproducible deposition technique, suitable for large area production.
- Good photovoltaic conversion efficiency
- Long-term stability.

Silicon has a high natural reflectance of more than 30%; this high reflectance and the large bandgap of 1.12 eV severely restrict the applications of silicon-based photon sensitive devices and the full use of the spectrum. Moreover, the high reflectance across the electromagnetic spectrum seriously affects the efficiency and sensitivity of optoelectronic devices based on silicon. With high absorptance in visible and infrared wavelengths.

In 1996 Eric Mazur "a physics professor at Harvard University in Cambridge", Massachusetts, and several of his graduate students discovered a material they later called black silicon [4]. The group placed a silicon wafer in a vacuum chamber, filled it with chalcogen-containing gas, and irradiated the silicon with ultrashort pulses from a femtosecond laser. Upon examination, the team discovered the blackened surface was covered with a vast array of nanoscale spikes.

This altered material was announced to the world at the American Physical Society Centennial meeting in 1999 in Atlanta, Georgia. In 2003, Mazur and his team built the first black silicon photodetector [5]. Additional black silicon testing revealed a substantial absorption of incoming light with wavelengths ranging from 400 to 2500 nm. In 2006, Mazur and Harvard University graduate student James Carey launched SiOnyx with the goal of exploiting black silicon to improve the infrared sensitivity of silicon-based photodetectors and image sensors in low-light and night-vision applications. Compared to the traditional silicon, the energy band structures of black silicon have been changed, which is beneficial to be used as photoluminescence. As black silicon fabricated with fs lasers is covered with sharp conical micro-spikes arrays, it can be used as field emitters further and in visible- infrared photodetectors, solar cells and night vision cameras as well [3].

I.1 Aspect of silicon and black silicon

I.2.1 Generalities

Silicon (Si) is a semiconductor which is defined as a material whose resistivity is intermediate between that of conductors and that of insulators [6,7]. Silicon is insulator at the temperature of 0 Kelvin. When the temperature rises, under the effect of the thermal agitation, electrons manage to escape and participate in the conduction. This conduction refers to the electrons located on the furthest layer of the nucleus that are involved in the covalent bonds. As all solids, the interaction of atoms and electrons in the lattice disrupts the discrete electronic energy levels of each atom to move them and bring them together in quasi-continuous electronic energy bands, the symmetry of which depends of the crystal lattice [8].

I.2.1.1 Silicon properties

Silicon and gallium arsenide with its related III-V compounds are the most commonly used semiconductor materials. However, silicon dominates the microelectronics industry with around 90% of all semiconductor devices sold worldwide made from silicon. Silicon possesses two of the most outstanding natural dielectrics, silicon dioxide (SiO_2) and silicon nitride (Si_3N_4), which are essential for device formation. Silicon is a semiconductor material with the indirect band gap of 1.12eV (**Fig.I.2**) [9,10].

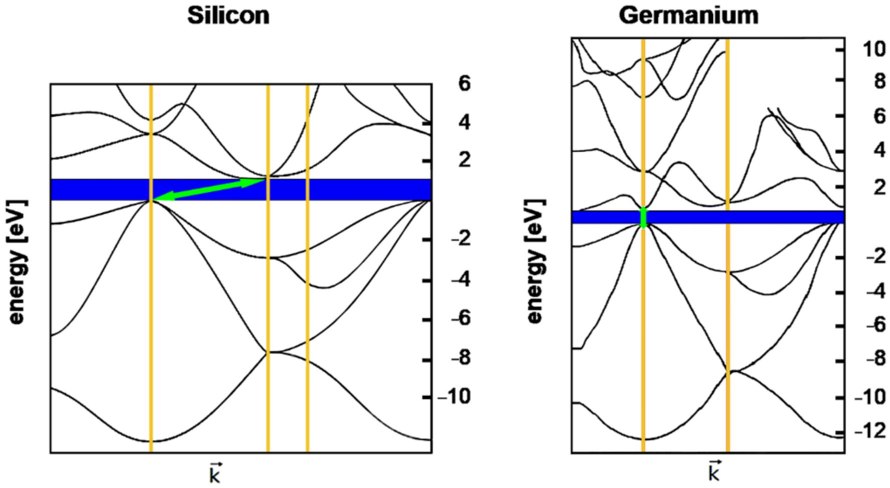

Fig.I.2- Silicon energy band structure [11].

The interaction between a photon and a semiconductor is generally explained by an important characteristic of the material; this characteristic is the absorption coefficient shown in the (**Fig.I.3**). This optical property was measured at 300 K. Silicon can absorbs wavelengths from 400 nm to 1100 nm. For short wavelengths the absorption coefficient of silicon is very high, the energy of photons is much more high than the indirect silicon gap (Eg = 1.12 eV, λ = 1.1 µm) [10,12].

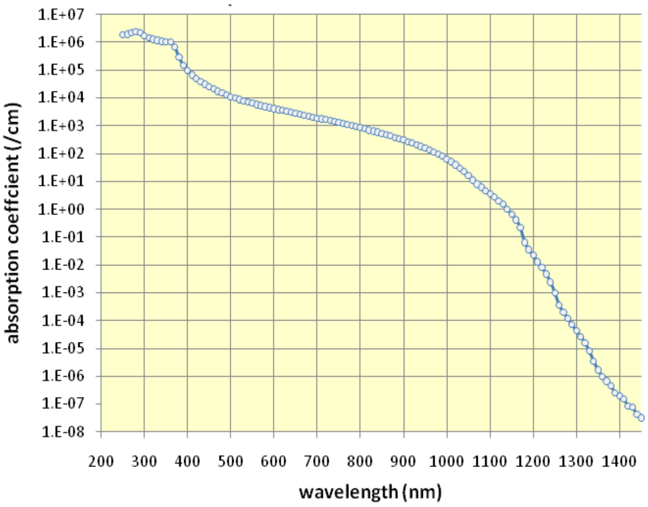

Fig.I.3-The absorption coefficient of silicon as function of the wavelength (from 200 to 1400 nm) [13].

However, the reduction of the reflection of these layers is effective only over a limited spectral range. Another way of reducing reflection is surface texturing, which is one of the most effective techniques to reduce silicon reflectance surface over wide band [12]. In our study, we focus on the alternative solution (silicon surface texturing with micro/nano structures) which results from the material called "Black Silicon" and then we are interested in improving its efficiency by the first solution (ARC) to reduce optical losses.

I.2.1.2 Nanostructured silicon

Silicon characterized by its indirect band gap at room temperature; therefore, it has low optical efficiency. Silicon nanostructured is one of the most effective solutions not only to get new properties compared to traditional silicon, but also to increase the sensitivity and the optical efficiency due to the quantum confinement effect. Surface texturing for enhanced absorption in Silicon has been historically obtained by creating randomly distributed pyramids using anisotropic etchants [9]. This permanent and lasting technique consists in the creation of µ-sized structures on the surface of silicon wafers. These structures are able to trap incident light (**Fig.I.4**) until it is absorbed, reducing the optical power lost by reflection at the silicon – air interface, due to multiple reflections of the incident light and, therefore, to a more efficient light absorption in the silicon volume [10].

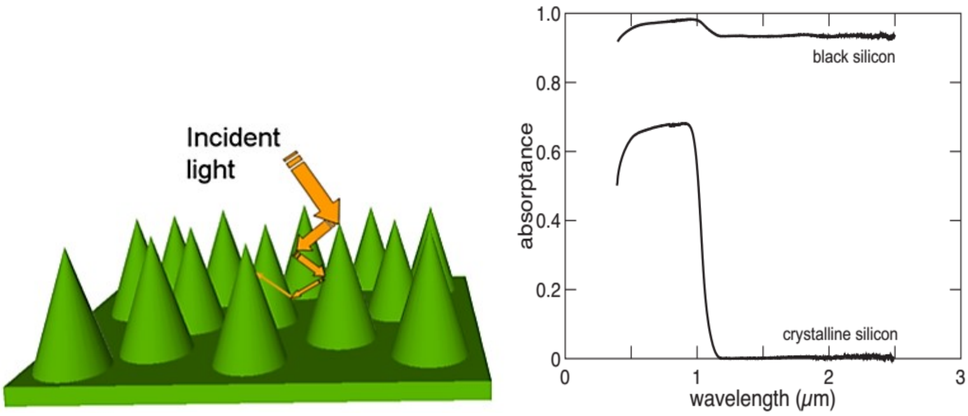

Fig.I.4 - (Left) Schematic representation of silicon microstructures illustrating the multiple reflection of incident light. (Right) Absorptance (in VIS-NIR) [9].

The nanostructed surface can act as a region with a graded index of reflection between air and the dielectric material, possessing a prosperous reflectance reduction in a broader spectral bandwidth and omnidirectional incidence [14]. The nanostructuration of silicon makes it possible to envisage the use of several types of nanostructures, such as thin layers (2D), nanowires (1D), quantum dots (0D) and results in a black surface to the naked eye, hence the name "**Black Silicon**" (BSi) [15,16].

The (sub-) micro textured silicon surface can be formed in various shapes (spikes, "penguin-like" structures, columns, and pyramids). BSi is now recognized as an antireflective layer both in visible and infrared ranges; hence, it attracted attention for numerous applications, including solar cells, improved VIS-IR photodetector, light emitting devices, etc [9]. In the following part, we will take a deeper look at BSi, its properties, morphology, methods and techniques of fabrication.

I.2.2 Black silicon

The term "black silicon" actually dates back at least to the 1980s as a generic term for describing high-aspect-ratio features formed on the surface of silicon [17]. Black silicon is a name given to the silicon surface whose optical performances have been improved by forming structures (surface modification) in various geometries on micro or nano-sizes to increase the absorption of the photons coming to the surface and reduce the amount of reflection [18]. However, the BSi presents a solution which is used as an alternative anti-reflection (AR), instead of anti-reflection coating (ARC). It has been applied to a wide range of applications, such as micro-electro-mechanical systems (MEMS), optoelectronic and photonic devices [16] .

I.2.2.1 Properties of black silicon

BSi possesses a few unique and attractive properties not found in traditional silicon making it an ideal candidate material for many applications. The main feature of BSi is the increased absorption of the incident light compared to traditional silicon (**Fig.I.4**). The enhanced absorption of black silicon is owing to the light trapping effect of surface morphology and energy level of dopants. The absorption in the range from 1100 nm to 2500 nm is also enhanced due to the doping of chalcogen elements [18]. Another important feature of black silicon is the low reflectivity. However, the high reflectivity of silicon which ranged from 30% to 40% for quasi normal incidence, is reduced to less than ~10% (crystalline silicon) [19]. Whereas, in textured amorphous silicon, it may be decreased to ~1% [20]. This is due to the formation of a so-called effective medium [21] by the nanostructured silicon surface. Within this medium, there is no sharp interface, but a continuous change of the refractive index that reduces Fresnel reflection. **The Effective Medium Theory** (EMT) predicts that a 200–300 nm thick textured graded index layer is sufficient to almost completely suppress the reflectance across the whole solar spectrum (above the silicon bandgap) [22]. Both, the energy levels of dopants and structural defects create more intermediate states to enhance the sub-band gap absorption of silicon. Compared to traditional silicon, the energy band structures of black silicon have been changed which is beneficial to be used as photoluminescence [23].

Besides the high absorption and the low reflectivity of this altered material, BSi eventually characterized by its high sensitivity of light includes the infrared wavelengths (low photon energy) that silicon usually does not absorb. Actually, Black silicon is one of the biggest trends in photovoltaic manufacturing due to the increased efficiency of the optical-electrical conversions [5].

I.2.2.2 Morphologies

Morphology could be succinctly described as the study of a given structure’s form, such as its dimensions in terms of widths, heights, or angles. However, with regard to nano-scale structures, morphology is not simply a mundane cataloguing of the physical properties of shape and size; it can dictate very strongly the optical, electrical, and chemical properties of structures (wettability, transport, and index of refraction for example). It is quite evident that such additional properties of nano-scale structures, in contrast to those of large substrates, would be strongly connected to form, as such structures are achieved often by self-assembling processes governed by the interaction of the atomic and molecular arrangement of deposited materials, precise location of sputtered or passivated material, and directional nature of chemical bonds, with resultant structures measured on scales not entirely different than those of the interactions which created them [24]. Black silicon is a material that is chemically equal to traditional silicon. The difference between them is the surface treatment that changes the morphology. This special morphology has to represent a certain roughness of the surface. The structure of the black silicon depends on the parameters already mentioned above, and also depends on the technical and the manufacturing conditions (pressure, temperature, duration, etc.) and we can distinguish several forms of black silicon (spikes, “penguin-like” structures, columns, pyramids, conical, and needles, etc.) [9,25].

I.2.2.3 Fabrication methods of B-Si

Over recent decades, significant progress has been made in the development of facile methods to create black silicon with controlled diameter, length and electronic properties. In principal, there are two approaches for preparing BSi, i.e., Bottom-up and top-down approaches presented in (**Fig.I.5**) [26].

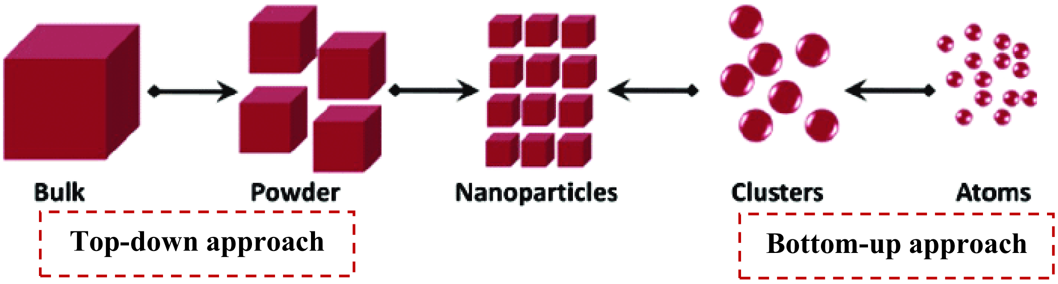

Fig.I.5-Bottom-up and top-down approaches [27].

The bottom-up approach is assembly process joining Si atoms to form nanoparticles and to create black silicon. This approach includes Vapor-Liquid-Solid (VLS) growth, oxide assisted growth (OAG), solution-based growth, and supercritical-fluid-based. The bottom-up approach can readily grow BSi with diameter ranging from ~ 5 nm to hundreds of nanometers, and length varied from ~ 100 nm to 10µm. On the other hand, the top-down approach prepares BSi via dimensional reduction of bulk silicon by lithography and etching. Electron beam lithography, reactive ion etching

(RIE), and newly developed metal-catalyzed electroless etching (MCEE) of Si are widely used to fabricate black silicon with dimensions ranging from tens to hundreds of nanometers. In general, the top-down methods have difficulty in production of black silicon with diameter below 10 nm [26].

As already mentioned, a wide variety of techniques employed to fabricate black silicon, but the focus on this work is not neither the production of black silicon, nor the comparison between these different methods, only one technique (**RIE),** which used in the fabrication of the three examined samples on this study, will be described in the following.

I.2.2.3.1 Reactive ion etching (RIE)

RIE is a plasma-based etching method used in integrated circuits (IC) and micro-electro-mechanical systems (MEMS), where the ions generation and acceleration towards the wafer are controlled with the same radio frequency (RF) power source. During etching, the sample is placed in the enclosure of the frame RIE. Dry etching of locally masked silicon is carried out aluminium or silicon oxide and this etching can be performed using a plasma sulfur hexafluoride (SF_6), and oxygen (O_2), as shown in the (**Fig.I.6**). In SF_6/ O_2 plasma, SF_6 will produce fluorinated radicals F^* which will react with the silicon atoms to form volatile compound SiF_4. So, silicon will etch by SF_6 according to the reaction below:

$$Si + 4F^* \rightarrow SiF_4$$

Simultaneously, the fluorinated radicals react with the silicon by forming SiF_x sites on its surface, which then react with the oxygen radicals O* for the formation of sidewall passivation layers SiO_yF_x. This passivation layer plays a very important role in the BSi formation. The mechanism of formation of SiO_xF_y molecule can be proposed as follows:

$$Si + xF^* \rightarrow SiF_4$$

$$SiF_x + yO^* \rightarrow SiO_yF_x$$

Indeed, the presence of oxygen determines the formation of the passivation layer SiO_yF_x, and this layer is essential for the BSi formation. In addition, this passivation layer is formed only at cryogenic temperatures and it is volatile at room temperature. That is why it is essential to operate at cryogenic temperatures to obtain black silicon [9,28].

During the silicon etching with/without mask, spikes will be formed depending on the degree of isotropy of the etching.

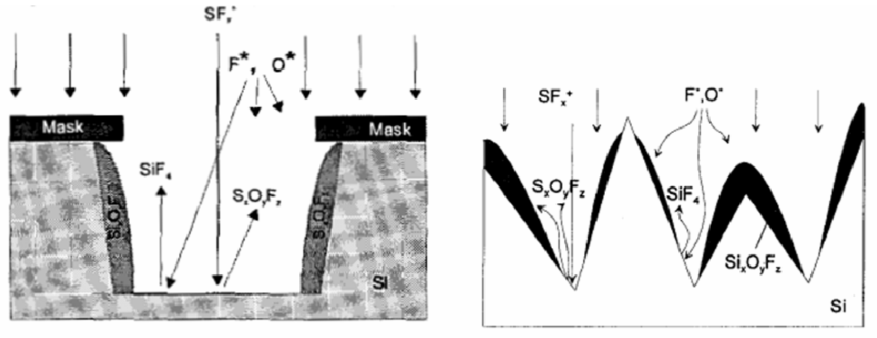

Fig.I.6-Silicon etching mechanism process by SF_6/O_2 plasma with [10]
and without black silicon mask [28].

There are several parameters that influence the process, such as pressure, temperature [29], electrical power, bias voltage, SF_6 and O_2 flow rates, and etching time [10,30–32]. For example, Jinsu Yoo et al. [31,33] studied the role of the SF_6/O_2 ratio in conditions where a smallest average reflectance was obtained with a SF_6/O_2 ratio of 2.8 and etching rate corresponding of the order of 300 nm/min (**Fig.I.7**).

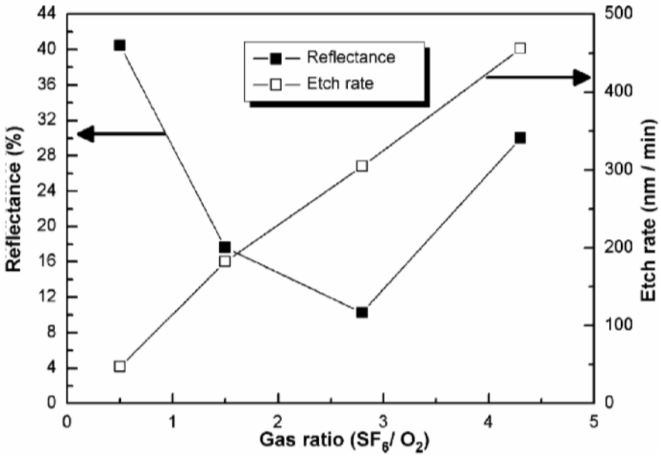

Fig.I.7-Average reflectance and silicon etch rate according to the ratio SF_6/O_2 [32-33].

Deep reactive ion etching (DRIE) is a technique based on the same principle of reactive ion etching process. Only, it uses two sources of plasma: ICP (inductively coupled plasma) for the production of high-density plasma, and CCP (capacitive coupled plasma) to control ion energy. By this technique, we can obtain a deeper etching, a speed higher etching (up to 32 µm/min), and high aspect ratio (thickness/width). There are mainly two types of DRIE process cryogenic process and Bosch process. The Bosch silicon etching process is often used in DRIE technique for the manufacture of directional profiles.

It is a room temperature process of two steps: the passivation step, followed by the etching step. Octafluorocyclobutane C_4F_8 gas is well suited for passivation in high-speed directional etching. Bosch is process with mask. In the cryogenic DRIE process, the passivation occurs simultaneously with the etching, which performed in SF_6/O_2 plasma. The profile of the pattern is therefore smoother than that obtained by the Bosch process. It is possible to adjust the parameters of the DRIE process cryogenic to obtain the desired etching profiles [34]. RIE-ICP is the process used in this thesis to fabricate the three black silicon samples. Cryogenic DRIE is a maskless process.

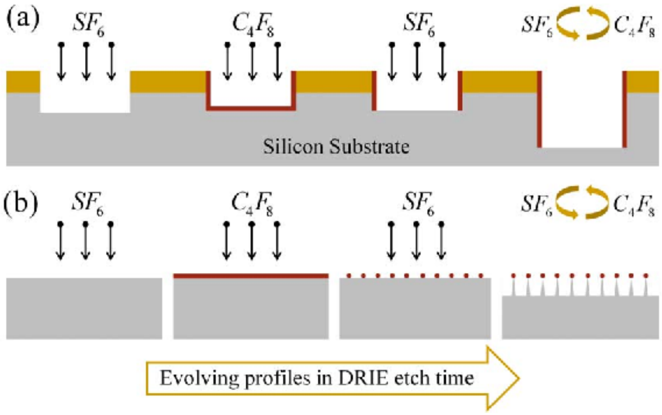

Fig.I.8-Schematic illustration of black silicon formation: (a) The Bosch silicon etching process, (b) the cryogenic DRIE process (optimized process) [35].

I.3 Applications of black silicon

The large bandgap and the high surface reflectance of bulk silicon restrict the full use of the spectrum; black silicon is one of the best methods to solve this problem. It is extensively the most efficient and very attractive for using as a sensitive layer of photodiodes, solar cells, field emission, luminescence, and other photoelectric devices [3,31,36,37].

I.3.1 Photodiodes

Black silicon can be used in traditional junction photodetector architecture. The measured quantum efficiency near the infrared wavelength (NIR) spectrum is over 10 times incumbent than traditional silicon photodetectors [38]. Black silicon generated by laser irradiation, especially with sulphur doping, is useful in many different applications. For example, BSi produced in SF_6 environment are luminescent upon annealing, and the luminescent wavelength can be modified by the annealing temperature. The improved photo-responsivity makes it ideal photodiode material [15].

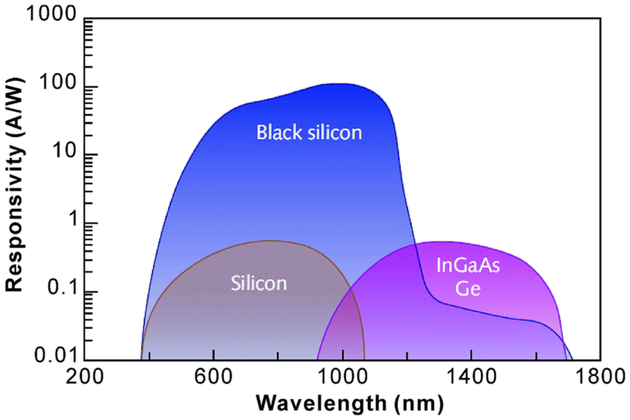

Fig.I.9-The responsivity of a BSi photodiode in comparison to those of standard silicon, InGaAs and Ge [15].

Fig.I.9 shows that photodiodes made of n-type BSi demonstrate a higher responsivity (in visible and near infrared range) than commercially available silicon photodiodes [15]. **Fig.I.10** shows an example of photodiode based on black silicon, normal-incidence Ge-on-Si photodiodes with 300 nm thick intrinsic Ge absorber layer and black silicon light-trapping are fabricated and analyzed with regard to their responsivity. Compared to a standard Ge-on-Si photodiode without black silicon, the black silicon device exhibits a 3 times increased responsivity of 0.34 A/W at 1550 nm and enhances of Ge absorptance by a factor of up to 10 (depending on the wavelength and Ge thickness) while simultaneously preserving the relatively simple architecture and fabrication of normal incidence detectors. By that, the problematic bandwidth-responsivity trade-off in ultrafast Ge-on-Si detectors can be widely overcome. The black silicon light-trapping structure can be applied to the device rear during back-end processing.

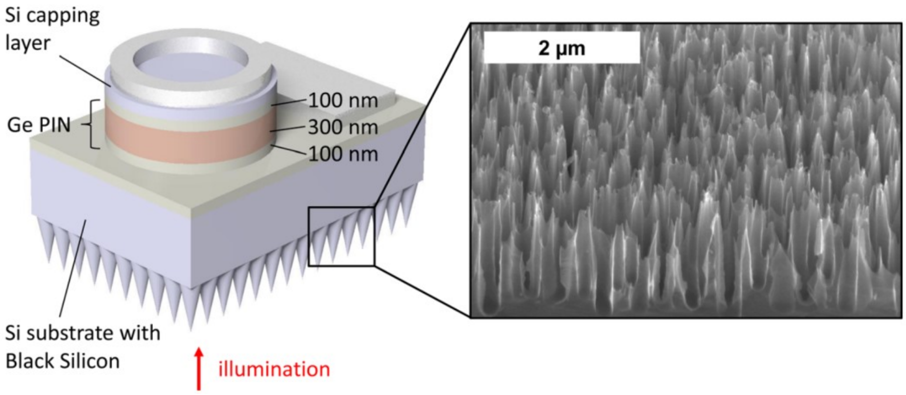

Fig.I.10- Scheme of the investigated black silicon Ge-on-Si photodiode (PIN structure of the device) [39].

Black silicon nanostructures are fabricated by Inductively Coupled Plasma Reactive Ion Etching (ICP-RIE) for light-trapping in underlying Ge films. The current-voltage characteristics of the fabricated black silicon Ge-on-Si photodiode in the dark and under illumination at 1550 nm are displayed in the (**Fig.I.11**).

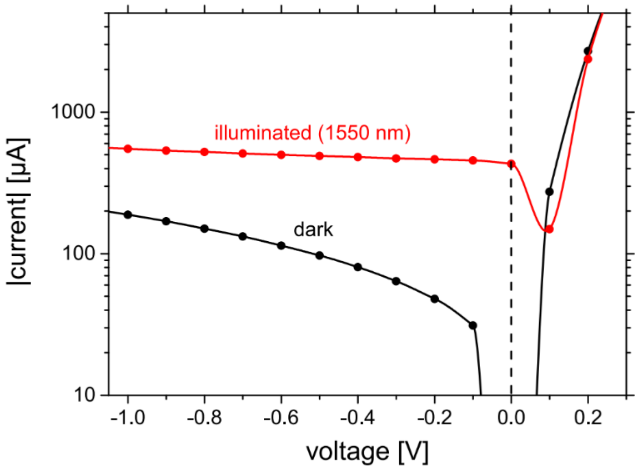

Fig.I.11- Characteristics of Ge-on-Si photodiode with black silicon in the dark and under illumination (1550 nm): Unhindered photocurrent extraction in reverse and at 0 V is distinct [39].

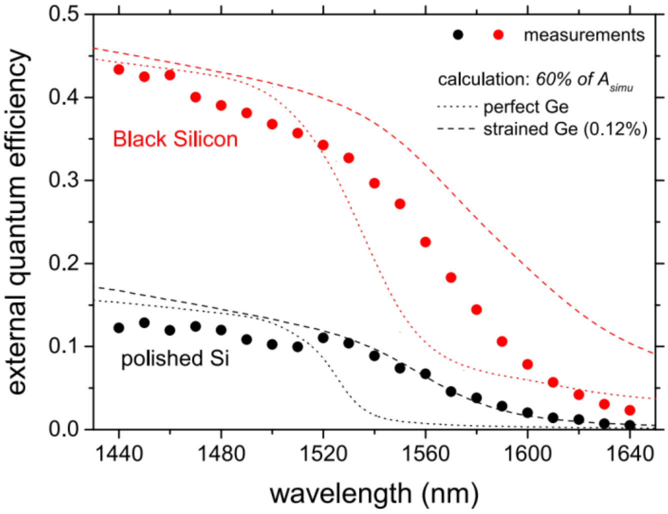

Fig.I.12- Measured EQE spectra of Ge-on-Si photodiode with and without black silicon light-trapping (dots) at 0V For comparison, also the theoretical absorptance spectra for perfect and strongly strained Ge (0.12%), scaled by a factor of 60% (to account for the limited photocurrent collection efficiency), are displayed (broken lines) [39].

M. Steglich et al. [39] have shown that the application of black silicon does not increase the dark current of the device, and the dark current density of the black silicon surfaces is equals that of the unstructured surfaces. They have shown also that, apparently, there is a strong enhancement of the external quantum efficiency (EQE) by utilization of black silicon at the light facing rear side of the detector. In fact, the EQE is raised by a factor of 3 at the shorter wavelengths to 4 at longer wavelengths where the Ge absorption gets gradually weaker (i.e., k > 1550 nm).

I.3.2 Solar cells

The unusual photoelectric characteristics, combined with these semi-conducting properties of silicon make black silicon one of the biggest trends in photovoltaic manufacturing. The unique light-trapping effect of micro-textured surface morphology greatly enhances the visible absorption of silicon, making it well used in Vis-NIR photodetection, as well as solar cells. In particular, these nanostructures as antireflection layer increase the surface area of the solar cells, and increase the amount of sunlight that is captured rather than reflected back from the cells. Modifying the material in this way makes it a lot less reflective, allowing solar cells that use it to trap light even when it's coming from very low angles [18]. In 2016, Trina Solar, a solar panel manufacturer, announced it had achieved a new efficiency record for black silicon solar cell of 23.5% on a large-area, mono-crystalline, square silicon wafer. Black silicon is currently used in about 30% of the multi-crystalline solar cell market [16]. Analysts predict that by 2020, 100% of multi-crystalline silicon market will be black silicon. The researchers have obtained the record-breaking efficiency of 22.1% on nanostructured silicon solar cell as certified by Fraunhofer ISE CalLab [40].In 2009, the cost of a solar panel installation was $8.50 per watt, which is much more than a year back.

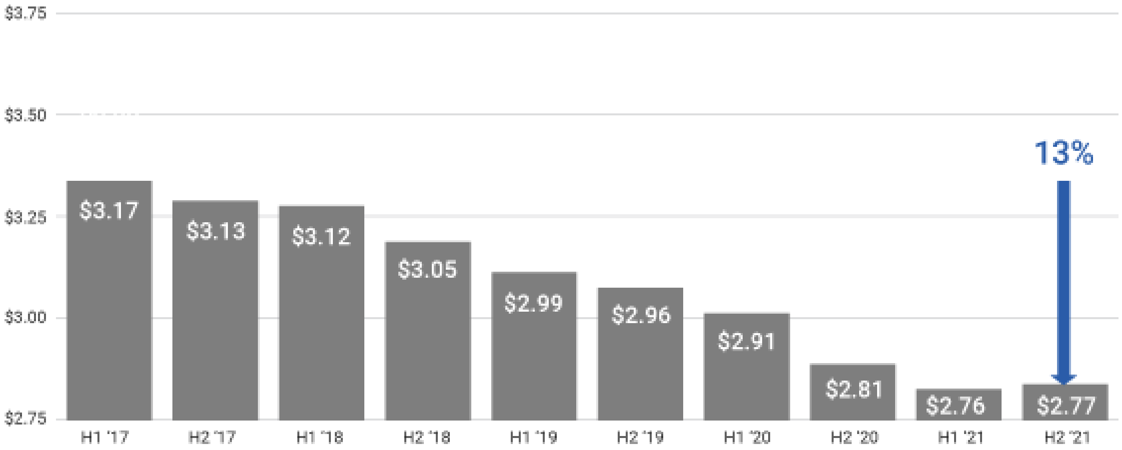

Fig.I.13-Solar panel cost over time per watt, by half year (2017-2021) [41].

The solar industry today is considerably different: not only has solar panel efficiency increased significantly, but solar panel manufacturers have improved their manufacturing procedures enormously as well.

I.3.3 Surface-enhanced Raman spectroscopy (SERS)

SERS employs inelastic scattering of monochromatic light by surface-immobilized biomolecules allowing the capture of unique signatures corresponding to molecular vibrations. This capability to distinguish among different molecules without involving time consuming steps, complex chemistry, or labels, complex chemistry, makes SERS a potentially very efficient method of bio-detection. The excitation of localized surface plasmons by light interacting with noble metal nanostructures (SERS substrates) increases dramatically the intensity of Raman scattering by the analyte, allowing the detection of very small amounts of molecules, from monolayers down to the single molecule limit.

In routine sensing measurements, all-dielectric resonant micro-and nanostructures composed of high-index dielectrics have recently emerged as a potential surface-enhanced Raman scattering (SERS) platform that can complement or potentially replace metal-based rivals [42]. However, a much-discussed challenge of SERS is that the electromagnetic enhancement of Raman scattering depends on the spacing, size, and shape of metal nanostructures where plasmonic waves are induced. In order to achieve efficient and reproducible SERS measurements, control over the substrate geometry is required at the nanoscale dimensions [42–44]. *Jorg Hubner* fabricated an integrated spectrometer device by using epoxy resist (SU-8) on black silicon as Raman spectroscopy and coupling a charge-coupled device (CCD) element. The surface Raman spectra recorded by an on-chip spectrometer show that the black silicon integrated system is suitable for Raman sensors [23].

References

[1] A. Goetzberger, C. Hebling, Photovoltaic materials, past, present, future, Solar Energy Materials and Solar Cells. 62 (2000) 1–19. https://doi.org/10.1016/S0927-0248(99)00131-2.

[2] A. Polman, M. Knight, E.C. Garnett, B. Ehrler, W.C. Sinke, Photovoltaic materials: Present efficiencies and future challenges, Science. 352 (2016) aad4424. https://doi.org/10.1126/science.aad4424.

[3] J. Lv, T. Zhang, P. Zhang, Y. Zhao, S. Li, Review application of nanostructured black silicon, Nanoscale Research Letters. 13 (2018) 1–10.

[4] T.-H. Her, R.J. Finlay, C. Wu, S. Deliwala, E. Mazur, Microstructuring of silicon with femtosecond laser pulses, Appl. Phys. Lett. 73 (1998) 1673–1675. https://doi.org/10.1063/1.122241.

[5] C. Mark, Black Silicon: 23 Years Later, SPIE Professional. (2019).

[6] J. Perlin, From Space to Earth, the Story of Solar Electricity. Villoz, A. Labouret-M. énergie solaire photovoltaïque : le manuel du professionnel.", 1999.

[7] S. Abdelilah, Électricité photovoltaïque - Matériaux et marchés, Technique de l'ingénieur. (2013).

[8] S. Charnet, Croissance et proprietes d'emission dans le visible de nanograins de silicium dans une matrice de silice : analyse par ellipsometrie spectroscopique, thesis, Caen, 1999. http://www.theses.fr/1999CAEN2023 (accessed July 2, 2019).

[9] K.N. Nguyen, P. Basset, F. Marty, Y. Leprince-Wang, T. Bourouina, On the optical and morphological properties of microstructured Black Silicon obtained by cryogenic-enhanced plasma reactive ion etching, Journal of Applied Physics. 113 (2013) 194903. https://doi.org/10.1063/1.4805024.

[10] G. Kumaravelu, M.M. Alkaisi, A. Bittar, Surface texturing for silicon solar cells using reactive ion etching technique, in: Conference Record of the Twenty-Ninth IEEE Photovoltaic Specialists Conference, 2002., 2002: pp. 258–261. https://doi.org/10.1109/PVSC.2002.1190507.

[11] G.C. Thurner, P. Debbage, Molecular imaging with nanoparticles: the dwarf actors revisited 10 years later, Histochem Cell Biol. 150 (2018) 733–794. https://doi.org/10.1007/s00418-018-1753-y.

[12] Q. Yuan, J. Döll, H. Romanus, H. Wang, H. Bartsch, A. Albrecht, M. Hoffmann, P. Schaaf, D. Wang, Surface-Nanostructured Al–AlN Composite Thin Films with Excellent Broad-Band Antireflection Properties Fabricated by Limited Reactive Sputtering, ACS Appl. Nano Mater. 1 (2018) 1124–1130. https://doi.org/10.1021/acsanm.7b00302.

[13] M.A. Green, M.J. Keevers, Optical properties of intrinsic silicon at 300 K, Progress in Photovoltaics: Research and Applications. 3 (1995) 189–192. https://doi.org/10.1002/pip.4670030303.

[14] Q. Yuan, J. Döll, H. Romanus, H. Wang, H. Bartsch, A. Albrecht, M. Hoffmann, P. Schaaf, D. Wang, Surface-Nanostructured Al–AlN Composite Thin Films with Excellent Broad-Band Antireflection Properties Fabricated by Limited Reactive Sputtering, ACS Applied Nano Materials. 1 (2018) 1124–1130.

[15] X. Liu, P.R. Coxon, M. Peters, B. Hoex, J.M. Cole, D.J. Fray, Black silicon: fabrication methods, properties and solar energy applications, Energy Environ. Sci. 7 (2014) 3223–3263. https://doi.org/10.1039/C4EE01152J.

[16] C. Mark, Black Silicon Lowers Cost, Increases Efficiency for Solar, (n.d.). https://www.asme.org/topics-resources/content/Black-Silicon-Lowers-Cost-Increases-Efficiency (accessed April 1, 2022).

[17] Black Silicon: 23 Years Later, (n.d.). https://spie.org/news/spie-professional-magazine-archive/2019-april/black-silicon (accessed November 20, 2022).

[18] C.-H. Hsu, J.-R. Wu, Y.-T. Lu, D.J. Flood, A.R. Barron, L.-C. Chen, Fabrication and characteristics of black silicon for solar cell applications: An overview, Materials Science in Semiconductor Processing. 25 (2014) 2–17. https://doi.org/10.1016/j.mssp.2014.02.005.

[19] B.L. Sopori, R.A. Pryor, Design of antireflection coatings for textured silicon solar cells, Solar Cells. 8 (1983) 249–261. https://doi.org/10.1016/0379-6787(83)90064-9.

[20] H.G. Craighead, R.E. Howard, D.M. Tennant, Textured thin-film Si solar selective absorbers using reactive ion etching, Appl. Phys. Lett. 37 (1980) 653–655. https://doi.org/10.1063/1.92015.

[21] C.C. Tuck, Effective Medium Theory: Principles and Applications, Second Edition, Oxford University Press, Oxford, New York, 2016.

[22] S. Kumar, D.K. Aswal, Recent Advances in Thin Films, Springer Nature, 2020.

[23] J. Lv, T. Zhang, P. Zhang, Y. Zhao, S. Li, Review Application of Nanostructured Black Silicon, Nanoscale Res Lett. 13 (2018). https://doi.org/10.1186/s11671-018-2523-4.

[24] G. Nava, R. Osellame, R. Ramponi, K.C. Vishnubhatla, Scaling of black silicon processing time by high repetition rate femtosecond lasers, Opt. Mater. Express, OME. 3 (2013) 612–623. https://doi.org/10.1364/OME.3.000612.

[25] D.A. Saab, Black Silicon optical properties, growth mechanisms andapplications, phdthesis, Université Paris-Est, 2015. https://tel.archives-ouvertes.fr/tel-01400179 (accessed March 31, 2022).

[26] K.-Q. Peng, S.-T. Lee, Silicon Nanowires for Photovoltaic Solar Energy Conversion, Advanced Materials. 23 (2011) 198–215. https://doi.org/10.1002/adma.201002410.

[27] V. Pareek, A. Bhargava, R. Gupta, N. Jain, J. Panwar, Synthesis and Applications of Noble Metal Nanoparticles: A Review, Advanced Science, Engineering and Medicine. 9 (2017) 527–544. https://doi.org/10.1166/asem.2017.2027.

[28] G. Fischer, E. Drahi, M. Foldyna, T.A. Germer, E.V. Johnson, Plasma nanotexturing of silicon surfaces for photovoltaics applications: influence of initial surface finish on the evolution of topographical and optical properties, Opt. Express, OE. 25 (2017) A1057–A1071. https://doi.org/10.1364/OE.25.0A1057.

[29] F. Atteia, J. Le Rouzo, G. Berginc, J.J. Simon, L. Escoubas, Black silicon (BS) using room-temperature reactive ion etching (RT-RIE) for interdigitated back contact (IBC) silicon solar cells, 10913 (2019) 109130U. https://doi.org/10.1117/12.2509326.

[30] S. Leopold, C. Kremin, A. Ulbrich, S. Krischok, M. Hoffmann, Formation of silicon grass: Nanomasking by carbon clusters in cyclic deep reactive ion etching, Journal of Vacuum Science & Technology B: Microelectronics and Nanometer Structures. 29 (2011). https://doi.org/10.1116/1.3521490.

[31] J.S. Yoo, I.O. Parm, U. Gangopadhyay, K. Kim, S.K. Dhungel, D. Mangalaraj, J. Yi, Black silicon layer formation for application in solar cells, Solar Energy Materials and Solar Cells. 90 (2006) 3085–3093. https://doi.org/10.1016/j.solmat.2006.06.015.

[32] D. Murias, C. Reyes-Betanzo, M. Moreno, A. Torres, A. Itzmoyotl, R. Ambrosio, M. Soriano, J. Lucas, P.R. i Cabarrocas, Black Silicon formation using dry etching for solar cells applications, Materials Science and Engineering B, Solid-State Materials for Advanced Technology. 177 (2012) 1509–1513.

[33] J. Yoo, G. Yu, J. Yi, Black surface structures for crystalline silicon solar cells, Materials Science and Engineering: B. 159–160 (2009) 333–337. https://doi.org/10.1016/j.mseb.2008.10.019.

[34] K.N. Nguyen, Étude et caractérisation des propriétés d'absorption électromagnétique du silicium micro/nano-structuré, phdthesis, Université Paris-Est, 2012. https://tel.archives-ouvertes.fr/tel-00868791 (accessed March 19, 2022).

[35] F. Zhu, C. Wang, X. Zhang, X. Zhao, H.A. Zhang, A three-step model of black silicon formation in Deep Reactive Ion Etching process, 2015 28th IEEE International Conference on Micro Electro Mechanical Systems (MEMS). (2015) 365–368. https://doi.org/10.1109/MEMSYS.2015.7050965.

[36] A. Serpengüzel, A. Kurt, I. Inanc, J.E. Cary, E.D. Mazur, Luminescence of black silicon, JNP. 2 (2008) 021770. https://doi.org/10.1117/1.2896069.

[37] P.W. May, M. Clegg, T.A. Silva, H. Zanin, O. Fatibello-Filho, V. Celorrio, D.J. Fermin, C.C. Welch, G. Hazell, L. Fisher, A. Nobbs, B. Su, Diamond-coated 'black silicon' as a promising material for high-surface-area electrochemical electrodes and antibacterial surfaces, J. Mater. Chem. B. 4 (2016) 5737–5746. https://doi.org/10.1039/C6TB01774F.

[38] A.J. Williamson, Black Silicon for Photodiodes: Experimentally Implemented and FDTD Simulated, TU - Technische Universität Ilmenau, 2010. https://hal-amu.archives-ouvertes.fr/hal-03349103 (accessed March 31, 2022).

[39] M. Steglich, M. Oehme, T. Käsebier, M. Zilk, K. Kostecki, E.-B. Kley, J. Schulze, A. Tünnermann, Ge-on-Si photodiode with black silicon boosted responsivity, Appl. Phys. Lett. 107 (2015) 051103. https://doi.org/10.1063/1.4927836.

[40] H. Savin, P. Repo, G. von Gastrow, P. Ortega, E. Calle, M. Garín, R. Alcubilla, Black silicon solar cells with interdigitated back-contacts achieve 22.1% efficiency, Nature Nanotech. 10 (2015) 624–628. https://doi.org/10.1038/nnano.2015.89.

[41] M. Sara, How Solar Panel Cost & Efficiency Change Over Time | EnergySage, Solar News. (2022). https://news.energysage.com/solar-panel-efficiency-cost-over-time/ (accessed March 31, 2022).

[42] E. Mitsai, A. Kuchmizhak, E. Pustovalov, A. Sergeev, A. Mironenko, S. Bratskaya, D.P. Linklater, A. Balčytis, E. Ivanova, S. Juodkazis, Chemically non-perturbing SERS detection of a catalytic reaction with black silicon, Nanoscale. 10 (2018) 9780–9787. https://doi.org/10.1039/C8NR02123F.

[43] R.F. Peters, L. Gutierrez-Rivera, S.K. Dew, M. Stepanova, Surface enhanced Raman spectroscopy detection of biomolecules using EBL fabricated nanostructured substrates, J Vis Exp. (2015). https://doi.org/10.3791/52712.

[44] G. Gervinskas, G. Seniutinas, J.S. Hartley, S. Kandasamy, P.R. Stoddart, N.F. Fahim, S. Juodkazis, Surface-enhanced Raman scattering sensing on black silicon, Annalen Der Physik. 525 (2013) 907–914. https://doi.org/10.1002/andp.201300035.

CHAPTER II

Biophotonic materials

Chapter II – Biophotonic materials

II.1. Introduction

The use of optical or photonic techniques to investigate, track, and maybe control a biological process at many levels of significant biology: molecular, cellular, tissue, and organismal level are referred to as "biophotonics" [1]. Biophotonics is a highly interdisciplinary field that includes physics, chemistry, engineering, and biology. It is, at the very minimum, a field that combines a physical understanding of optical devices such as light sources, detectors, and cameras, as well as particular tools used to study biology such as the microscope of various forms and technology used (Confocal, Widefield, Interferential, Raman, etc.) [2] and in that process, gain new information about the matter being probed. So we consider the photonic methods as our "Biophotonics Tools" [3–5]

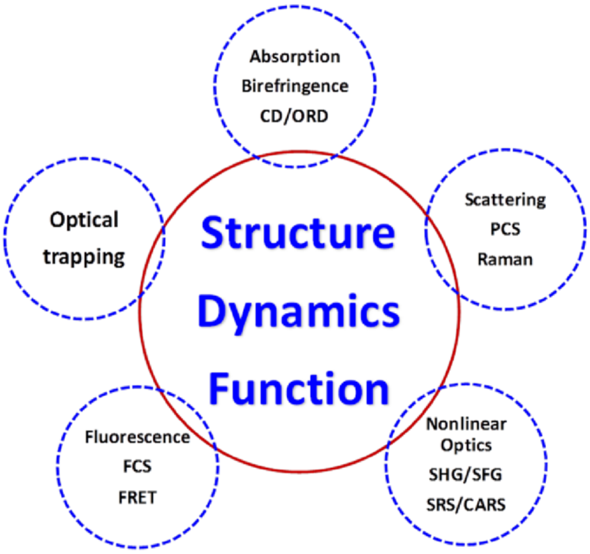

Fig.II.1-Biophotonics tools to understand structure and dynamics in biological processes [4].

In recent years, many technical advancements have appeared to improve imaging performance and instrument adaptability in optical microscopy for biophotonics applications to visualize objects ranging in size from millimeters to nanometers. Increased penetration depth in scattering media, improved image resolution beyond the diffraction limit, faster image acquisition, improved instrument sensitivity, and better contrast mechanisms are among the advancements. The functions and parameters of interest include observation and illumination techniques, observation methods, numerical aperture, the field of imaging , and depth of field [6,7].

II.2. Fluorescence phenomena

Fluorescence is defined as the emission of light by molecules that have absorbed a shorter wavelength of light. Fluorescence spectroscopy, particularly fluorescence microscopy, has emerged as the most significant biophotonics technique because it allows researchers to answer a multitude of problems in biomedicine. [8–10] provide a dipper introduction to fluorescence, [11–14] whereas discussing the developing principles of fluorescence nanoscopy. The problem in fluorescence spectroscopy/microscopy with fluorescence-labeled biomolecules is photobleaching, which is the permanent loss of fluorescence emission from a fluorophore due to its exposure to excitation light. Photobleaching is a dynamic process that occurs when fluorophore molecules are exposed to excitation light and are photochemically degraded. The average number of absorption fluorescence emission cycles that a fluorophore may undergo before being destroyed by photobleaching is determined by the excitation light intensity, the fluorophore's molecular structure, and its chemical environment. Some fluorophores are already bleached after the emission of a few photons whereas others can run through thousands or millions of excitation and emission cycles until photobleaching occurs [2]. Certain chromophores in molecules can absorb light and cause the molecule to become electronically excited. Excited electronic states, on the other hand, are often energetically unstable and short-lived. whereas fluorescence is one way for a molecule to return to its initial state from an excited electronic state (non-excited state), it is one of several processes that can follow an electronic absorption. These processes are usually represented in a Jablonski energy level diagram. **Fig.II.2** shows a simplified Jablonski diagram.

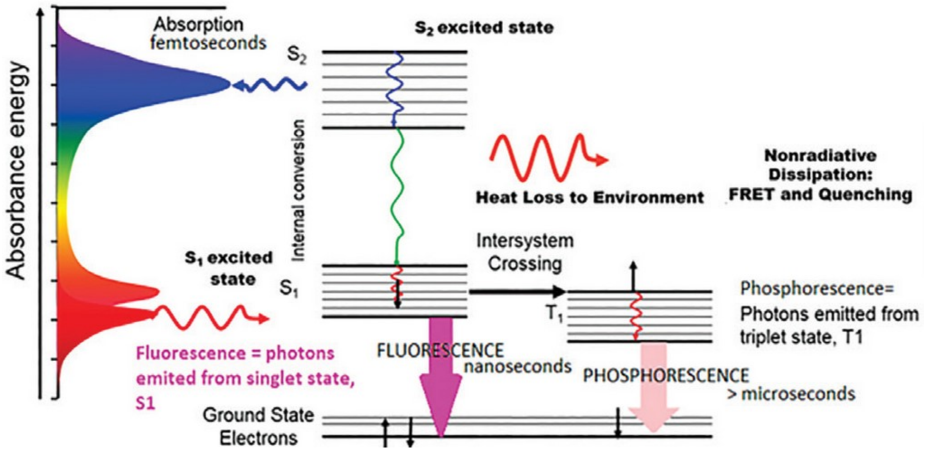

Fig.II.2- Jablonski term scheme of molecular absorbance and fluorescence [15].

The distance between the excitation and emission wavelengths is called the Stokes shift (**Fig.II.3**) and is a key aspect in the detection of emitted fluorescence in biological applications. Stokes shift is also a distinct characteristic of each fluorophore. For example, detection of emitted fluorescence can be difficult to distinguish from excitation light when using fluorophores with very small Stokes shifts, because the wavelengths of excitation and emission strongly overlap. Conversely, fluorophores with large Stokes shifts are easy to distinguish due to the large separation between the excitation and emission wavelengths. The Stokes shift is particularly critical in multiplex fluorescence applications because the emission wavelength of a fluorophore can overlap [16].

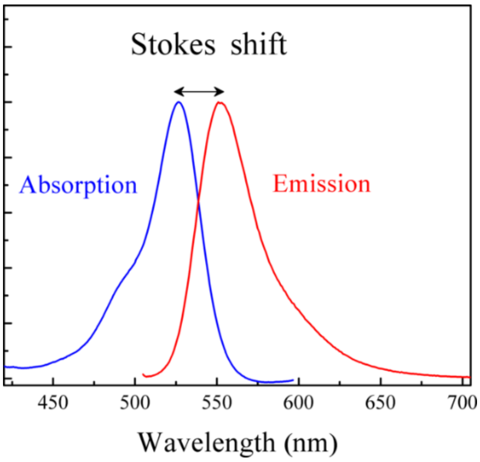

Fig.II.3-Excitation and emission spectra of (Rh6G)rhodamine 6G with ~25 nm Stokes shift [16].

II.2.1 Fluorescence Derived Parameters

II.2.1.1 Extinction coefficient

The extinction coefficient **ε**, or specific absorbance, reflects the probability of absorption. Its value can constitute a criterion for the choice of colorants; the larger **ε**, the higher the fluorescence will be at equal incident light intensity. The transmitted light intensity after absorption of incident light is given by the Beer-Lambert law and is written as follows:

$$I_t = I_0 e^{-\varepsilon c L} \qquad \text{(Eq.II.1)}$$

I_0: incident intensity, I_t: transmitted intensity, c: medium concentration and L is medium length. For the fluorescence to be strong, it is not enough that a large number of photons are absorbed, it also requires a high quantum efficiency [17].

II.2.1.2 Quantum efficiency

For a molecule to emit fluorescence radiation, it must be able to absorb a photon. The fluorescence quantum yield is defined as the ratio between the number of emitted photons and the number of absorbed photons:

$$\Phi_f = \frac{Number\ of\ \ emitted\ photons}{Number\ of\ \ absorbed\ photons} x\,100\% \qquad \text{(Eq.II.2)}$$

The efficiency of fluorescent light emission for a given molecule is determined by the quantum efficiency. Since part of the excited molecules can lose their excess energy either by the transition between singlet (↑↓) and triplet (↑↑) state or by bond dissociation, Φ_f is necessarily less than 1. Fluorophores have quantum yields between 0.1~1 [17].

II.2.1.3 Fluorescence intensity

A fluorophore that has a high extinction coefficient, as well as a high quantum efficiency, will have a very strong fluorescence intensity or "brightness". The relationship between ε and Φ_f is determined by equations (Eq.II.1) and (Eq.II.2):

$$I_f = (I_0 - I_t) \times \Phi_f \qquad \text{(Eq.II.3)}$$

With $I_0 - I_t = I_a$ Where;

I_0 Laser source intensity;

I_a absorbed intensity;

I_t transmitted intensity;

Considering the equation (Beer-Lambert) and the first term of the limited expansion of the exponential, fluorescence intensity is written as follows:

$$I_f = 2.3 \times (\varepsilon.\Phi_f.C.L.I_0) \qquad \text{(Eq.II.4)}$$

This relation is therefore only valid if the concentration of the fluorophore solution or the optical path of the excitation beam is very small. It is necessary to determine the concentration range, in which the fluorescence intensity is linear with that of the source [17].

II.2.1.4 Lifetime or photo-stability

The third important feature of a fluorescent molecule is the fluorescence lifetime (τ_f). It corresponds to the average lifetime of the excited state.

Most fluorophores have lifetimes of the order of nanoseconds or even picoseconds. The shorter time leads to better sensitivity of the fluorophore. Indeed, several successive excitations are possible because the fluorophore molecules quickly return to their ground state [8].

II.2.2 Fluorophore host medium impact

Many factors can affect the fluorescence spectra of a component in solution such as temperature, pH, and fluorescence quenching, which temperature changes the Boltzmann statistical distribution. An increase in temperature decreases the efficiency of photoluminescence. In return, it increases with the pH of the solution. The shape of the fluorescence spectrum also depends on the pH. While quenching is an effect of fluorescence inhibition by certain molecules which affects the quantum efficiency as well as the fluorescence lifetime [8,18].

II.2.3 Fluorophores

The wide choice of fluorophores today offers greater flexibility, variation, and performance of fluorophore for research applications than ever before. Fluorophores can be divided into three general groups:

- Organic dyes;
- Biological fluorophores;
- Quantum dots.

Each fluorophore has distinct characteristics, which should be considered when deciding which fluorophore to use for a given application or experimental system [19].

II.2.4 Detection

Many different types of fluorescence detectors have been developed, and although each is specific to distinct experimental methods, all fluorescence detectors have four basic requirements:

- An excitation light source, such as lasers, photodiodes, or lamps (xenon arc and mercury vapor being the most commonly used lamps);
- A fluorophore;
- Filters to isolate specific wavelengths to excite different fluorophores;
- A detector registers the output, which is usually an electronic signal.

Although this list is not exhaustive and new instrumentation is continually being developed, common fluorescence detection instrumentation includes:

- Fluorescent microscopes
- Confocal microscope
- Spectrofluorometers
- Flow cytometers

In the present study, we will broach only the confocal microscope in the next parts.

II.3 Confocal microscopy and diffraction limit

In basic microscopes, a light source such as a pure white mercury lamp illuminates the entire sample at the same time. Wide-field microscopes (WFM) are the term given to this equipment. Widefield microscopes are limited when light emitted from the sample above and below the focal plane of interest interferes with the resolution of the image being viewed. Therefore, images of samples thicker than about 2 μm appear blurry. When viewing an object in a microscope, the light coming from the sample may be represented as a series of several point sources of light. Therefore, as light from these point sources passes through the various optical elements and aperture diaphragms of a microscope, the optical waveforms begin to spread out due to scattering and diffraction effects [2,20–22]. A small broadened diffraction pattern appears in the image of the point source as a result of this spreading. Because of the spread image, the instrument cannot resolve the separation of the images of two close point sources to reveal the real structural characteristics and details of a specimen below a certain limit. This issue occurs when two source points in the object are separated by a lateral distance of less than half the wavelength of the imaging light [23]. This restriction is called Abbe's criterion or diffraction limit. The broadened image of a point source is known as an Airy pattern. The three-dimensional distribution of light intensity in the Airy pattern is called the point-spread function (PSF) of the microscope lens [20,23,24]. **Fig.II.4** illustrated where the numerical aperture NA increases from left to right. More details within the specimen can be viewed when the Airy disk projected in the image decreases. That is, smaller Airy disks allow the viewer to better distinguish two closely spaced points in the specimen [23].

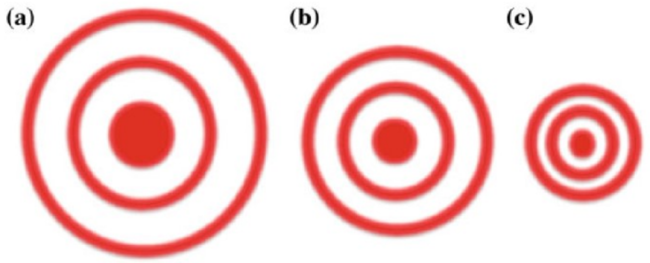

Fig.II.4- As long as the NA increases, the Airy disks get smaller for objectives of the same focal length. a) Small NA large Airy disk. b) Intermediate NA medium Airy disk. c) Large NA small Airy disk[20,23].

In conventional microscopes, the entire specimen being examined, or a large portion of it, is illuminated and observed simultaneously. The observer focuses on the sample segment located at the focal point of the microscope objective. The simplicity of this setup places a limit on image quality, as unfocused light from other parts of the sample, as well as other unwanted scattered light, will also appear in the image. The result is that the image may be blurry or some details may be obscured [2,23]. The use of confocal microscopy [25–27] helps to resolve such limitations. A confocal microscope (see **Fig.II.5**) provides sharp images of a specimen that would typically appear blurry when examined with a conventional microscope. This image-enhancing feature is achieved by an optical method that blocks out the majority of the light that does not come from the sample's focal plane, which the main feature of a confocal microscope is the use of two spatial filters with pinhole apertures [28].

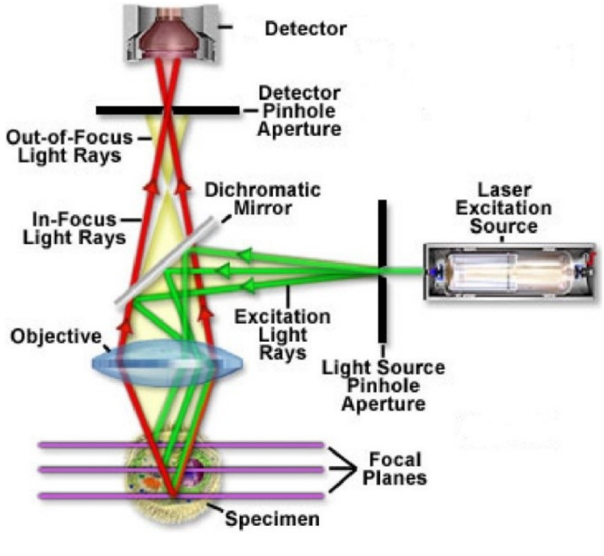

Fig.II.5- Basic concept of confocal microscopy [28].

In **Fig.II.5** a laser beam is passed through the microscope objective and focused on the sample which contains fluorescent particles (fluorophores) in a dilution. When the particles cross the confocal volume, they become fluorescent. This light is collected by the same lens and then passes through the dichroic mirror. Fluorescence signal fluctuations are detected by an avalanche photodiode [29].

II.4 Fluorescence Correlation Spectroscopy (FCS)

A key technological advance in spectroscopic methodologies is for rapid, accurate detection and diagnosis. Examples of spectroscopic techniques used in biophotonics include fluorescence spectroscopy, fluorescent correlation spectroscopy, elastic scattering spectroscopy, diffuse correlation spectroscopy, Raman spectroscopy, surface-enhanced Raman scattering spectroscopy, coherent anti-Stokes Raman scattering spectroscopy, stimulated Raman scattering spectroscopy, photon correlation spectroscopy, Fourier transform infrared spectroscopy and Brillouin scattering spectroscopy.

Citation:

> **"***In fact, FCS is now so efficient and so sensitive that it can generate misleading data (If one is not meticulously careful about experimental design) faster than any other spectroscopy I know.***"** ***Watt. W. Webb*** [30]**.**

This last citation, was written by one of the pioneers of the field, illustrates the paradox of fluorescence correlation spectroscopy: It is a relatively simple technique to implement, which gives quantitative results in real-time. Fluorescence correlation spectroscopy investigates the chemical and photophysical dynamics of dilute molecular solutions by taking measurements of the dynamic optical fluctuations of the fluorescence of a few molecules, even averaging less than one molecule at a time, in open focal volumes less than a femtoliter (10^{-18} m^3) (**Fig.II.6**) [24,30,30–32].

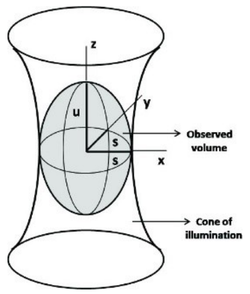

Fig.II.6- Detection volume of a confocal microscope in FCS procedures [33].

In practice, FCS is combined with confocal microscopy to yield a good signal-to-noise ratio for examining individual molecules. When a suitable model has been identified, FCS can be used to provide quantitative data such as diffusion coefficients, hydrodynamic radii, average concentrations, kinetic chemical reaction rates, and singlet-triplet dynamics [34–37].

A statistical analysis of the fluorescence signal fluctuations is used in the FCS analysis procedure to determine the molecular processes by means of an autocorrelation function G (τ) of the fluctuations in the fluorescence intensity emission.

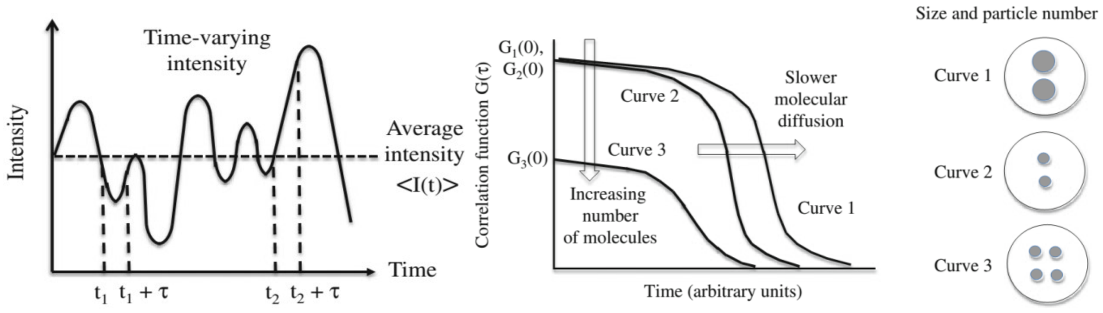

Fig.II.7- (Left) Sampling of a time-varying signal at two different time intervals, (Right) The correlation function for different numbers and sizes of molecules [4].

Fig.II.7 Illustrates a measurement that is made at two different observation times t_1 and t_2 in time intervals τ. Then the autocorrelation function G(τ) is defined by [4,38]:

$$G(\tau) = \frac{\langle \delta I(t)\delta I(t+\tau)\rangle}{\langle I(t)\rangle^2} = \frac{\langle I(t)I(t+\tau)\rangle}{\langle I(t)\rangle^2} + 1 \qquad \text{(Eq.II.5)}$$

For a two-dimensional sample with N particles, the correlation function can be written as:

$$G(\tau)=\frac{1}{N}\frac{1}{1+\left(\tau/\tau_D\right)} \qquad \text{(Eq.II.6)}$$

Where τ_D defines the diffusion time, that it defined the diffusion coefficient as follows:

$$\tau_D=\frac{W_0^{\,2}}{4D} \qquad \text{(Eq.II.7)}$$

With W_0 being the effective volume, D is the diffusion coefficient for spherical particles. The diffusion coefficient is expressed by the Stokes-Einstein relation it is temperature-dependent (discussed in the experimental part) as follows:

$$D(T)=\frac{kT}{6\pi\eta(T)r} \qquad \text{(Eq.II.8)}$$

Where:

D is the diffusion coefficient, k is the Boltzmann constant $(1.3807\cdot 10^{-23} J\cdot K^{-1})$, r hydrodynamic radius, and η is the viscosity (water or solvent) that is also a function of temperature. **Fig.II.8** Ilustre a graph for three fluorophores experiment calibration of FCS performed at 25°C. If the experiment calibration was not performed at 25°C, the all previous values should be recalculated again using the following equation [39]:

$$D(T)=D(25°C).\frac{t+273.15}{\eta(t)}\cdot 2.985\cdot 10^{-6} Pa\cdot s\cdot K^{-1} \qquad \text{(Eq.II.9)}$$

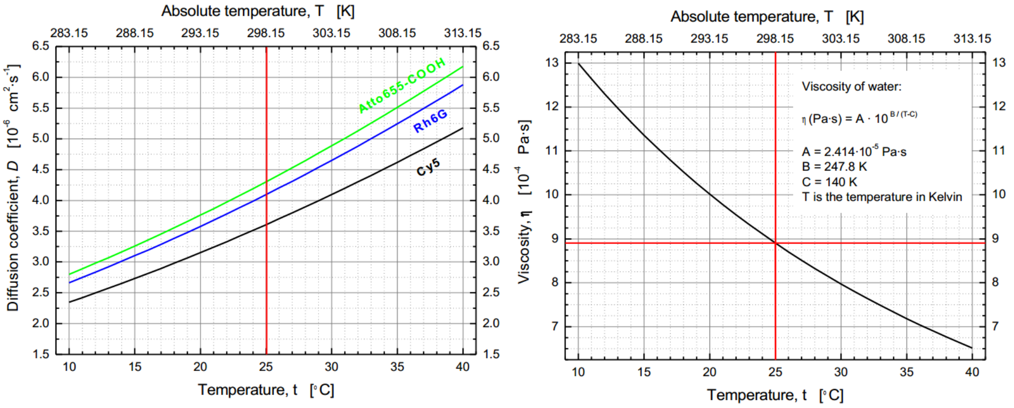

Fig.II.8- Temperature effect for three popular fluorophores and (right) the viscosity of water [39].

References

[1] G. Keiser, Overview of Biophotonics, in: G. Keiser (Ed.), Biophotonics: Concepts to Applications, Springer, Singapore, 2016: pp. 1–23. https://doi.org/10.1007/978-981-10-0945-7_1.

[2] J. Popp, V.V. Tuchin, A. Chiou, S.H. Heinemann, Handbook of Biophotonics, 3 Volume Set, Wiley, 2012.

[3] Y. Yin, K. V V, Introduction to Biophotonics, in: Biophotonics Science and Technology, August 2018, WORLD SCIENTIFIC, USA, 2017: pp. 1–11. https://doi.org/10.1142/10868.

[4] G. Keiser, Biophotonics Technology Applications, in: G. Keiser (Ed.), Biophotonics: Concepts to Applications, Springer, Singapore, 2016: pp. 323–337. https://doi.org/10.1007/978-981-10-0945-7_11.

[5] G. Keiser, Light-Tissue Interactions, in: G. Keiser (Ed.), Biophotonics: Concepts to Applications, Springer, Singapore, 2016: pp. 147–196. https://doi.org/10.1007/978-981-10-0945-7_6.

[6] X.D. Hoa, A.G. Kirk, M. Tabrizian, Towards integrated and sensitive surface plasmon resonance biosensors: a review of recent progress, Biosens Bioelectron. 23 (2007) 151–160. https://doi.org/10.1016/j.bios.2007.07.001.

[7] X. Fan, I.M. White, S.I. Shopova, H. Zhu, J.D. Suter, Y. Sun, Sensitive optical biosensors for unlabeled targets: A review, Analytica Chimica Acta. 620 (2008) 8–26. https://doi.org/10.1016/j.aca.2008.05.022.

[8] J.R. Lakowicz, ed., Introduction to Fluorescence, in: Principles of Fluorescence Spectroscopy, Springer US, Boston, MA, 2006: pp. 1–26. https://doi.org/10.1007/978-0-387-46312-4_1.

[9] N.J. Turro, Modern Molecular Photochemistry, , University Science Books Mill Valley, CA., 1991.

[10] V. Bernard, B.-S. Mário Nuno, Introduction, in: Molecular Fluorescence, John Wiley & Sons, Ltd, 2012: pp. 1–30. https://onlinelibrary.wiley.com/doi/abs/10.1002/9783527650002.ch12.

[11] M. Fernández-Suárez, A.Y. Ting, Fluorescent probes for super-resolution imaging in living cells, Nat Rev Mol Cell Biol. 9 (2008) 929–943. https://doi.org/10.1038/nrm2531.

[12] S.W. Hell, Microscopy and its focal switch, Nat Methods. 6 (2009) 24–32. https://doi.org/10.1038/nmeth.1291.

[13] S.W. Hell, Far-field optical nanoscopy, Science. 316 (2007) 1153–1158. https://doi.org/10.1126/science.1137395.

[14] S.W. Hell, Toward fluorescence nanoscopy, Nat Biotechnol. 21 (2003) 1347–1355. https://doi.org/10.1038/nbt895.

[15] What is the Jablonski Diagram?, HORIBA Scientific.. https://www.horiba.com/int/scientific/technologies/fluorescence-spectroscopy/what-is-the-jablonski-diagram/ (accessed April 1, 2022).

[16] R.M. Christie, 17 - Fluorescent dyes, in: M. Clark (Ed.), Handbook of Textile and Industrial Dyeing, Woodhead Publishing, 2011: pp. 562–587. https://doi.org/10.1533/9780857093974.2.562.

[17] E. Guiot, microscopie de fluorescence par excitation à deux photons : application à des études de corrélations et de déclins de fluorescence en milieu biologique, phdthesis, Université Paris Sud - Paris XI, 2001. https://pastel.archives-ouvertes.fr/tel-00010025 (accessed March 21, 2022).

[18] G.S. Stephen, Fluorescence and Phosphorescence Spectroscopy -Physicochemical Principles and Practice, 1st Edition, Elsevier, 1977.

[19] Life Technologies, www.thermofisher.com/ng/en/home.html (accessed April 1, 2022).

[20] J. F, W. H, Fundamentals of Optics, chap. 15, 4th ed, (McGraw-Hill, New York,), 2002.

[21] A.D. Charles, Optics for Engineers 1st ed (CRC Press, Boca Raton, 2011.

[22] H. E, Optics, 5th Edition chap. 8, Addison-Wesley, 2006.

[23] G. Keiser, Microscopy, in: G. Keiser (Ed.), Biophotonics: Concepts to Applications, Springer, Singapore, 2016: pp. 233–258. https://doi.org/10.1007/978-981-10-0945-7_8.

[24] R.Y. Tsien, L. Ernst, A. Waggoner, Fluorophores for Confocal Microscopy: Photophysics and Photochemistry, in: J.B. Pawley (Ed.), Handbook Of Biological Confocal Microscopy, Springer US, Boston, MA, 2006: pp. 338–352. https://doi.org/10.1007/978-0-387-45524-2_16.

[25] S. Colin J. R., R. Shakil, Handbook of Biological Confocal Microscopy, Springer. (2006).

[26] T. Vo-Dinh, ed., Biomedical Photonics Handbook, CRC Press, Boca Raton, 2003. https://doi.org/10.1201/9780203008997.

[27] C.J.R. Sheppard, S. Rehman, Confocal Microscopy, in: R. Liang (Ed.), Biomedical Optical Imaging Technologies: Design and Applications, Springer, Berlin, Heidelberg, 2013: pp. 213–231. https://doi.org/10.1007/978-3-642-28391-8_6.

[28] A. Basil, W. Wassef, Confocal Endomicroscopy, IntechOpen, 2013. https://doi.org/10.5772/55959.

[29] E.L. Elson, D. Magde, Fluorescence correlation spectroscopy. I. Conceptual basis and theory, Biopolymers. 13 (1974) 1–27. https://doi.org/10.1002/bip.1974.360130102.

[30] W.W. Webb, Fluorescence correlation spectroscopy: inception, biophysical experimentations, and prospectus, Appl. Opt., AO. 40 (2001) 3969–3983. https://doi.org/10.1364/AO.40.003969.

[31] S.T. Hess, S. Huang, A.A. Heikal, W.W. Webb, Biological and Chemical Applications of Fluorescence Correlation Spectroscopy: A Review, Biochemistry. 41 (2002) 697–705. https://doi.org/10.1021/bi0118512.

[32] Y. Tian, M.M. Martinez, D. Pappas, Fluorescence Correlation Spectroscopy: A Review of Biochemical and Microfluidic Applications, Appl Spectrosc. 65 (2011) 115–124. https://doi.org/10.1366/10-06224.

[33] A. Das, N. Yadav, S. Manchala, M. Bungla, A.K. Ganguli, Mechanistic Investigations of Growth of Anisotropic Nanostructures in Reverse Micelles, ACS Omega. 6 (2021) 1007–1029. https://doi.org/10.1021/acsomega.0c04033.

[34] K. Starchev, K. Wilkinson, J. Buffle, Application of FCS to the Study of Environmental Systems, in: R. Rigler, E.S. Elson (Eds.), Fluorescence Correlation Spectroscopy: Theory and Applications, Springer, Berlin, Heidelberg, 2001: pp. 251–275. https://doi.org/10.1007/978-3-642-59542-4_12.

[35] F.J. Meyer-Almes, Nanoparticle Immunoassays: A new Method for Use in Molecular Diagnostics and High Throughput Pharmaceutical Screening based on Fluorescence Correlation Spectroscopy, in: R. Rigler, E.S. Elson (Eds.), Fluorescence Correlation Spectroscopy: Theory and Applications, Springer, Berlin, Heidelberg, 2001: pp. 204–224. https://doi.org/10.1007/978-3-642-59542-4_10.

[36] E. Matayoshi, K. Swift, Applications of FCS to Protein-Ligand Interactions: Comparison with Fluorescence Polarization, in: R. Rigler, E.S. Elson (Eds.), Fluorescence Correlation Spectroscopy: Theory and Applications, Springer, Berlin, Heidelberg, 2001: pp. 84–98. https://doi.org/10.1007/978-3-642-59542-4_5.

[37] R. Brock, T.M. Jovin, Fluorescence Correlation Microscopy (FCM): Fluorescence Correlation Spectroscopy (FCS) in Cell Biology, in: R. Rigler, E.S. Elson (Eds.), Fluorescence Correlation Spectroscopy: Theory and Applications, Springer, Berlin, Heidelberg, 2001: pp. 132–161. https://doi.org/10.1007/978-3-642-59542-4_7.

[38] W. Thorsten, M. Sudipta, M. Radek, An Introduction to Fluorescence Correlation Spectroscopy, IOP, 2020. https://doi.org/10.1088/978-0-7503-2080-1.

[39] K. Peter, Absolute diffusion coefficients: Compilation of Reference Data for FCS.Technical and Application Notes | PicoQuant, (2010).

CHAPTER III

Experimental part-

Photovoltaic materials

Chapter III– Experimental part: Photovoltaic materials

Optimizing the nanostructuring of PV materials, used as an active layer, is a key element for solar cells in different technologies. Then, for a better understanding and organization of this practical part, we have two study levels of characterization of the nanostructure of Black silicon (B-Si) samples prepared from wafers without coating versus coated samples considering the solar cells application and their positive impact on efficiency by reducing the light reflectance.

III.1 Description of samples -Nanostructuring surface

In the context of characterization, this part provides an overview of the samples that we have described and used in the next parts. All needed information about the substrate used for these samples, manufacture procedure, characterization technique, and the features of needles (dimensions, chemical compound, structure, crystal orientation of substrate/needles) have been presented in the next sections.

At this stage, the main objective of this work part is optical, structural/morphological, and chemical compositions (as well as the electronic structure) investigation of all the BSi samples. Non-destructive methods which do not damage the sensitive needles of the specific surface of the BSi have been implemented by means available at the host laboratory at the Institute of Physics, Institute of Micro-and Nanotechnologies MacroNano®, Technische Universität Ilmenau, Germany. So, among the techniques that we have used, we mention such as PL, UV-Vis, SEM, SE, CLSM, XRD, EDX, REM, and XPS. The preparation and achievement of the BSi samples were carried out at CIS Research institute for the micro-sensors GmbH in Erfurt, Germany.

In the first, the experimental part for the characterization of structures and materials applied in photovoltaics was divided into two sections (**see Fig.III.1**):

- ***Section 01:*** B-Si samples without coating (three samples);
- ***Section 02:*** B-Si samples with the coating (two samples + one as reference);

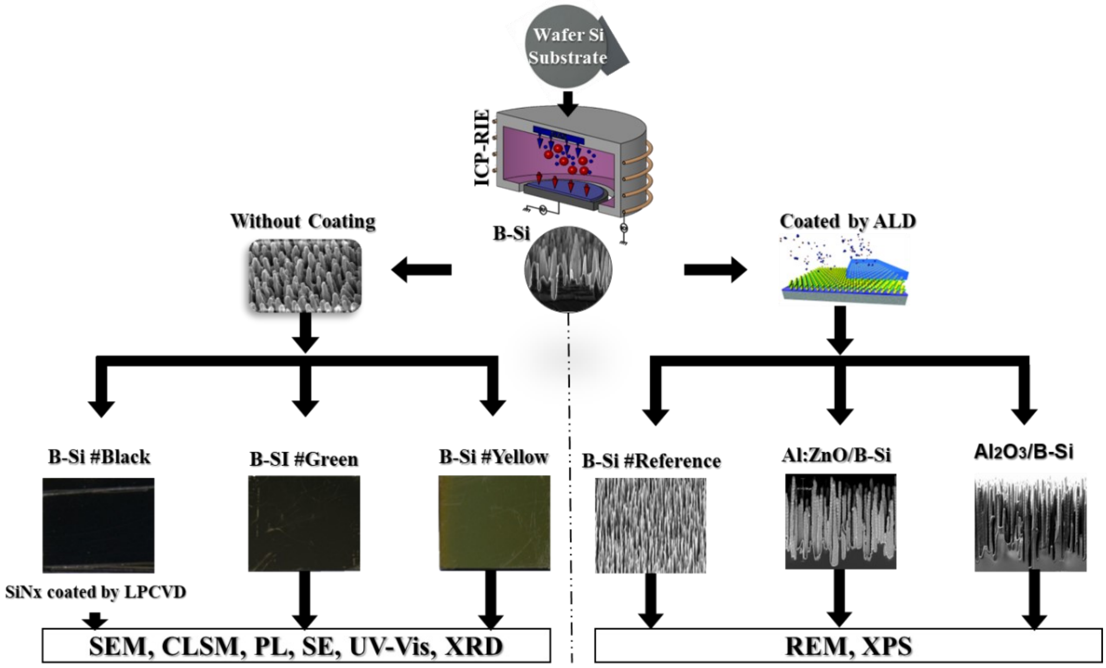

Fig.III.1- Overview of the different processes from production to characterization.

III.2 Section: Samples without coating

The substrate of all samples is monocrystalline silicon, which was prepared by the Czochralski method (It is a crystal growth technology that starts with insertion of a small seed crystal into a melt in crucible, pulling the seed upwards to obtain a single crystal), as we noted in the following table, a different feature of three samples of BSi has been determined.

Tab.III.1- samples' characteristics.

	Sample	**B-Si #Black**	**B-Si #Green**	**B-Si #Yellow**
Substrate	Crystal orientation	Monocrystalline Si {100}		
	Preparation method	Czochralski		
	Doping	N (Phosphorus)		
	Diameter	4" (~100mm)		
	Thickness	525 nm		
	Specific resistance	1-20 Ωcm		
	Doping concentration	$2.2 \times 10^{14} \sim 5.0 \times 10^{15}$ cm^{-3}		
BSi	Fabrication method	ICP/RIE	ICP/RIE	ICP/RIE
	Coating	SiNx	-	-

(a)-B-Si #Black **(b)-B-Si #Green** **(c)-B-Si #Yellow**

Fig.III.2- Morphological appearance of three B-Si samples.

The silicon etching process is often used in the DRIE technique for the manufacture of directional profiles. It is a process at ambient temperature and contains two steps of etching and passivation using sulfur hexafluoride (SF_6) gas for the etching and octafluorocyclobutane (C_4F_8) for the passivation. This elementary etch-passivation cycle is repeated several times until the preferred etch depth is reached. The advantage of this process is the controllability and the highest aspect ratio. To steadily increase the homogeneity of the black silicon layer, the manufacturing parameters such as power and gas pressure were not kept constant for the wafers, but intentionally slightly different during etch-passivation cycles, which is going to create different aspect ratios (needle shape, width, height, and density) for the three samples, as a consequence of different morphologies like needle shape, length, density and colors (B-Si-Black, green, and yellow). Then, according to the nanostructuring process or etching/passivation, no coating was deposited for the samples B-Si-Green and B-Si-Yellow. Otherwise, the sample of B-Si-Black one-layer SiN_x was deposited at temperatures of about 800°C through low-pressure chemical vapor deposition (LPCVD).

However, an additional step was carried out for the B-Si-green and B-Si-yellow to remove the remains of the passivation layer formed by (C_4F_8) on the specific surface of silicon. Finally, the three wafers were cut into pieces of different sizes which will be characterized subsequently by means of the various optical and structural characterization techniques mentioned above in **Fig.III.2**. The three samples differ markedly to the naked eye with scratches on the surface of the samples which easily occur due to the highly sensitive surface.

III.2.1 Experimental results

III.2.1.1 Structural characterization

In order to evaluate the surface morphology of the BSi samples, several structural characterization techniques and equipment were applied such as SEM “AURIGA 60 ZEISS”, LSM “Olympus LETX OLS 4000”, XRD “Siemens D5000”, EDX "Thermo-Fischer scientific"

III.2.1.1.1 SEM results

The SEM was used to further study the morphological characterization of the three B-Si samples. The following figures **(Fig.III.3**, **Fig.III.4**, and **Fig.III.5)** show views of the specific B-Si surfaces of each sample in the edge and middle at angles (0°, 42°, and 54°) with different electrons beam energies (from 7 KeV to 20 KeV) and magnifications of 100X and 2000X. Therefore, signals are detected using two detectors "SESI and InLense". The SESI (Secondary Electron and Secondary Ion) is a chamber detector that can detect both secondary electrons and secondary ions, depending on the applied suction voltage whether positive or negative. The SESI is particularly suited to the exploration of topography and would have a lower sensitivity to charge effects compared to the InLense detector. The InLense detector offers very high resolution. In addition, a very low accelerating voltage can be used, which increases the surface sensitivity.

a. B-Si #Black

The BSi-Black sample was examined extensively by choosing two regions; the damaged area (at the edge) and almost pure (in the middle) to make a comparison between the two morphologies in the same sample and to show in which way the damage affects the nanostructure of the B-Si sample (needle's shape). The results are presented below in the following figures:

b. B-Si #Green

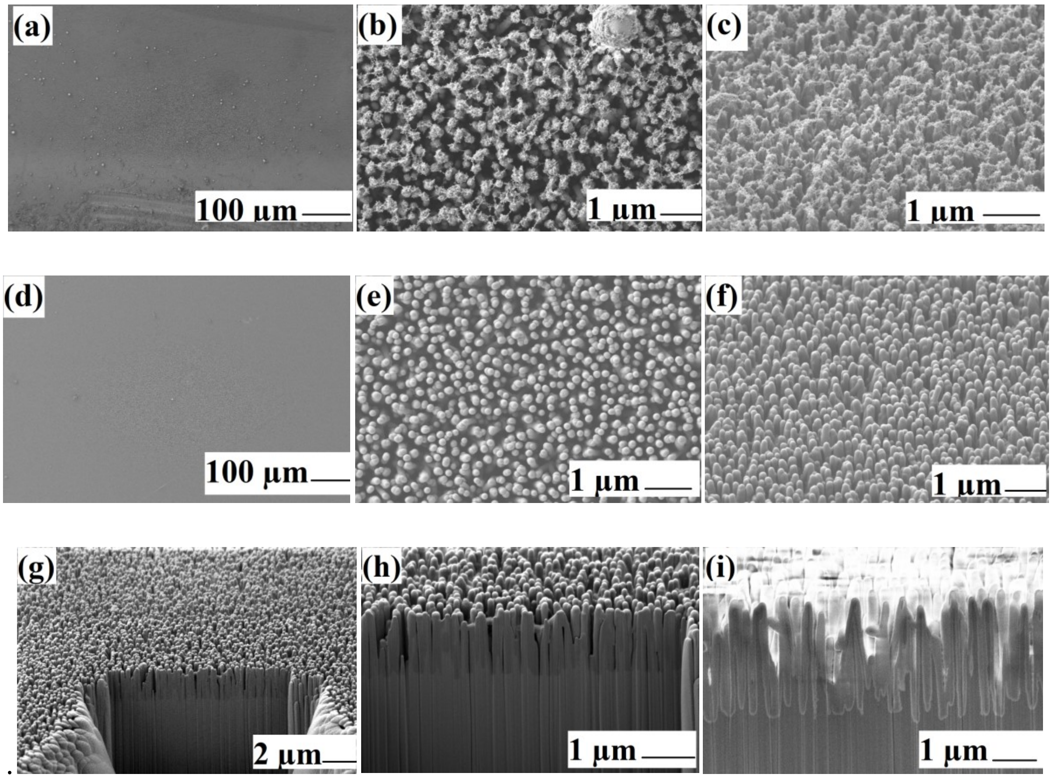

Fig.III.3- SEM images of B-Si-black sample taken from the edge and the middle: (a), (b) Top views, and (c) Tilted at 45° top view taken from the edge of the sample. (d), (e) Top views and (f) Tilted at 45° top view taken from the middle of the sample. (g), (h), and (i) Tilted (at 54°) side view after cutting with different electron beam energies, different magnifications, and different signals.

According to the SEM images, the focus on the B-Si-Black sample was sufficient to know the necessary information and to discover the influence of the defects on the surface. So, we will set this focus also for the other two samples (B-Si-green and B-Si-yellow). Therefore, we have to examine only one zone (in the middle) which can help us to study the morphological aspect of the three samples, see **Fig.III.4** and **Fig.III.5**.

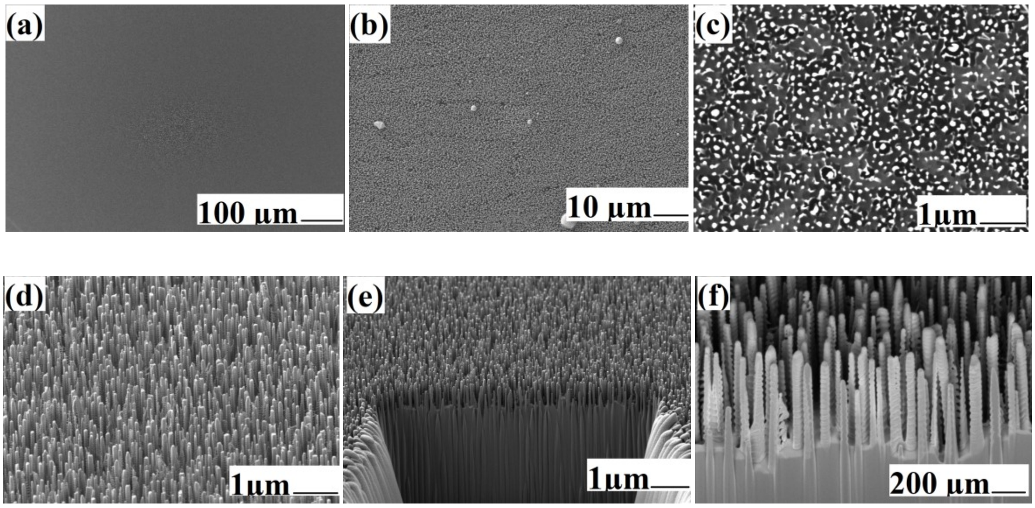

Fig.III.4- SEM images of B-Si-green sample: (a), (b), and (c) Top views. (d) Tilted top view at 54° taken from the edge of the sample. (e) Tilted side view at 54°of the cuts. (f) Tilted side top view at 54° of the sample after the cut.

c. B-Si #Yellow

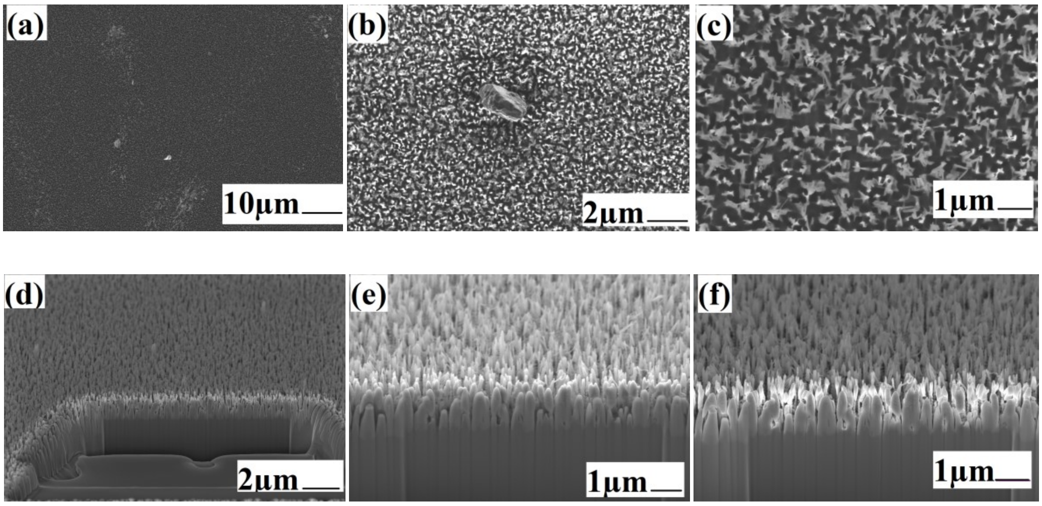

Fig.III.5- SEM images of B-Si-yellow sample: (a), (b), and (c) Top view. (d) Tilted top view at 54° of the cuts. (e), (f) Tilted side view (54°) after the cut.

III.2.1.1.1.1 Results discussion

All samples have a nanostructured surface (needles) formed by the alternating and directional deep reactive ion etching (DRIE) process. For the B-Si-Black sample, the needles are all on a relatively planned surface and placed at the same level of specific silicon surface area which will give a certain morphological uniformity when all the needles have the same height (peak to valley), see **Fig.III.3 (h).**

Regarding the B-Si-green sample, the needles are visible, and the depth-height of the needles is mostly uneven, so it is clear their variations in the same area, see **Fig.III.4 (f)**.

Subsequently, the B-Si-yellow sample has a very irregular surface and the height of the needles is too variable, see **Fig.III.5**. The individual needle **Fig.III.4 (f)** on the B-Si-green sample is thinner compared with the individual needle on the B-Si-black and B-Si-yellow samples as presented in the figures respectively (**Fig.III.3 (h)** and **Fig.III.4 (f)**). These three figures show a variation in the height, shape, and density of needles referring to the slight variation in the production process of black silicon. They also show that the part of the perimeter of the needle is bright due to the re-deposition of some materials (impurities) and the inside of the needle is dark which refers to the silicon substrate Si(100). **Fig.III.5 (d)** shows some defects upon the substrate caused by the etching during cutting that due to imbalances in the charge carriers that have formed in the corners and edges, material removal occurs irregularly resulting in a removal preference from one area to another.

The needles reach only about half these heights, when we look closely at the long needles it looks like two parts. However, the upper half part has a slight formation of depression on the surface and the lower half shows clear pits. As a result, the needles either were completely etched or became very thin during production. Therefore, the needles reach from height. The main reason for this phenomenon is unknown yet because the manufacturing parameters were kept constant throughout the process.

In order to be able to quantitatively compare these production-related structural differences of the samples, the needles of all samples were examined more precisely concerning different dimensions. Thus, from the measurement of the height, the diameter, and the distance of six needles of each sample, a mean value was calculated, which was recorded in **Table.III.2**. In addition, the thickness of the entire black silicon layer was measured.

Tab.III.2-The dimensional characteristics of the B-Si samples.

Samples	B-Si #Black	B-Si #Green	B-Si #Yellow
Thickness-B-Si-layer [nm]	2644	2451	2169
Needle height [nm]	2136	1702	1828
Needle diameter[nm]	300	154	179
Needle distance [nm]	50	223	392

Fig.III.6 Illustrates such damaged nanostructuring (of needles) and contamination on the surface which negatively affect the optical behavior of samples when the surface interacts with light. These defects can lead to losses by the reflection of the incident light since the purpose of this nanostructuring is to trap and improve the absorption of light.

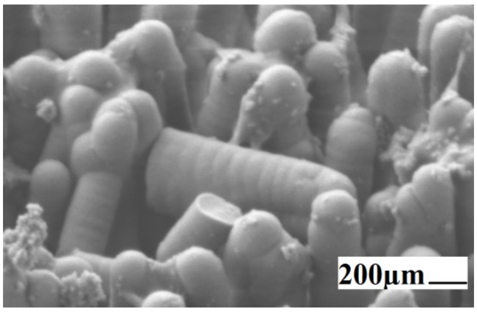

Fig.III.6- SEM image shows damaged surface taken from the near edge of B-Si-sample.

III.2.1.1.2 EDX results

Energy-dispersive X-ray spectroscopy is an analytical technique used for elemental analysis and chemical characterization of a sample. Its characterization capabilities are largely due to the fundamental principle that each element has a unique atomic structure allowing a unique set of peaks on its electromagnetic emission spectrum (basic principle of spectroscopy).

From the EDX spectrum in **Fig.III.7** for the three samples, a set of elements were identified citing: Carbon (C), Nitride (N), Oxygen (O), Chlorine (Cl), fluorine (F), and silicon (Si).

- Nitride appears strongly (high peak) only on the B-Si-Black sample due to the coating process.
- Some of these elements are detected because of contamination and interactions between the sample and the air such as O, and Cl.
- Other elements like C and F come from residues of the polymers used during the formation of needles.
- An oxidation occurs on the surface of the B-Si needles, this justifies the size of the oxygen peak which is relatively high due to the large specific surfaces of the needles.

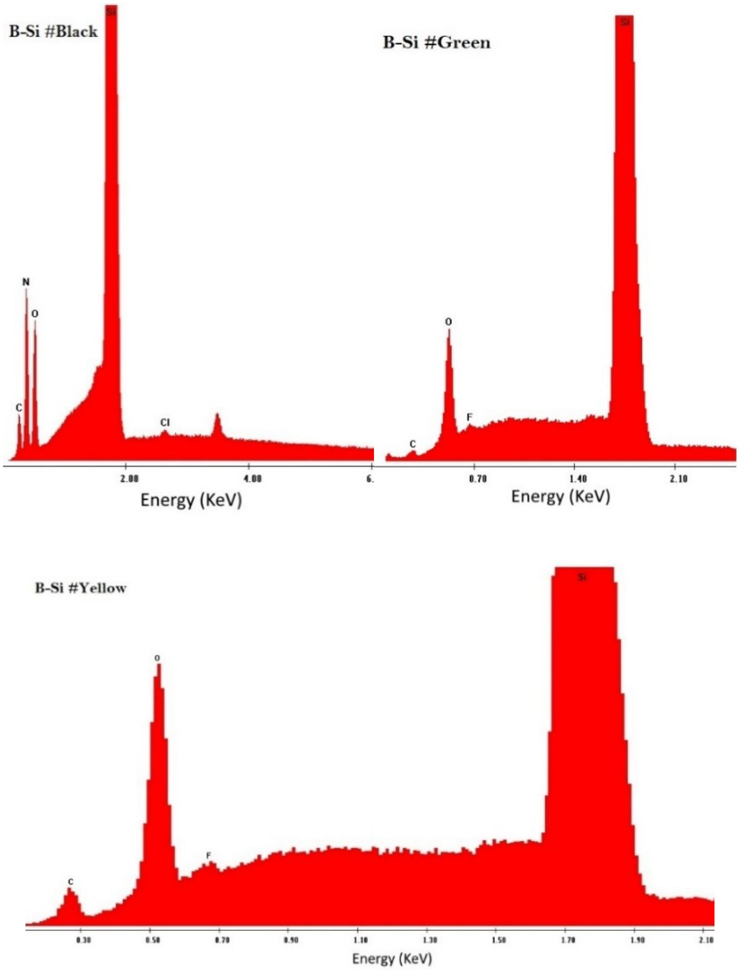

Fig.III.7- Typical EDX spectra for the three B-Si samples.

III.2.1.1.3 XRD results

X-ray diffraction is an efficient method for studying the internal crystal structure of a material. DRX results of all samples were performed using the various parameters mentioned below in the table **Tab.III.3**:

Tab.III.3- XRD device settings

X-Ray λ= 1.5406 Å, P=1.6KW (U = 40KV, I = 40mA)	
Scan speed	12s/step
Step size	0.02° (it means that for 1° we have 50 measured points)
Rotation speed	120 rpm
First point (2θ)	20°
Final point (2θ)	80°

The XRD analysis was used to find out all the orientations of both the substrate (Si) and the needles (B-Si). X-Ray tubes are made with different anode materials (in the present work we are using three anodes: Cu-K$_{\alpha}$, Cu-K$_{\beta}$, W-L$_{\alpha}$). For copper, it is reasonably long

1.54056 Å, which gives good resolution in the registration of the pattern because the copper targets are easier to cool than most other possible anodes. In addition, the Cu-Kα intensity is higher than others which is sufficient for the diffraction of solid material. Therefore Cu-Kα line is better to get a good XRD pattern. This investigation focuses principally on the measuring of the **2θ** and d-spacing (*Appendix A*). The resulting **2θ** values will be different for the same sample using the three anodes, but the **d-spacing** will be always the same. The XRD pattern is demonstrated in **Fig.III.8** below.

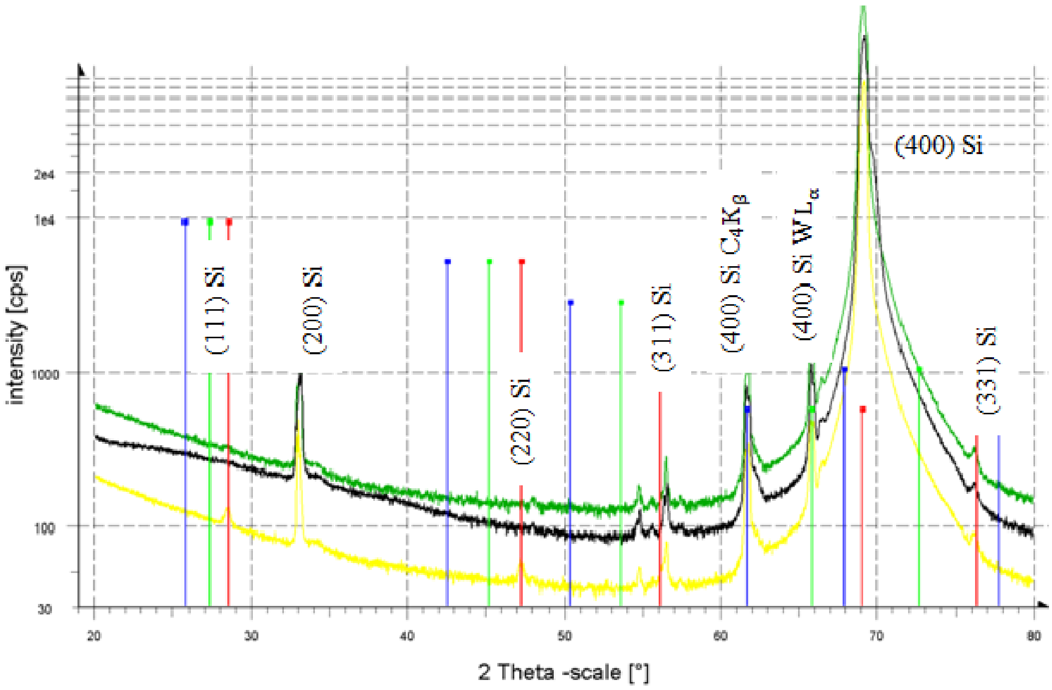

Fig.III.8- XRD analysis curve of the three B-Si samples.

From the DRX curve above, each color (black, green, yellow) corresponds respectively to B-Si #Black, B-Si #Green, and B-Si #Yellow samples. The presence of peaks is at 2θ = 28.5°, 33°, 47.5°, 56°, 61.5°, 66°, 70°, and 76° corresponding respectively to (111), (200), (220), (311), (400) Cu-L_{β}, (400) W-$L_{\alpha 1}$, (400), and (331).

As expected, peaks of substrate orientation occur. At (111) it is the wafers peaks. At (111 wafers it is the peaks of (111), (333) Lattice planes, and at (100) wafers the peaks of (400) lattice planes. Due to the high intensity of peaks at signal crystals, an additional forbidden peak (200) occurs. This peak appears since some needles are broken off; they are available in other orientations. The original (111) lattice plane is no longer oriented parallel to the surface, therefore, in severely damaged surfaces, lattice planes also occur. A similar effect can occur when the needles are very thin and thus bend. The low peaks represent the orientation of the needles and the high peaks represent the orientation of both the substrate

(Si) and the needles (B-Si) which have the same orientation as the substrate (well-oriented needles).

III.2.1.1.4 CLSM results

In order to provide a wide range of information about the structure of our samples, the confocal laser scanning microscopy (CLSM) technique has been implemented. We use for this investigation the Olympus LEXT OLS4000 system as **Fig.III.9** demonstrates. It is s a confocal microscope capable of taking high-resolution 3D images. The magnification (Optical and Digital) of this microscope ranges from 108X to 17280X. It is capable of resolving features 10 nm in size in the z-direction (sample height) and 120 nm in the x-y plane.

The system Specifications:

- Objective Lens Magnification: 5X to 100X.
- Laser 3D image Magnifications: 20X to 100X.
- Digital Magnification: 1 to 8X.
- Total Magnification capability: 5X to 17280X.
- Laser Imaging Mode: 405 nm Laser, Photomultiplier Detector.
- Minimum Z-Resolution: 10 nm.
- Minimum XY-Resolution: 120 nm.

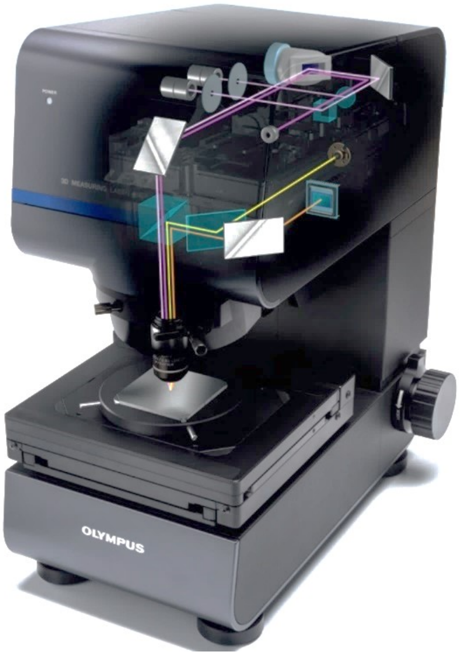

Fig.III.9- CLSM Olympus LEXT OLS4000 system.

The results of this characterization for all B-Si samples are demonstrated in the following figures below in **Fig.III.10**:

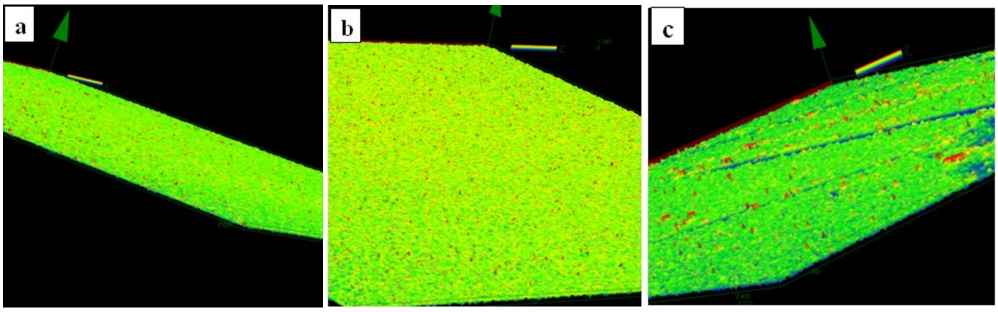

Fig.III.10- 3D images results using the CLSM for samples: (a) B-Si #Black, (b) B-Si #Green, (c) B-Si #Yellow.

This technique is support additional information for other characterization techniques-like SEM, AFM, and REM. The peaks found upon the surface of all samples assume the structure of the needles (roughened surface). The roughness rapports of the three samples are comparable, only we can see high peaks on the yellow sample and this is due to the damage occurring upon the surface.

III.2.1.2 Optical characterization

After the analysis and the discussion of the structural investigations, we have to go too far to analyze the optical behavior of the B-Si sample using the available characterization techniques such as Ellipsometry, photoluminescence (PL), infrared (IR) spectroscopy, and UV-Vis assembled with the integrating sphere.

III.2.1.2.1 Spectroscopic ellipsometer (SE) results

Ellipsometry is a very sensitive technique that can be used to characterize the composition, roughness, thickness, doping concentration, electrical conductivity, and other material properties. It is very sensitive to the change in the optical response of incident radiation when the s-polarized and p-polarized light are differently affected during interaction (reflection or transmission) with a material interface being investigated.

The linearly and circularly polarized light are usually elliptically polarized during the reflection due to the different behavior of the s-polarized and p-polarized light. Based on this change in the polarization state, we can conclude the optical constants of the material. In our study, the measurements were not determined for fixed wavelengths, but they were over a certain spectral range, this is called spectroscopic ellipsometry. These parameters are related to the reflection ratio ρ of the s- and p-polarized light by the following formula:

$$\rho = \frac{r_p}{r_s} = \tan(\Psi) e^{i\Delta} \qquad \text{(Eq.III.1)}$$

$\tan(\Psi)$ corresponds to the amount of the complex number ρ, and Δ is the phase divergence between p- and s-polarized waves. Ψ and Δ can be converted into the optical constants depending on the angle of incidence φ_0 (45):

$$\langle \tilde{\varepsilon} \rangle = \langle \tilde{n} \rangle^2 = \sin^2 \varphi \left[1 + \tan^2(\varphi_0) \frac{(1-\rho)^2}{(1+\rho)^2} \right] \qquad \text{(Eq.III.2)}$$

The used ellipsometer is shown in **Fig.III.10**.

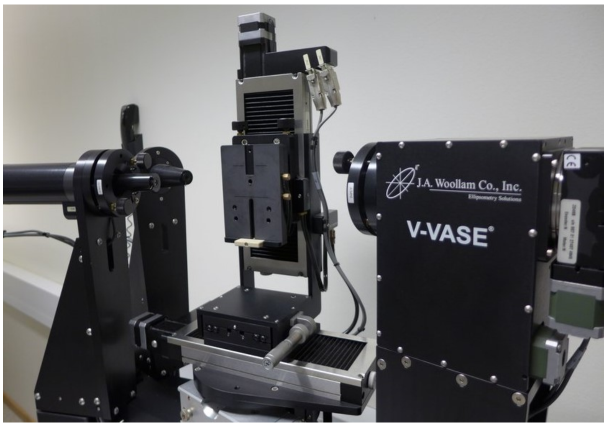

Fig.III.11- The V-VASE ellipsometer.

For each sample, we have measured two famous ellipsometric parameters Ψ and Δ which allow indicating the behavior of the reflection and the optical constants. The spectral range differs from one sample to another, generally, it varies from E= 1ev to E= 6 eV (from respectively λ = 1240 nm to λ=248 nm) to be able to follow the behavior of the samples in the visible and especially in the near-infrared range; because silicon shows a significant change there. The measurements are shown in the following **Fig.III.12**:

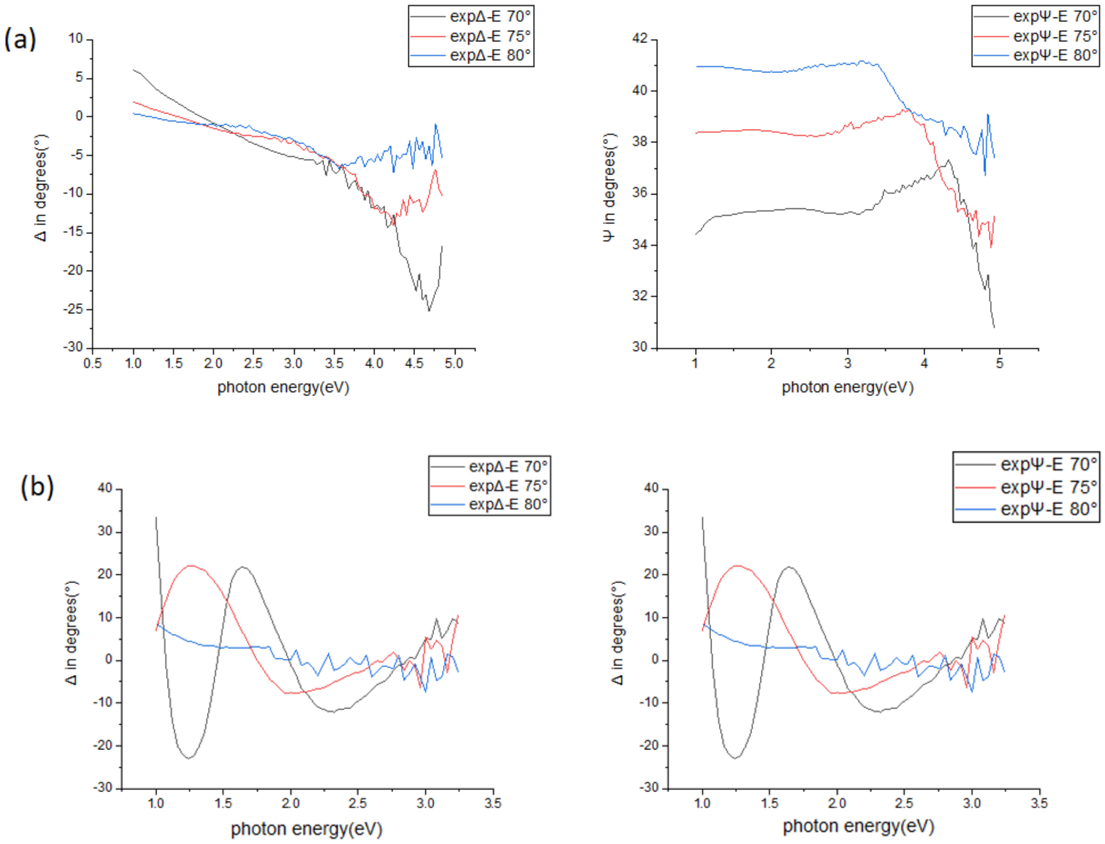

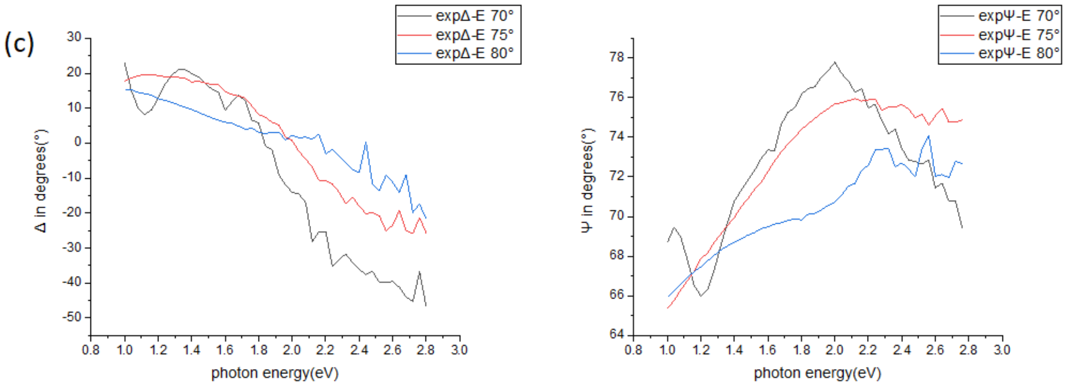

Fig.III.12- The ellipsometric parameters Ψ and Δ variation of the three B-Si samples: **(a)** B-Si #black, **(b)** B-Si #yellow, **(c)** B-Si #green.

The gradients of the ellipsometric parameters of silicon were calculated using the tabulated optical constants from V-VASE. The measurements of the three samples have been compared to the measurement of flat silicon illustrated **in Fig.III.13** below:

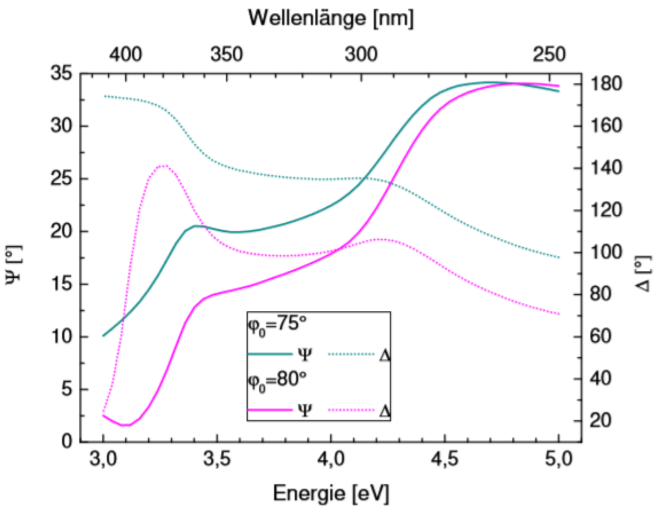

Fig.III.13- Flat silicon measurements.

Δ of planar silicon is exclusively positive. A phase jump of π at the Brewster angle is expected for the p-polarized wave at an ideal interface. For the simple sample model of a semi-infinite, homogeneous, and isotropic sample, for which reflections occur only at the air-sample interface, Δ also has a phase jump from 180° to 0°. However, since k = 0 for silicon, Δ does not change abruptly but has a wide transition range around the Brewster angle. The Brewster angle is close to the angle for which Δ = 90°. It can be seen from the values of Δ in **Fig.III.12 (a)** that the Brewster angle of silicon is in or near the investigated region. By contrast, Δ is significantly smaller for the black silicon samples than for silicon, and to a large extent even negative.

III.2.1.2.2 UV-Vis assembled with the integrating sphere

In this technique we have measured the total reflection (specular and diffuse reflection) of all samples, using the integrating sphere.

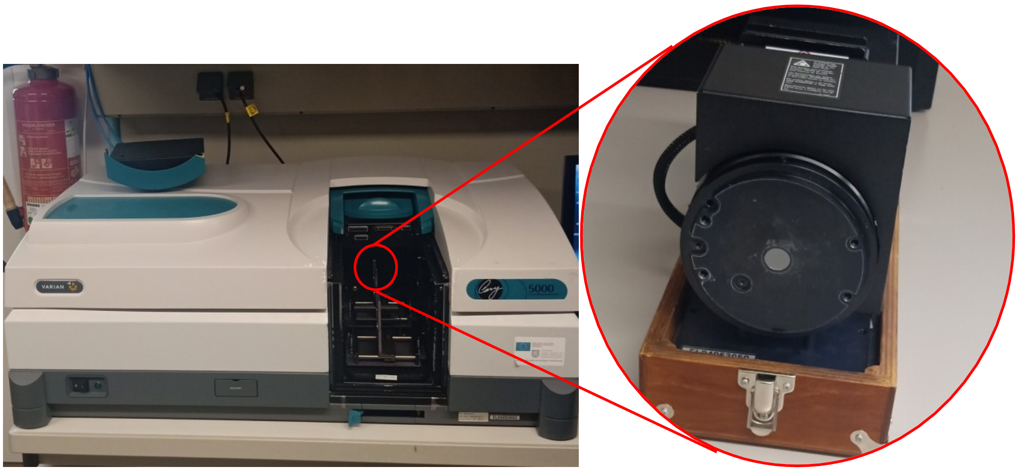

Fig.III.14- UV-Vis spectrophotometer and the integrating sphere accessory.

In Figure above, the red arrow indicates the positioning of the integration sphere in the spectrophotometer.

The reflectivity was measured for the entire spectral range on the integrating sphere with the carry 5000. However, the total reflectivity curves R_{tot} have measured for the range 250 nm to 1400 nm replaced the gold-coated integrating sphere. In this range, the sensitivity of the detector used to carry 5000 is low and a strong noise is superimposed on the measurement; this is particularly troublesome with the small reflectivity of the black silicon. Replacement of the data is possible because the spectra of both spheres between 520 nm and 1150 nm are in good agreement, confirming that the commissioning of the gold-plated integrating sphere was successful in this work. In the measurement of the silicon, no data was replaced Noise in this spectrum is still recognizable.

The spectra of the total reflectivity of the BSi samples and the reference silicon sample are shown in **Fig.III.15 (a), (b), and (c)**.

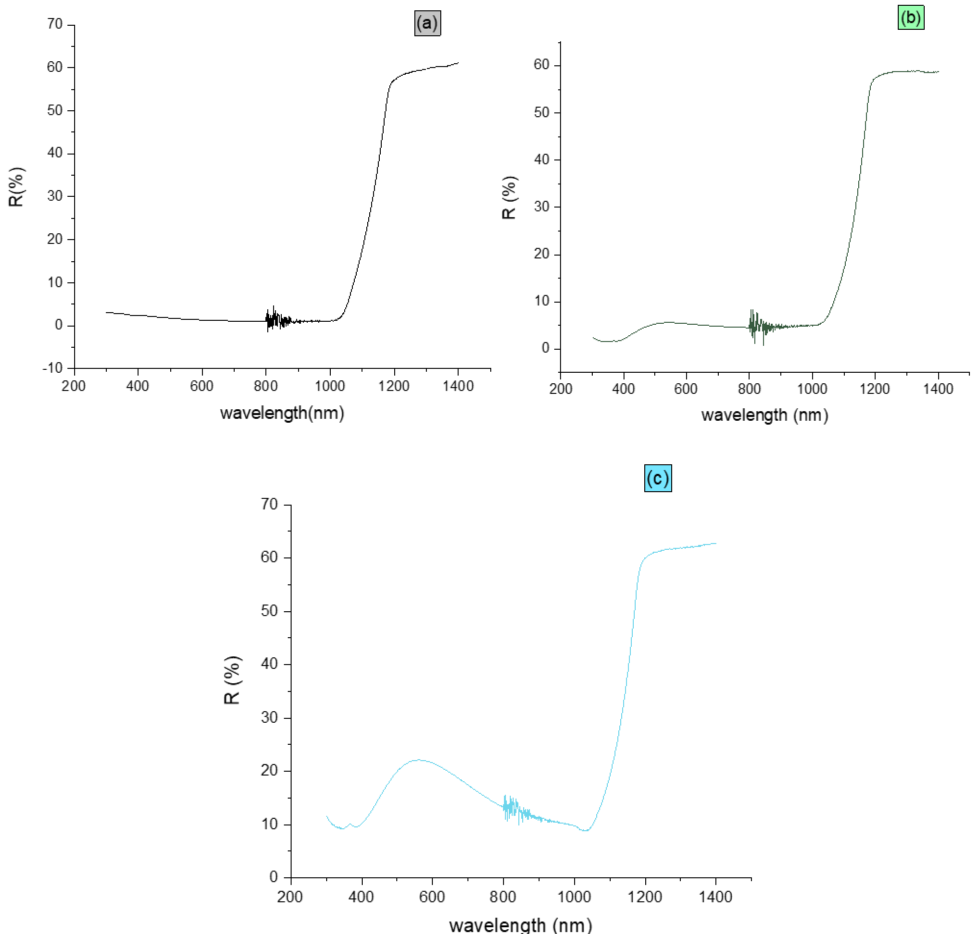

Fig.III.15- Reflectance measurements of B-Si of all samples, (a) #Black sample, (b) #Green sample, (c) #Yellow sample.

Regards to the curves, it is noticeable that the three samples have the same optical behavior; the reflectivity is extremely weak in the visible range: no reflected light for the BSi-black sample which means that the whole visible light was absorbed by this sample, for the BSi-green sample, the reflectivity goes nearly to 5% corresponding the green wavelength (λ~ 550 nm), and the same thing for the yellow sample, the reflectivity goes nearly to 20% corresponding the yellow wavelength (λ~ 580 nm).

At wavelengths just above 1000 nm, the reflectivity increases significantly, since silicon below its bandgap becomes optically transparent, allowing light to reach the back of the sample. The backside reflection occurring there increases the measured reflectivity. For the strength of the backside reflection, the condition of the reverse side is decisive. The silicon sample was roughened like the B-Si sample set on the back.

In collusion, this study part focuses on the characterization of the structure and the optical behaviour of the three used samples (black, green, and yellow). Some investigations assumed the given data about samples. For example: in the XRD technique we find that the substrate is made of silicon oriented (111), and in the PL technique (*Appendix B*) we find that the samples were n-doped using a low concentration of phosphorus. On the other hand, we examined the structure of the samples using CLSM, and SEM. With the SEM; we get a deep look at the morphology of the needles and calculate some needles parameters like the thickness and height of the needles. The enhancing IR absorption (*Appendix C*) can greatly benefit from the exceptionally good antireflection effect induced by the needle-like Black Silicon nanostructure.

III.3 Section: Coated BSi samples

The increased surface area of BSi requires the ability to cover conformally the pits or walls of nanostructure with a high aspect ratio. This is extremely challenging for most thin film deposition methods. It is well known that only Atomic Layer Deposition ALD, can uniformly coat each pit over the surface of the black silicon. Therefore, coating of BSi with Alumina Al_2O_3 or Al:ZnO by ALD would be the ideal approach to realize the surface passivation.

The preparation of the samples as mentioned previously was carried out at CIS (Research institute for the micro-sensors GmbH in Erfurt) with a different characteristic, which has been defined in the following table:

Tab.III.4- Different characteristics for three samples of Black Silicon samples.

Samples	**#BSi2**	**#BSi4**	**#BSi6**
	Al: ZnO/ BSi	**Al_2O_3/BSi**	**Bare BSi**
Substrate	Si (100)	Si (100)	Si (100)
Doping- Substrate	N (Phosphorus)	P (Boron)	N (Phosphorus)
Doping Concentration [cm^{-3}]	~ $1,5.10^{15}$	~ $4,7.10^{15}$	~ $1,4.10^{15}$
Fabrication of Black Silicon	ICP/RIE	ICP/RIE	ICP/RIE
Coating	Al:ZnO	Al_2O_3	-
Fabrication of coating	ALD	ALD	-
Thickness of coating [nm]	~ 70	~ 50	-

III.3.1 REM results -Morphological characterization

In the reflection electron microscope (REM), when an electron beam is an incident on a surface of interest, instead of using the transmission (TEM) or secondary electrons (SEM), the reflected beam of elastically scattered electrons is detected.

In the beginning, we have three BSi samples, one of them is bare BSi with no coating, and the other two samples are coated by the atomic layer deposition method as follows:

- **Al_2O_3**: Alumina deposited by thermal ALD from trimethylaluminum (TMA) and H_2O as precursors.
- **Al:ZnO**: Aluminium doped Zinc Oxide deposited by thermal ALD using methylzincisopropoxide (MZI), dimethylaluminium isopropoxide (DMAI), and H_2O as precursors.

To inspect the structural morphology of two designated BSi samples coated with different thin layers, the **Fig.III.16** Cross-sectional REM images shown for both coated samples, the film consists of spherical grains uniformly distributed over the surface and conformally coats the pits /nanostructure of two samples.

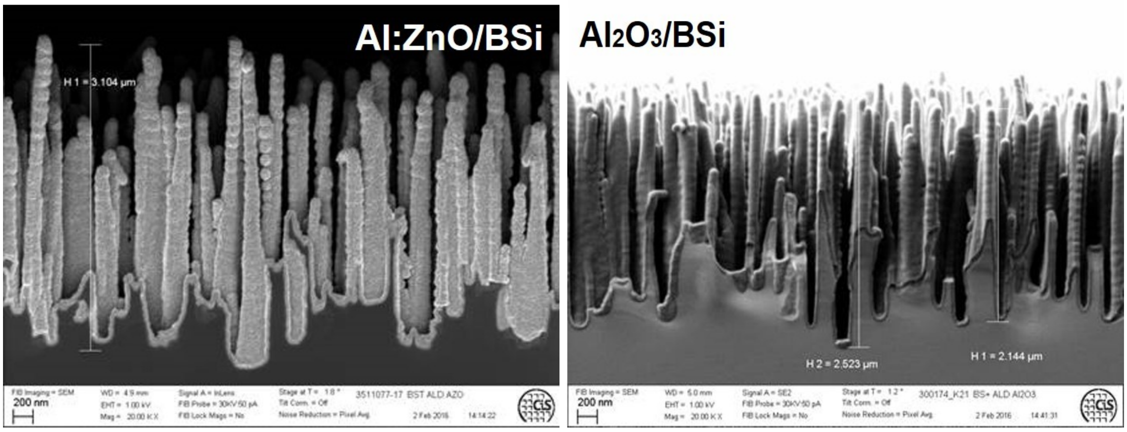

Fig.III.16- REM images side view of Al: ZnO/BSi (left) and Al_2O_3/BSi (right) covers the surface perfectly conformal.

III.3.2 XPS Analysis -Stoichiometry

XPS is a technique to analyze the atoms ‘structure and get information about their electronic structure as well as ionization energy. So, it is based on the photoelectric effect which was described by Einstein in 1905. It works when a sample is irradiated by an X-Ray beam and then quantifies the kinetic energy and number of electrons that are ejected from the material, with this technique we can obtain the chemical composition of various materials and reveals which chemical elements are present at the surface such as the carbon, oxygen, etc. Then, can inform us about the chemical bond nature which exists between these elements as well.

XPS has some advantages and some disadvantages, and we are going to go through some of them in the following:

- ✓ Non-destructive method, as well as, a surface-sensitive method, so is very helpful to do an elemental mapping for example.
- ✓ Provides quantitative measurements and information about chemical bonding and the chemical composition of molecules.

On the other hand, it has some disadvantages as well, so it is first of all:

- ✓ Very expensive technique.
- ✓ Needs a high vacuum.
- ✓ Slow process.
- ✓ Detects all elements with an atomic number of “**3**” and above, so it cannot easily detect hydrogen “**H**” and Helium “**He**”.

III.3.2.1 Practical background

The way of this work is that we have an increment X-Ray and it has enough energy, that it will be absorbed by an atom and inner shell electrons will be ejected exactly as demonstrated in **Fig.III.17**. Is as known as the photoelectric effect, and the selectivity of the energy of an X-Ray with a particular wavelength is known. The ejected photoelectron has kinetic energy that can be calculated to be equal to the energy of the incident X-Ray (hυ) minus the binding energy and the work function of the element “$\mathbf{W_f}$”. so, the work function is defined as the minimum energy needed to remove an electron from a solid to a point in the vacuum immediately outside the solid surface, so the electron should be far from the surface. Then by detecting and measuring the energy of the electron specific to each element, we are able to determine the composition of the sample.

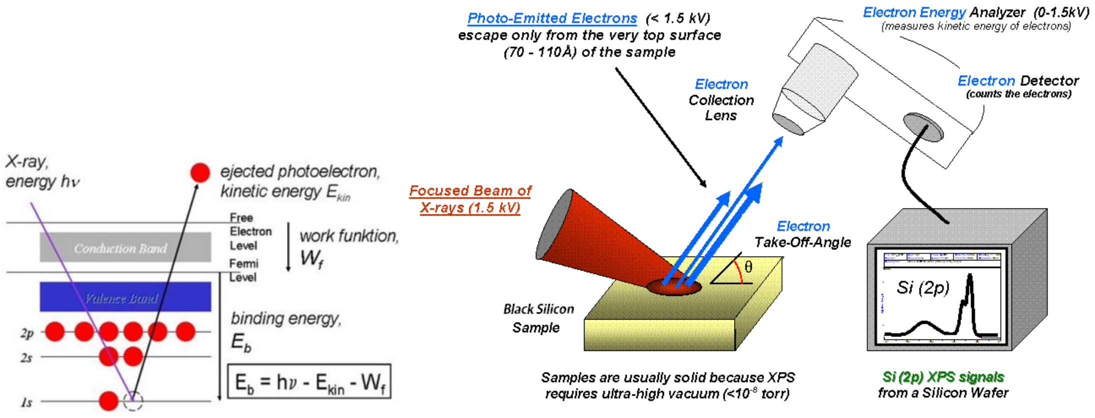

Fig.III.17- Basic principle of XPS & XP-Spectrometer Setup (B. Vincent Crist, X-ray Photoelectron Spectroscopy, English Wikipedia, accessed March 20, 2022)

III.3.2.2 XPS results

The following spectra (**Fig.III.18**), summarize the quantification data collected by XPS “SPECS Surface Nano Analysis GmbH” for the three samples analyzed, which shows the XPS spectrum of three Black Silicon samples. In the XPS spectra, the intensity is represented with respect to the binding energy (represented with kinetic energy as well). A photoelectron spectrum is recorded by counting ejected electrons over a range of electron kinetic energies, peaks appear in the spectrum from atoms emitting electrons of a particular characteristic energy. The energies and intensities of the photoelectron peaks enable the identification and quantification of all surface elements. This allows elements on the surface to be identified based on the unique binding energy each element has. The peaks areas on the spectra can also be used to obtain the concentration of the elements on the sample as well.

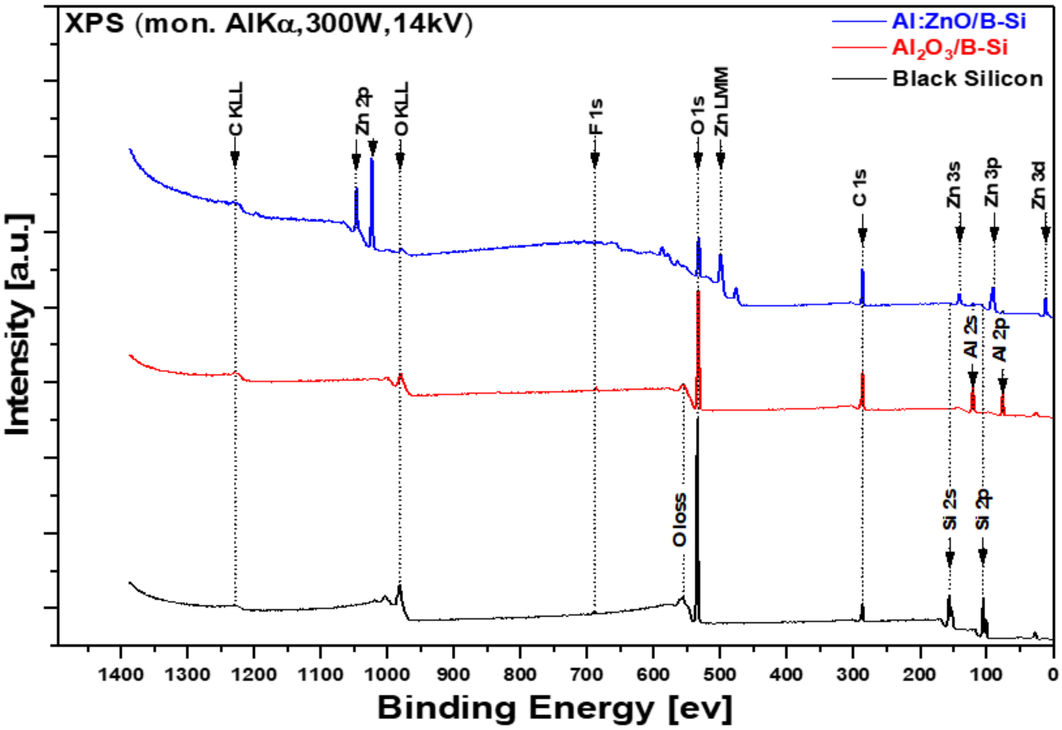

Fig.III.18- XPS survey spectra low resolution of the Black Silicon (black line), and Alumina deposited on Black Silicon (Redline), and Aluminium doped Zinc Oxide deposited on Black Silicon (blue line).

III.3.2.3 Spectra analysis

The area and the peak in the spectrum are a measure of the relative amount of the element represented by that peak. Some more detailed observations in the following:

First of all, you might have noticed that the energy axis is inversed, that's because we want to be able to get a clear view presentative of the structure of the atoms because the more you approach the nuclei or the origin the higher the band energy is going to be. The energy scale was adjusted, for the Al:ZnO/BSi, Al_2O_3/BSi, and bare Black Silicon sample, the C 1s peak "the maximum of C 1s component" was set to the reference value of the adventitious carbon at 284.80 ev. the corresponding shift is below 1.65 eV. From **Fig.III.18** at the almost right the emission from the "**2p**, **2s,** and **1s**" levels give very weak peaks at about **100 eV**, **150 eV,** and **286 eV** respectively.

The next peak is the most intense peak in this spectrum, and it is at binding energy around **534 eV** this peak is due to oxygen emission from **1s** levels of the Black silicon sample. In addition, to that, we recognize the **1s** level for the fluorine with a peak at around 680 electron volts. The remaining peak is not the XPS peak but an Auger peak from energy emission, it occurs at the binding energy around **840 eV**, **980 eV,** and**1220 eV** respectively. As we have seen, the high of the peaks is an indication of how many electrons there are in that energy level, with this method we can identify elements by comparison given that most binding energies for elements are already known. Subsequently, they can be compared from the reference book of standard spectra for identification and interpretation of XPS data, consequently determining the electronic structure of an element identified. The XPS technique was used to analyze the chemical elemental composition by the observing behavior of the **O s1**, **C 1s**, **Si 2p**, **Al 2p,** and **Zn 3p** lines from BSi, Al_2O_3/BSi, and Al: ZnO/BSi samples providing a new understanding of morphology/stoichiometry and phase evolution during the atomic layer deposition. The XPS survey spectra of Alumina deposited on Black silicon represent mainly Aluminium oxygen and carbon contributions but also fluorine contamination. For the Aluminium doped zinc oxide deposited on black silicon, one can notice only peaks corresponding to **Al**, **Zn**, **O,** and **C**. For both samples, no silicon was observed in the whole spectrum, we observed it just in the BSi sample.

It is well known, that the band gap energy is equal to the difference between the elastic peak energy and the onset of inelastic losses ($E_g = E_{loss} - E_{O\ 1s}$). The analysis of the inelastic loss (O $_{\text{loss}}$) spectrum in core-level XPS spectra can be used to determine the band gap energies of both samples Al_2O_3/BSi, and Al:ZnO/BSi.

III.3.2.4 Data quantification

In the following tables, the atomic concentration of a chemical element on the surface for each sample has been calculated from XPS measurements.

Tab.III.5- Chemical components and their positions (Binding Energy axis) from the sample's surface after XPS analysis.

Sample	**#BSi2**[Al:ZnO/BSi]		**#BSi4**[Al_2O_3/BSi]		**#BSi6**[Bare BSi]	
	B.E [ev]	**%At**	**B.E [ev]**	**%At**	**B.E [ev]**	**%At**
F 1s	-	-	686.76	0.39	687.41	0.21
O 1s	530.96	7.37	532.67	22.22	532.89	21.43
C 1s	285.04	15.04	285.89	22.41	285.14	6.74
Si 2p	-	-	-	-	103.50	71.61
Al 2p	74.16	2.27	120.38	54.98	-	-
Zn 2p	1021.83	75.32	-	-	-	-

III.3.2.4.1 High-Resolution XPS core level spectra

From the low-resolution XPS spectrum, the fitting has been made and each peak area can be used for further deconvolution which will reveal two or three distinct components represented in the high-resolution XPS core level spectra **Fig.III.19**, **Fig.III.20,** and **Fig.III.21**.

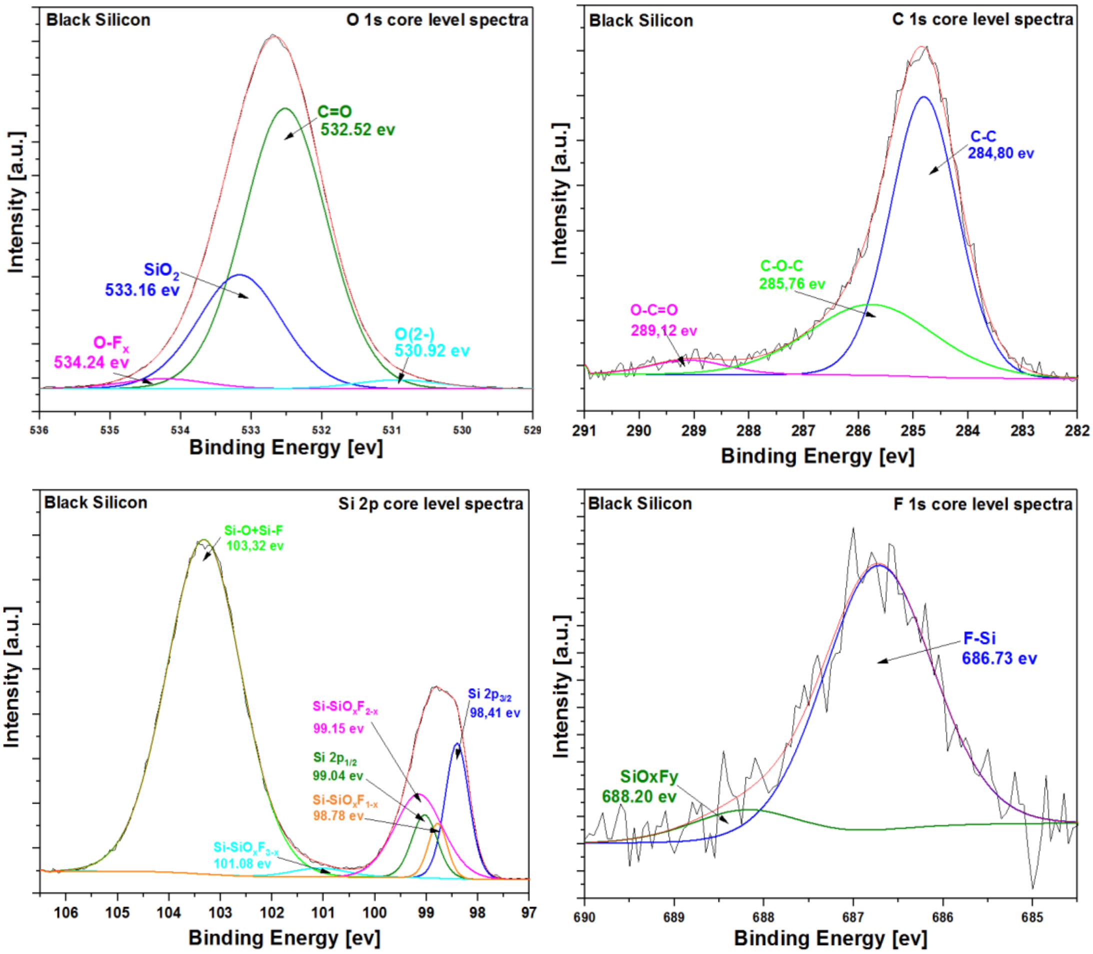

Fig.III.19- F 1s, O 1s, C1s, and Si 2p high-resolution XPS core level spectra at the surface of bare Black Silicon sample.

According to **Fig.III.19**, In the **Si 2p** high-resolution XPS core level spectra of the black silicon, we can observe:

At **103.32 eV** this peak can be assigned to **Si-O** and **Si-F** bonds, it seems to be quite difficult to distinguish **Si-O** and **Si-F** contributions because the induced chemical shifts are quite close to each other. At the same time, we can distinguish the appearance of various suboxides.

In **F 1s**, the spectrum consists of two peaks, the lower peak at **688.20 eV** is tentatively assigned to **SiOxFy** bonds, and the higher one at **686.73 eV** is most likely caused by **F-S** bonds.

Fluorine-Oxygen bond contamination at **686.73 eV** can be explained by a reactive ion etching process.

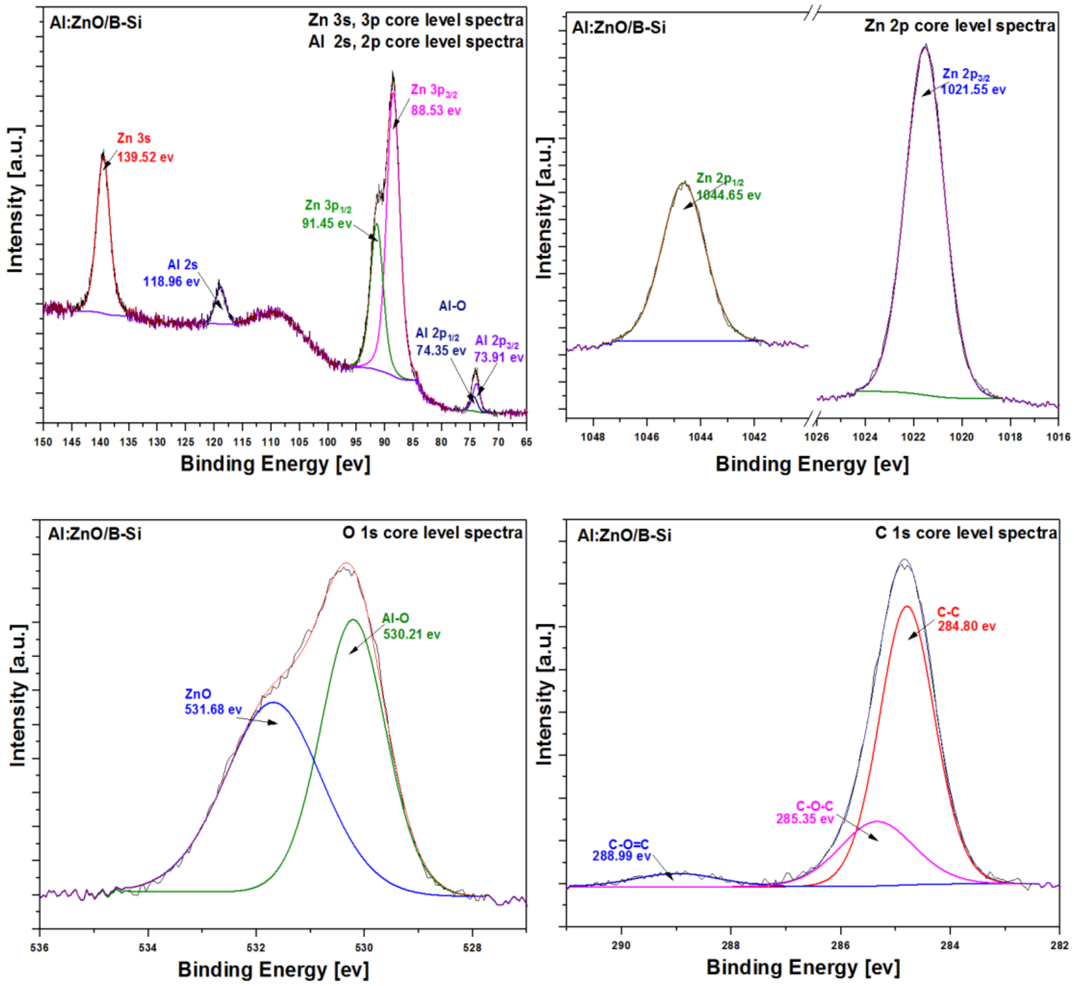

Fig.III.20- O 1s, C1s, Zn 2s/2p/3s/3p, and Al 2s/2p high-resolution XPS core level spectra at the surface of Al-doped ZnO deposited on Black Silicon sample.

The high-resolution XPS spectra above present the detailed spectra of the **Zn 2p/3s/3p, Al 2s/2p**, **O 1s,** and **C 1s** core levels.

Deconvolution of **C 1s** revealed three main distinct components as aliphatic **C-C, C-O-C,** and **C-O=C** bands.

The **O 1s** is broad and asymmetric as it is associated with different types of bonds. Further deconvolution revealed two/three distinct components, the strongest peak located at **530.21 eV** originated from **Al-O** bonds, and the other peak at **531,68 eV** is associated with **ZnO**.

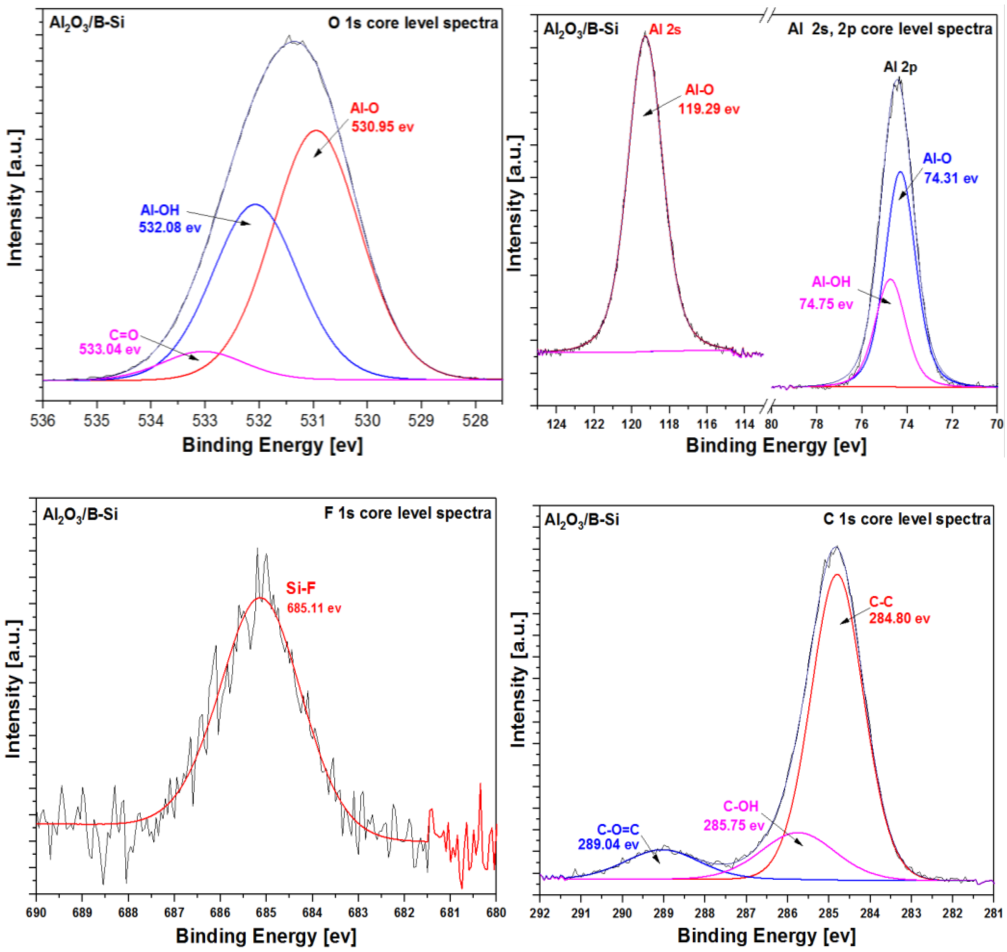

Fig.III.21- F 1s, O 1s, C1s, and Al 2s/2p high-resolution XPS core level spectra at the surface of Alumina deposited on Black Silicon sample.

The detailed spectra of the **Al 2p**, **O 1s**, **C 1s,** and **F 1s** core levels are shown in the **Fig.III.21** curves. The presence of **Al-O** and **Al-OH** bonds in the Alumina film is confirmed by the binding energies of the **Al 2p** peak at **74.31 eV** /**74.75 eV** for Alumina/BSi sample.

As a consequence of all the previous results, we can summarize them in the following points:

- One of the strengths of XPS lies in its ability to quantify the recorded signals with relative ease and without the need for reference materials. The relative peak areas have been used to estimate the surface composition, and to calculate the sample stoichiometry.
- According to the results of the XPS, confirmed that the process RIE was performed by **SF_6/O_2** plasma because no **C-F** bonds were observed in survey spectra for the black silicon sample.

- An X-ray photoelectron spectroscopy analysis was performed to investigate which elements and chemical bonds that exist within a surface as well as the electronic structure.
- Binding energy analysis confirmed the formation of conformally thin films (Al_2O_3 and Al: ZnO) on the black silicon samples.
- **CasaXPS®** processing software offers powerful analysis techniques for both spectral and imaging data.

The morphology of the deposited films and initial black silicon (or silicon grass) were investigated by means of reflection electron microscopy (REM). X-ray photoelectron spectroscopy (XPS) was used to analyze the chemical elemental composition by observing the behavior (stoichiometry) of the **Zn 2p**, **Al 2p**, **O 1s,** and **C 1s** lines of three samples.

III.4 Recap

As a recap of all sections of this part, the black Silicon represents a significant technological advancement in silicon-based photodetection. Among the multitude of fabrication methods for Black Silicon, ICP-RIE seems to be the most reasonable choice for most of the named applications because of its very good repeatability and reliability.

Different applications make different demands on the morphology of suitable Black Silicon nanostructures which can be hard to meet. For example, imaging devices are required to be image preserving, thus forbidding the utilization of strongly forward scattering Black Silicon structures for such applications. On the contrary, non-imaging optoelectronic devices like pin photodiodes or solar cells can take considerable advantage of light scattering into higher propagation angles in the absorber due to the light path enhancement at a fixed absorber thickness.

CHAPTER IV

Experimental part- Effective Medium for Biophotonics

Chapter IV– Experimental part: Effective medium for biophotonics

IV.1 Introduction

The fluorescence correlation spectroscopy (FCS) is applicable for the determination of the diffusion constants and the concentrations in the Pico to nanomolar concentration region with wide applications in biology, which makes it one of the most promising techniques for extracting quantitative information from biological media. The excitation intensity and the optical collection of the fluorescence signal have a great influence on the measured autocorrelation function defined by the relationship between the optical system i.e., the Point Spread Function (PSF), and the parameters derived from the autocorrelation curve of the FCS technique.

The quantitative results are based on the confocal volume size which should be determined experimentally. Due to the saturation, bleaching of dye molecules, optical aberrations, and refractive index variations (as seen in the biological specimen) the confocal volume is difficult to measure in situ and is sensitive.

The confocal volume of an optical system (Confocal Fluorescence Microscope) describes the spatial resolution that depends on samples properties like the sample refractive index of the sample containing medium, fluorophore photophysics, cover slide thickness, and other experimental parameters.

In this section, three approaches for the optical characterization and determination of the confocal volume parameters for the FCS measurements have been discussed and presented in the following synoptic diagram (see **Fig.IV.1**).

***1st approach**:* Measurement of a dilution series of a sample, which has the advantage of applying to any fluorophore with a known concentration.

***2nd approach**:* FCS measurement of a sample with a known diffusion coefficient to determine confocal volume in FCS curve fitting. This approach has the advantage that it is not necessary to determine the exact sample concentration.

***3rd approach**:* Direct confocal volume measurement by raster scanning of a sub-resolution fluorescent bead with high accuracy.

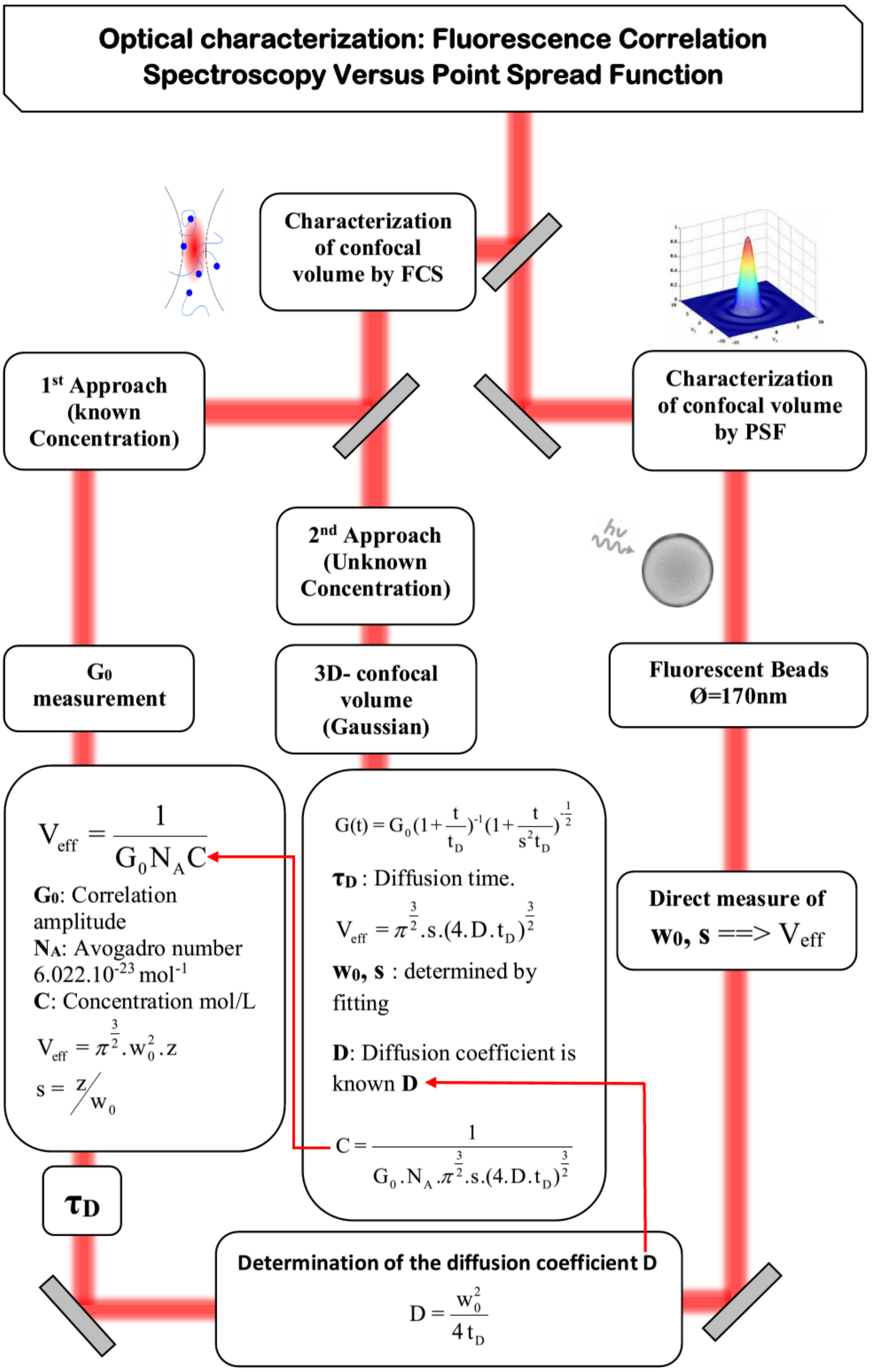

Fig.IV.1- Synoptic diagram of optical characterization approaches.

IV.2 Experimental details

IV.2.1 FCS Setup (1st and 2nd approaches)

The measurements were performed on an inverted microscope (*Nikon*) equipped with Olympus UPlanAPO NA 1.2/60x water immersion objective. The FCS setup used for this study section is illustrated in **Fig.IV.2**. The excitation source is operating at 532 nm (*Optoelectronics Company, UK*) with a maximum power of 2 mW.

Firstly, the laser beam is expanded through an afocal system to ensure the filling of the objective's backside. A dichroic mirror reflects the excitation beam to the objective which will focus the beam onto a fluorescent solution (*Alexa Fluor 532, Life Technologies, USA).* The fluorescent light coming from the solution is collected by the same objective transmitted through the dichroic mirror and focused using a lens on a pinhole of 30 µm to reject out-of-focus light and define the confocal volume. Next, a 50/50 beam splitter is used to split and send the light to two avalanche photodiodes (APDs) with single-photon sensitivity (*SPCM-AQRH, Excelitas Technologies, Canada*). The APDs are linked to a multi-channel correlator (*ALV-7004/USB Multiple Tau Digital Correlator −ALV-Laser GmbH, Langen, Germany*) which is also connected to a computer to present and evaluate the output data by the LabView commercial software (*National Instruments, Texas, USA*).

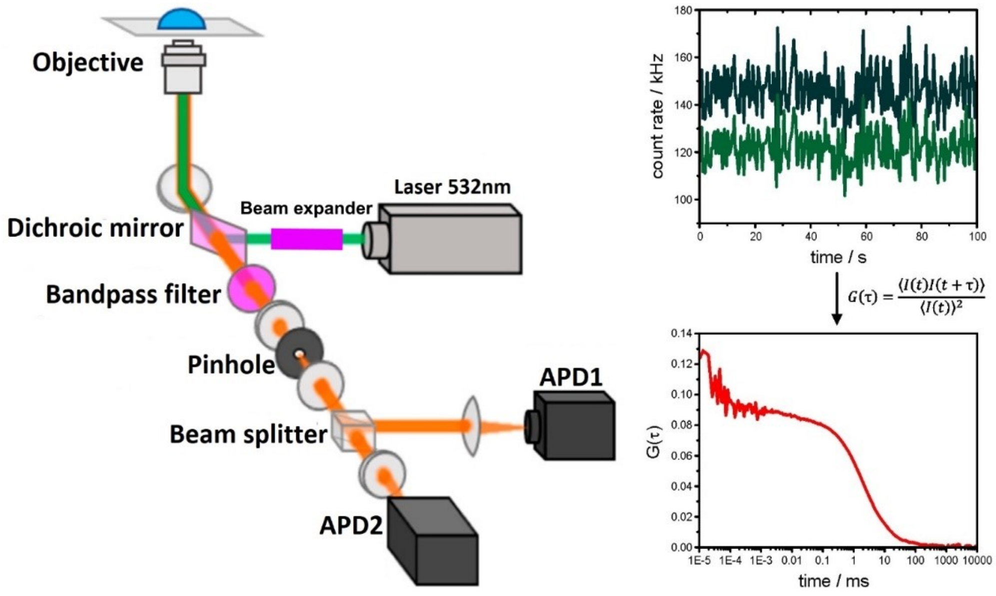

Fig.IV.2- Schematic of the experimental FCS setup.

IV.2.2 Point Spread Function (PSF) measurements Setup (3rd approach)

To study the PSF, a series of samples of fluorescent polystyrene latex microspheres Φ= 0.170 ± 0.005 nm (PS-Speck™ Kit Invitrogen) with 1.6 refractive index and maximum excitation absorption at a wavelength of 540 nm and maximum emission at 560 nm were prepared. A droplet of diluted solution (final microsphere solution was for 10^6 stock dilution) of fluorescent microspheres was dried on a coverslip. The microspheres immobilized on coverslips were then captured using a water immersion objective with a coverslip thickness corrector.

The scan plane of the sample was moved to different directions using an XYZ piezo flexure stage (Physike Instrument, Germany), the scan distance was chosen to be 200 nm between consecutive XY sections and 20 nm for z-sections to obtain PSF profiles from the fluorescent microsphere images. Therefore, the beads are used as calibration gauges to optically calibrate imaging systems and obtain better resolution.

IV.2.3 Confocal volume measurements (optical characterization)

IV.2.3.1 Numerical calculation

The correlation spectroscopy setup was characterized to determine the effective volume for FCS. We used the experimental conditions ($\lambda = 532nm$, $NA = 1.2$ and $n = 1.33$)and replaced them in the following formulas to determine the lateral waist (w_{xy}) and the axial waist (w_z):

The lateral resolution $1/e^2$ -radius of the confocal volume:

$$FWHM_{xy} = \frac{0.5\lambda_{ex}}{NA} \quad \text{(Eq.IV.1)}$$

The axial $1/e^2$ -radius of the confocal volume:

$$FWHM_Z = \frac{0.88\lambda_{ex}}{n - \sqrt{n^2 - NA^2}} \quad \text{(Eq.IV.2)}$$

We note that the term confocal volume is not identical to effective volume which will be used here as we mentioned in the following formulas:

$$V_{conf} = \left(\frac{\pi}{2}\right)^{3/2} w_{xy}^2 w_z = \left(\frac{1}{2}\right)^{3/2} V_{eff} \quad \text{(Eq.IV.3)}$$

IV.2.3.2 Experimental measurements

The determining of the effective volume (therefore the confocal volume) as the first approach is to measure the correction amplitude of a sample (Alexa Fluor 532, Life Technologies, USA) with known concentration, then the effective volume can be calculated according to:

$$V_{eff} = \frac{1}{G_0 N_A c} \quad \text{(Eq.IV.4)}$$

Where **G_0** is the correlation amplitude, **c** is the sample concentration in malar units and **N_A** is Avogadro number $6.022 \mathrm{x} 10^{23}$.

The second approach is based on the assumption that the confocal volume can be approximated by a three-dimensional Gaussian shape. By an analytical calculation, the autocorrelation function is defined as follows:

$$G(\tau) = 1 + \frac{1}{N}\left(1+\frac{\tau}{\tau_D}\right)^{-1}\left(1+\omega^2\frac{\tau}{\tau_D}\right)^{-0.5} \times \left\{1+n_T\exp\left(-\frac{\tau}{\tau_T}\right)\right\} \qquad \text{(Eq.IV.5)}$$

Where τ can be interpreted as the average time a molecule needs to transverse the confocal volume by diffusion. If the diffusion coefficient is known, the size of the confocal volume can be extracted using the following formulas:

$$w_{xy}^{2} = 4D\tau \qquad \text{(Eq.IV.6)}$$

$$V_{eff} = \pi^{3/2} k\,(4D\tau)^{3/2} \qquad \text{(Eq.IV.7)}$$

τ and k are determined by fitting the correlated data with (Eq.IV.5)

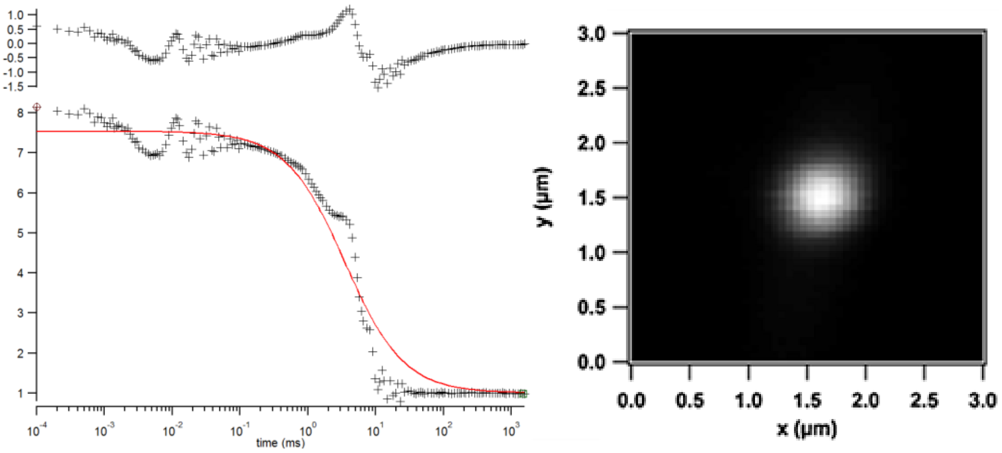

Fig.IV.3- (Left) Fluorescence correlation curve of Alexa Fluor 532 (dashed line) and the fitting curve using (Eq.IV.5) (red line). (Right) Lateral PSF image of a fluorescent bead immersed in oil obtained by fluorescence confocal microscopy.

According to the numerical application of the equation (Eq.IV.1, Eq.IV.2, Eq.IV.3 and Eq.IV.5), we get the following results:

Tab.IV.1- Dimensions of the effective volume determined by FCS and PSF from (1D Gaussian fits).

λ=532 nm	Sample	FWHM_{xy} (nm)	FWHM_z (nm)	V_{eff} (fl)
Theoretical	Water	0.192	0.527	0.108
FCS	Alexa Fluor532	0.4	1	0.894
PSF	Fluorescent bead	0.68	1.12	0.843

The results of the PSF measurements were given in **Tab.IV.1** and compared with the FCS measurements of the fluorescent solutions. Both techniques gave effective volume with low uncertainties. From the FCS measurements, a good fit is required to provide diffusion time since FCS is a method based on the statistical analysis of fluorescence fluctuations to quantify the effective volume. However, in the case of PSF, a simple direct scan of the fluorescent microspheres is sufficient to determine the effective volume.

IV.2.4 Quantitative parameters derived from the FCS

The objective of the present part is to estimate the local temperature variation at the confocal volume level by applying the FCS technique, which consists to analyze the temporal fluctuations in the fluorescence signal emitted by a small group of fluorophore molecules immersed in a viscous solution (in our case: Fluorophore + Sucrose) like a real biological medium, and then determine the impact (**Temperature × Viscosity**) factor on the resolution of the results derived from the FCS autocorrelation curve.

IV.2.4.1 Material and experimental setup

Alexa Fluor@647 Fluorophores are optical probes called Alexa (Alexa Fluor@647 (650/665) Life Technologies) with a concentration of 50 nM; 5 nM, the choice of the fluorescent molecule depends on the different chemical and physical characteristics which present a good quantum efficiency and a good resistance against photobleaching, as well as the absorbance spectrum, should be adequate with the excitation wavelength.

In order to prepare the fluorophore solution of a concentration of 20nM, the dilution series was applied using UV-Vis spectrometer (***Beer-Lambert law §chapter II 2.1.3***), the solution absorbance is plotted in **Fig.IV.4** for the different concentrations of the dilution series.

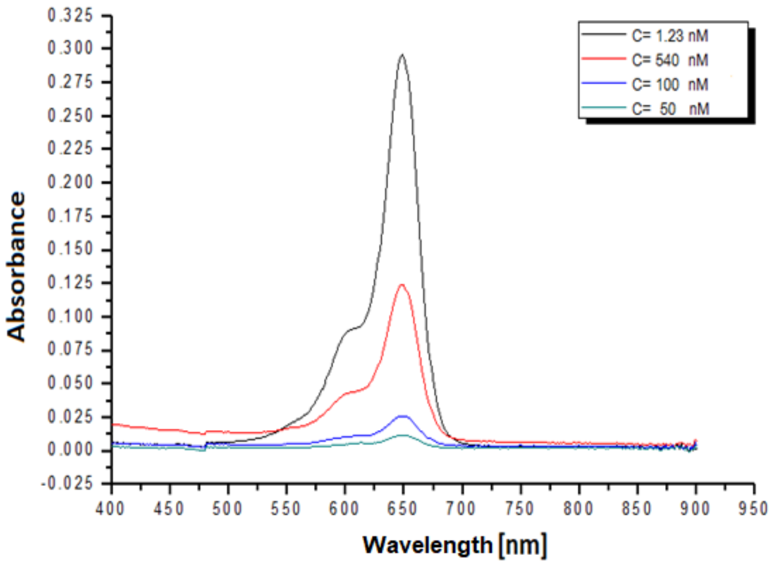

Fig.IV.4- Measurements of the AF647 concentration using the UV-Vis spectrometer.

Sucrose ≥99.5% Sigma-Aldrich: Sucrose is a disaccharide formed of a glucose molecule and a fructose molecule linked by an α(1↔2)β osidic bond. Its molecular formula is $C_{12}H_{22}O_{11}$ and its molar mass is 342.3 g mol-1.

In **Tab.IV.2**, in order to determine the viscosity of each solution, preparation of different solutions of different concentrations of sucrose was made, and subsequently, their refractive index (**Fig.IV.5**), which was measured by an Abbe refractometer.

Tab.IV.2- The viscosity of 1 mL solution as a function of the mass of sucrose.

% Suc	**0%**	**5%**	**10%**	**15%**	**20%**	**25%**	**30%**	**35%**	**40%**
C [mg/mL]	0	50.9	103.8	158.9	216.2	275.9	338.1	402.9	470.6
$\eta_{23°}$ [mPa.s]	1	1.144	1.333	1.589	1.941	2.442	3.181	4.314	6.150

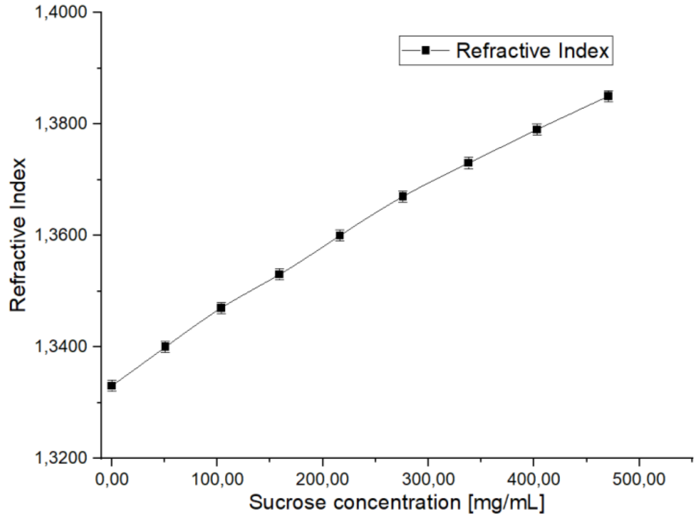

Fig.IV.5- Refractive index variation as a function of solution concentration.

Fig.IV.6 shows a laser beam, continuous, of optimal spatial quality (filtered at 633 nm), is focused through a water objective of NA 1.2 60X. A variation of 20µW was chosen as a step to see the influence of the laser intensity on the Alexa 647 (20nM) diffusion time, note that the laser intensity must not be too great so as not to saturate (photobleaching) the excitation of the fluorescence.

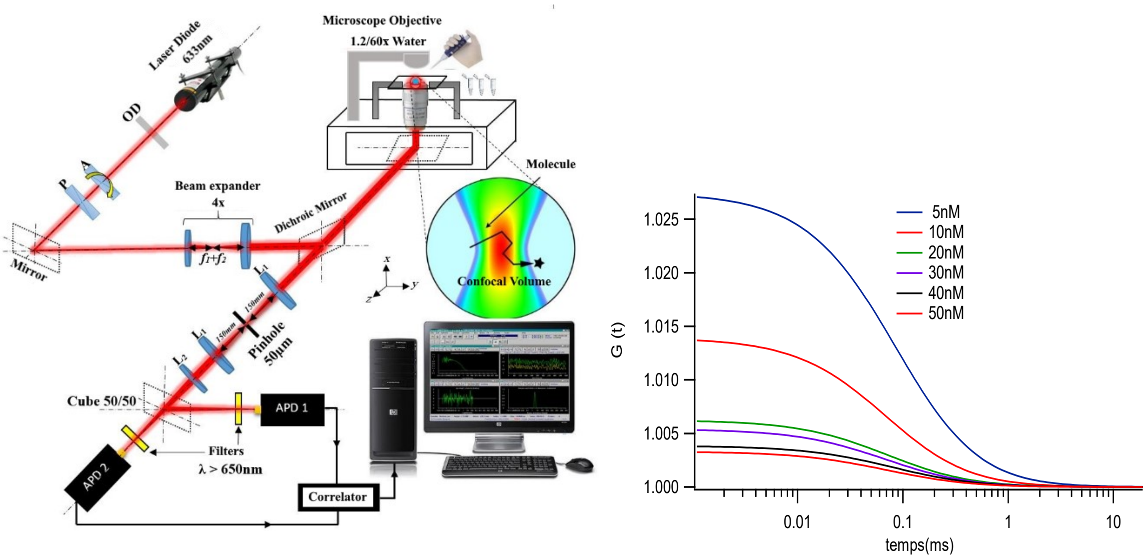

Fig.IV.6- Experimental FCS Setup.

IV.2.4.2 Approach evaluation

By a mathematical development of the equation of Stocks Einstein describes the diffusion law as follows:

$$D = \frac{k_B.T}{6\pi.\eta.R_h} \tag{Eq.IV.8}$$

With:

D is the diffusion coefficient of Alexa647 @647 D= 3,13.10^{-6} cm^2.s^{-1} at 23°C

k_β is Boltzman coefficient 1,3806504.10^{-23}J/K

T is the absolute temperature in Kelvin

η is dynamic viscosity [Pa.s]

R_h is hydrodynamic radius

The diffusion coefficient can also be calculated by this formula:

$$D = \frac{w_{xy}^2}{4.\tau_D} \tag{Eq.IV.9}$$

Therefore, from the (Eq.IV.8 and Eq.IV.9) we define a new equation that is directly related to the experimental configurations, as follow:

$$T\left(\frac{\eta_{23^\circ}}{\eta}\right) = \left(\frac{w_{xy}^2 .T_{23^\circ}}{4.D_{23^\circ}}\right).\left(\frac{1}{\tau_D}\right) \tag{Eq.IV.10}$$

So,

$$T\left(\eta_{eff}\right) = C.\left(\frac{1}{\tau_D}\right) \tag{Eq.IV.11}$$

With ***C*** is a constant which we determine it from the calibration of the FCS system (experimental setup, (λ_{Ex}=633nm, Objective NA=1.2 X60 Water immersion). As we mentioned below:

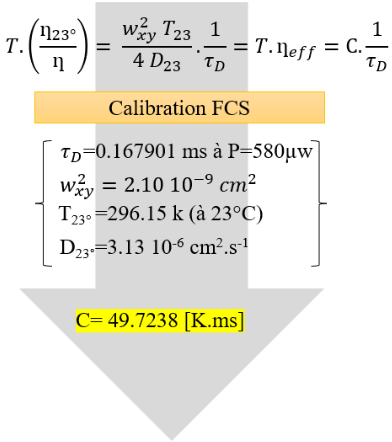

$$T.\left(\frac{\eta_{23^\circ}}{\eta}\right) = \frac{w_{xy}^2\, T_{23}}{4\, D_{23}}.\frac{1}{\tau_D} = T.\eta_{eff} = \mathrm{C}.\frac{1}{\tau_D}$$

Calibration FCS

τ_D=0.167901 ms à P=580µw

$w_{xy}^2 = 2.10\ 10^{-9}\ cm^2$

T_{23°=296.15 k (à 23°C)

D_{23°=3.13 10^{-6} $cm^2.s^{-1}$

C= 49.7238 [K.ms]

After determining the diffusion time ***τ_D*** experimentally, the evaluation of the local temperature is made by changing the intensity of the laser beam and analyzing the evolution of the factor (Temperature × Effective Viscosity).

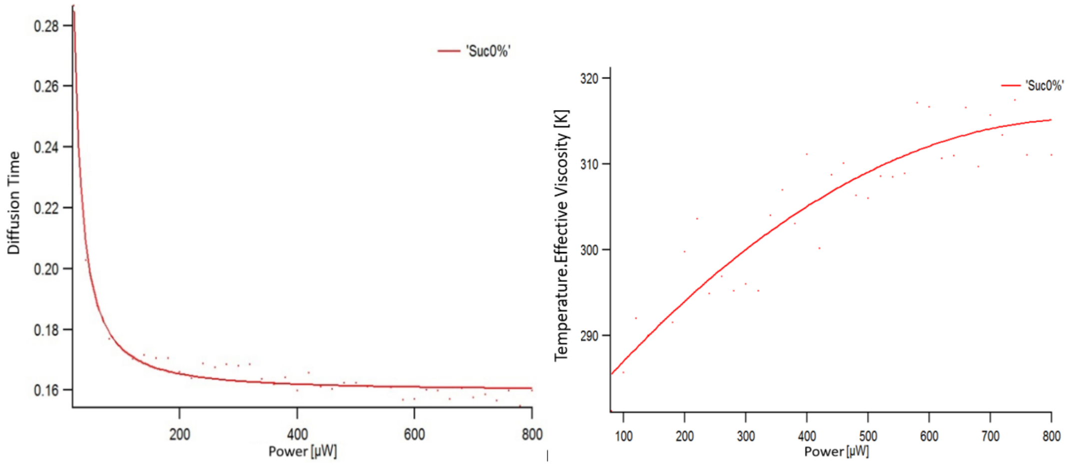

Fig.IV.7- Evolution of τ_D (left) and T (right) as a function of laser intensity.

Local temperature estimation by applying fluorescence correlation spectroscopy is an excellent technique with very high sensitivity to small changes (temperature, viscosity, concentration, kinetics, diffusion coefficient) at the confocal volume level down to a volume of femtolitre.

IV.2.5 PSF and effective medium model

The optical system of a microscope is basically diffraction-limited [1,2] and the PSF exhibits a lateral diffractive ring pattern broadening with a defocus introduced by the finite lens aperture [3–5]. The literature concerning the modeling of the PSF is extensive and several approximations are proposed with different degrees of accuracy. A particular challenge to model the PSF of a microscope concerns the absence of detailed information about the exact design of the microscope objective [6,7]. An important contribution was proposed by Gibson and Lanni [8], who developed a scalar model based on the calculation of the optical path difference OPD between experimental conditions and the microscope objective design. The PSF has been implemented in the MEX file package Matlab environment (*Appendix D*) that computes the scalar PSF model described by Gibson and Lanni [8,9]. This program is dynamically linked to subroutines that the Matlab interpreter loaded and executed. It also provides the implementation of algorithms for vectorial [6,7,10,11] and scalar [8,12] PSF models and for conventional and widefield microscopes.

In a homogeneous medium, the dielectric function is independent of the space variable and is considered as a constant at every point of the medium, which is not the case for a heterogeneous medium. Several models have been developed earlier [13–22] with some assumptions to calculate an effective dielectric function depending on the ones of the matrix and of the heterogeneities in order to describe the PSF and the response of the widefield microscopy WFM imaging. As regards the optical properties of the heterogeneous biological specimens, these heterogeneities are considered as being large in the sense that each point of the material can be associated with a macroscopic dielectric permittivity [13]. Furthermore, inhomogeneities must not exceed certain size limits. Indeed, when the size of the heterogeneities is very small compared to the wavelength of the laser light, the scattering and diffraction effects are negligible [17,18,23,24]. Hence, when the wavelength of the light wave is larger than the inhomogeneities, the macroscopic appearance of the dielectric function is respected and the medium can be characterized by an average dielectric function, which is expressed through an appropriate effective medium theory (EMT) [23]. The EMA such as the Lorentz-Lorenz, Maxwell-Garnett, Bruggeman and chemical mixture models are the most common models used to estimate the effective refractive index RI of heterogeneities in a specimen [17–19]. The combination of the effective medium approximations with the diffraction calculation helps to calculate the PSF.

So, we assume a combination of both approaches (Scalar PSF [8] and EMA [23]) in order to formulate a new specific model that aims to provide a realistic representation of the actual experimental conditions in WFM. First, we will introduce the scalar PSF on which our model is based, and give the corresponding OPD term. Subsequently, we will present the most common mathematical models of EMA. Finally, we will discuss the effects of the effective RI using various models of EMA for different setup conditions (numerical aperture (NA), immersion medium, working distance (WD), specimens, host medium, etc.) in order to propose a realistic PSF model.

IV.2.5.1 Widefield microscopy: PSF Gibson-Lanni model

The foundation of light microscopy was established a century ago by Ernst Abbe (1873, 1884). He demonstrated how the diffraction of light is obtained by a microscope objective. Hence, he determined the optical resolution laws and established the role of the numerical aperture of the microscope objective on the optical resolution [5]. Widefield optics are designed to reduce out-of-focus light and to limit the light detection to the desired plane of “in-focus” light (the object plane) [4,25,26]. Microscope objectives are designed to provide optimal imaging conditions for sources located directly below the coverslip. On the other hand, these conditions are not necessarily fulfilled for fluorescent sources that are located at a distance from the coverslip that induces higher spherical aberrations [2,27]. As conventional microscopy, WFM is limited by the light diffraction, as stated by Ernst Abbe [24]. The lateral optical resolution limit was defined for a widefield microscope with a perfect microscope objective and finite NA by the Rayleigh criterion [2,4] as:

$$R_{Lateral}^{WFM} = 0.37\frac{\lambda_{em}}{NA} \qquad \text{(Eq.IV.12)}$$

If the distance between two-point sources is lower than $\mathrm{R}_{\mathrm{Lateral}}^{\mathrm{WFM}}$ lateral, they cannot be resolved.

The commonly used axial resolution "Full Width at Half Maximum" (along with the z-axis) for the WFM configuration is given below [1,4,28]:

$$FWHM_{axial}^{WFM} = 0.885\frac{\lambda_{em}}{n_i - \sqrt{n_i^2 - NA^2}}$$

(Eq.IV.13)

with n_i the RI of the medium between the coverslip and the front lens. The factors affecting the axial resolution are the objective NA. Increasing the NA will increase the -axial- z-resolution as shown in (Eq.IV.13). Thus, with an equivalent numerical aperture and the same wavelength, a water-immersion objective will have a better resolution than an oil-immersion objective in the case of a point source located on the backside of the coverslip (at smaller depths) [3], as it will be demonstrated in the following developments. Gibson-Lanni's model expressed the PSF of an optical microscope objective using the scalar diffraction theory of light [8].

The scalar model describes the phase aberrations based on the computation of the OPD between the design and experimental conditions [6,7,10–12] (the design conditions correspond to the ones given by the manufacturer). This OPD is calculated over the three media (immersion medium/ coverslip/ object) as illustrated in **Fig.IV.8**, using the reference and experimental values for the thickness and RI. This model, despite some limitations, presents the advantage of simplicity, as it clearly considers the different components of the optical system. It can also be used to calculate the PSF of widefield/confocal microscopes [3].

The assumption made by Gibson-Lanni is that all observed aberrations are generated by external factors to the microscope objective, and therefore have their origins in the object/coverslip/immersion media combination [29,30]. In addition to the source depth-dependent mismatches/aberrations [30,31], typical factors that induce aberrations are the coverslip thickness, which may deviate up to 10% from design values, and the RI of the immersion medium, which can be sensitive to the temperature [6].

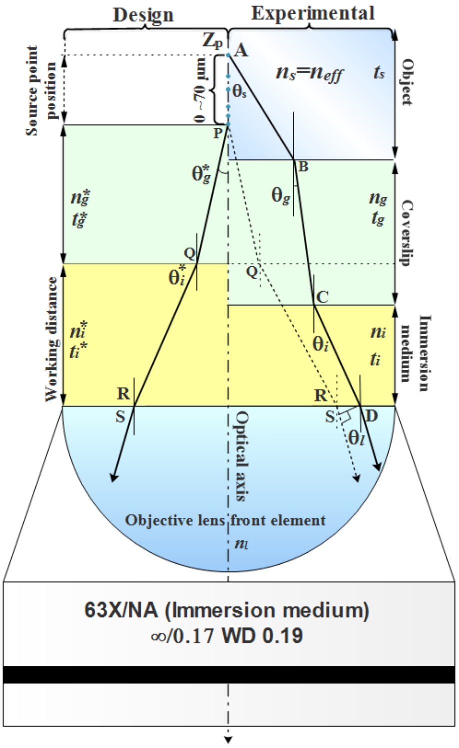

Fig.IV.8- Schematic representation of the geometric model of the path difference between two rays in the experimental system and design system.

The parameters with an asterisk (*) are valued for the design conditions of the objective lenses, those without an asterisk are the experimental ones. As shown in **Fig.IV.8**, the optical paths traced by the light rays ($\overline{\text{ABCD}}$ and $\overline{\text{PQRS}}$), originating from one on-axis point source, enter the objective lens front element in parallel at an angle θ_l . In the experimental system, the ABCD ray passes through the object (thickness t_s and RI n_s), the coverslip (thickness t_g and RI n_g) and the immersion medium (thickness t_i and RI n_i). In the design system, the object is directly below the coverslip and the PQRS ray only passes through the coverslip (thickness t_g^* and RI n_g^*) and the immersion medium (thickness t_i^* and RI n_i^*). For a constant RI n_s of the object and under the reference conditions, the optical path length is given by [3,8]:

$$\overline{PQRS} = n_g^* \frac{t_g^*}{\cos\theta_g^*} + n_i^* \frac{t_i^*}{\cos\theta_i^*} + n_l \chi, \qquad \text{(Eq.IV.14)}$$

Where;

$$\chi = \overline{\mathrm{RS}} = \sin\theta(t_s \tan\theta_s + t_g \tan\theta_g + t_i \tan\theta_i - t_g^* \tan\theta_g^* + t_i^* \tan\theta_i^*) \qquad \text{(Eq.IV.15)}$$

and for a source located at an arbitrary depth Z_p corresponding to an object layer thickness of t_s, it is equal to:

$$\overline{ABCD} = n_s \frac{Z_p}{\cos\theta_s} + n_g \frac{t_g}{\cos\theta_g} + n_i \frac{t_i}{\cos\theta_i} \qquad \text{(Eq.IV.16)}$$

The OPD Ψ is then equal to ABCD−PQRS [8] and is given by:

$$\begin{aligned}\Psi\left(\theta, z; Z_p, \tau\right) = {} & n_s \frac{Z_p}{\cos\theta_s} + n_g \frac{t_g}{\cos\theta_g} + n_i \frac{t_i}{\cos\theta_i} - n_g^* \frac{t_g^*}{\cos\theta_g^*} - n_i^* \frac{t_i^*}{\cos\theta_i^*} \\ & - n_l \sin\theta_l \left(Z_p \tan\theta_s + t_g \tan\theta_g + t_i \tan\theta_i - t_g^* \tan\theta_g^* - t_i^* \tan\theta_i^*\right).\end{aligned} \qquad \text{(Eq.IV.17)}$$

where, Z_p and z are the axial coordinates of the point source and of the focal plane respectively. The reference value for the immersion layer thickness t_i^* corresponds to the working distance of the microscope objective, which is known, $\tau = (NA, n, t)$ is the parameter set of the imaging system in which *n* is the RI, *t* is the thickness. The actual value of $t_i$is variable and depends on the focal setting of the system[6]. Therefore, it is desirable to express this parameter as a function of defocus. By identification, Gibson and Lanni define:

$$\frac{\Delta z}{n_i} = \frac{t_s}{n_s} + \frac{t_g}{n_g} + \frac{t_i}{n_i} - \frac{t_g^*}{n_g^*} - \frac{t_i^*}{n_i^*} \qquad \text{(Eq.IV.18)}$$

and consequently:

$$t_i = n_i \left[\frac{\Delta z}{n_i} + \left(\frac{t_g^*}{n_g^*} - \frac{t_g}{n_g}\right) + \left(\frac{t_i^*}{n_i^*} - \frac{t_s}{n_s}\right)\right] \qquad \text{(Eq.IV.19)}$$

Now (Eq.IV.17) can be written as:

$$\begin{aligned}\Psi\left(\rho, z; Z_p, \tau\right) = {} & \left\{Z_p - z + n_i \left(\frac{t_g^*}{n_g^*} - \frac{t_g}{n_g} + \frac{t_i^*}{n_i^*} - \frac{Z_p}{n_s}\right)\right\} \sqrt{n_i^2 - NA^2 \rho^2} + Z_p \sqrt{n_s^2 - NA^2 \rho^2} \\ & - t_i^* \sqrt{n_i^{*2} - NA^2 \rho^2} + t_g \sqrt{n_g^2 - NA^2 \rho^2} - t_g^* \sqrt{n_g^{*2} - NA^2 \rho^2}.\end{aligned} \qquad \text{(Eq.IV.20)}$$

where, *NA* is the numerical aperture of the objective, and ρ is the normalized radius, we substituted $\Delta z = z - Z_p$.

The final expression for the optical path difference OPD is then given by (Eq.IV.21) as follow:

$$\begin{aligned}
\Psi(\rho,z;Z_p,\tau) \;=\; & n_i z\sqrt{1-\left(\frac{NA\rho}{n_i}\right)^2} \\
& +n_g t_g\left(\sqrt{1-\left(\frac{NA\rho}{n_g}\right)^2}-\left(\frac{n_i}{n_g}\right)^2\sqrt{1-\left(\frac{NA\rho}{n_i}\right)^2}\right) \\
& -n_g^* t_g^*\left(\sqrt{1-\left(\frac{NA\rho}{n_g^*}\right)^2}-\left(\frac{n_i}{n_g^*}\right)^2\sqrt{1-\left(\frac{NA\rho}{n_i}\right)^2}\right) \qquad \text{(Eq.IV.21)} \\
& -n_i^* t_i^*\left(\sqrt{1-\left(\frac{NA\rho}{n_i^*}\right)^2}-\left(\frac{n_i}{n_i^*}\right)^2\sqrt{1-\left(\frac{NA\rho}{n_i}\right)^2}\right) \\
& +n_s t_s\left(\sqrt{1-\left(\frac{NA\rho}{n_s}\right)^2}-\left(\frac{n_i}{n_s}\right)^2\sqrt{1-\left(\frac{NA\rho}{n_i}\right)^2}\right).
\end{aligned}$$

The phase aberration φ (ρ, z, Z_p, τ) is obtained by multiplying the OPD with $k = 2\pi/\lambda$.

The term φ (ρ, z, Z_p, τ) represents the phase aberrations introduced by the use of the microscope objective in conditions other than those recommended by the manufacturer Carl Zeiss (called design conditions) which guarantee a minimum aberration. The PSF can then be calculated using Kirchhoff's diffraction formula [6–8] given by:

$$PSF\ (X;X_p,\tau)=\left|\mathrm{K}\int_0^1 J_0(krNA\rho)e^{i\varphi(\rho,z;Z_p,\tau)}\rho d\rho\right|^2 \qquad \text{(Eq.IV.22)}$$

where, $X=(x,y,z)$ denote the coordinates of a point in the image plane and $X_p=(x_p,y_p,Z_p)$ are the coordinates of the point source, K is the constant complex amplitude that can be obtained from the energy balance equation [11], $r=\sqrt{\left(x-x_p\right)^2-\left(y-y_p\right)^2}$ is the point at which ray intersects the exit pupil and J_0 is the Bessel function of the first kind of order zero.

The results of the PSF recorded with FluoSpheres® beads (fluorescent polystyrene latex microspheres Φ=0.170 ± 0.005 μm, which its RI is ns=1.68, and have an excitation and emission wavelengths at 506 nm and 529 nm respectively) is shown in **Fig.IV.9**.

Fig.IV.9 shows a point spread functions computed at λ=529 nm and using (Eq.IV.21) for a water-immersion objective with a NA of 1.2 ($n_i^* = 1.33$), designed to be used with a cover glass of RI $n_g^* = 1.515$ and thickness $(t_g^* = 170\mu m)$ and for point sources located at different depths of 0, 4, 10, 20, 40, and 70 µm above the cover glass in a medium of RI n_s= 1.68 (object: FluoSpheres® beads). *Appendix A* shows the various parameters used in the Gibson-Lanni approach. The calculated PSF at zero depth (Z_p = 0 µm) was performed with fluorescent microspheres attached to the coverslip.

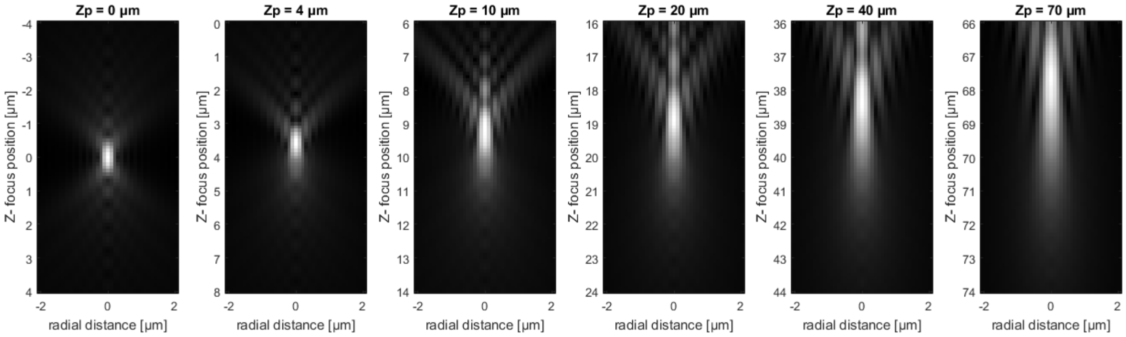

Fig.IV.9- XZ planes of PSF recorded with the water-immersion objective (NA of 1.2) generated by various depths and obtained with the Gibson-Lanni model for an object refractive index n_s=1.68.

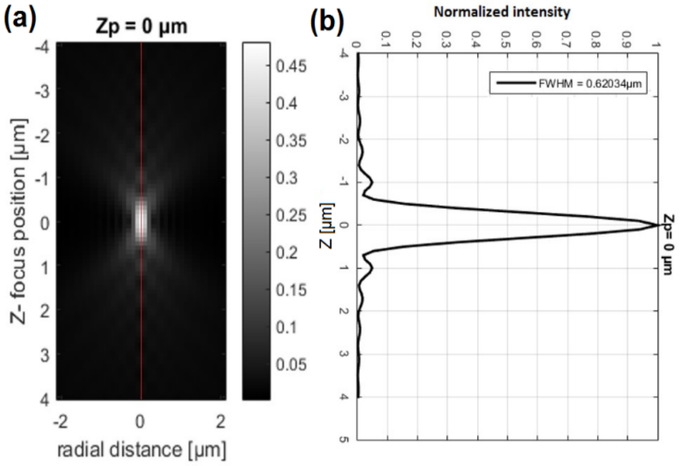

Fig.IV.10- Axial intensity profile obtained with the Gibson and Lanni model for the water immersion objective (63X, NA=1.2) at Z_p = 0 µm focusing depth: (a) 2D and (b) 1D.

Fig.IV.10 shows the corresponding axial profiles through the center of the PSF. The PSF calculated with the water-immersion objective start to be aberrated from a depth of 10 µm. The distortion of the PSF is due to the spherical aberrations that are introduced by the mismatch between the RI of the object and the one of the immersion medium of the microscope objective [29–32]. The deterioration of the resolution can be quantified by the axial full width at half maximum (FWHM) of the PSF. The calculated values of the FWHM at focusing depths of 0, 4, 10, 20, 40 and 70 µm in the object are listed in **Tab.IV.3**.

Tab.IV.3- FWHM of PSF for various focusing depths Objective 63X/NA=1.2 Water, using the Gibson-Lanni model.

Zp [µm]	0	4	10	20	40	70
FWHM [µm]	0.6203	0.6793	1.2444	1.5070	2.1079	2.6996

When the refractive indices of the immersion medium of the microscope objective and of the object are equal, the FWHM is not modified [3,10]. Spherical aberrations are introduced when there is a mismatch between the RI of the object and the immersion medium [29]. This effect further increases when focusing the light to a certain depth above the coverslip [26].

IV.2.5.2 Effective Medium Approximations (EMA)

The effective dielectric function is a macroscopic function representing the optical response of a mixed medium (microspheres in a dielectric matrix in our case) considered as a whole. In the context of the quasi-static approximation ($\lambda >> R$), the mixed medium, which is heterogeneous on a microscopic scale, can be considered to be homogeneous on a macroscopic scale, and can, therefore, be replaced by an effective medium having an effective dielectric function [18,19]. Such a composite medium can often be treated as a homogeneous medium with material constants being, in some sense, averages of the corresponding constants of its components [20]. One known approach of this kind is the self-consistent effective medium approximation [21,22,33–35] used when all the components are in the form of grains (aggregate topology of the composite).

IV.2.5.2.1 Mathematical development

The effective medium theories [17,23] can be used to describe the optical properties of the object when we have a sample consisting of a host medium (matrix) with inclusions (heterogeneities). It defines the properties of the host and of the inclusions as bulk materials [36]. The optical behavior of such EMA combinations is theoretically calculated by means of the effective medium approximations. These approximations can be Maxwell-Garnett, Lorentz-Lorenz, Bruggeman [18] or chemical mixture [36]. All these approximations can be developed starting from the following (Eq.IV.23):

$$\frac{n_{eff}^2 - n_h^2}{n_{eff}^2 - 2n_h^2} = \sum_{i=1}^{N} f_i \frac{n_i^2 - n_h^2}{n_i^2 - 2n_h^2} \qquad \text{(Eq.IV.23)}$$

Where N is the number of components, n_{eff}, n_h, and n_i are the complex refractive indices for the effective medium, the host medium and the inclusions. Note that we have not yet defined a host medium. The f_i represents the volume fractions of the inclusions (ranging from zero to one). The difference between Lorentz-Lorenz, Maxwell-Garnett and Bruggeman models is the choice of the host medium. Many models have been used to explain the effective refractive indices of the mixed medium. However, only a few of them are used. The fundamental aspects of the theory EMA have been discussed by Aspnes [14–16]. The following models are the most commonly used to estimate these effective refractive indices of mixtures of isotropic materials [17].

a. Lorentz-Lorenz model

The Lorentz-Lorenz approximation was developed to describe point polarizable entities embedded in a vacuum. Thus, the RI in the Lorentz-Lorenz model for a material of two or more components [36] can be represented by:

$$\frac{n_{eff}^2 - 1}{n_{eff}^2 + 2} = \sum_{i=1}^{N} f_i \frac{n_i^2 - 1}{n_i^2 + 2} \qquad \text{(Eq.IV.24)}$$

From (Eq.IV.24), we obtain the expression of the effective RI of Lorentz-Lorenz:

$$n_{eff}^2 = \frac{1 + 2\left(\sum_{i=1}^{N} f_i \frac{n_i^2 - 1}{n_i^2 + 2}\right)}{\left(1 - \sum_{i=1}^{N} f_i \frac{n_i^2 - 1}{n_i^2 - 2}\right)} \qquad \text{(Eq.IV.25)}$$

b. Maxwell-Garnett model

One of the earliest treatments of the mixed medium is due to Maxwell-Garnett. It assumed that dilute amounts of materials (i=1,2,3, etc.) where embedded in a large quantity of a material j so that the material j acts as a host medium. The Maxwell-Garnett [17,19] expression for the RI is:

$$\frac{n_{eff}^2 - n_j^2}{n_{eff}^2 + 2n_j^2} = \sum_{i \neq j} f_i \frac{n_i^2 - n_j^2}{n_i^2 + 2n_j^2} \qquad \text{(Eq.IV.26)}$$

The Maxwell-Garnett theory uses an infinite host medium. Therefore, this should be used for small fractions of inclusions in the host medium (for example bead solution). The Maxwell-Garnett approximation corresponds to inclusions in a host background (other than vacuum) and the quantities in (Eq.IV.23) have their obvious interpretations. In the case of a single inclusion n_1 in a single host n_h the equation becomes [17,36]:

$$\frac{n_{eff}^2 - n_h^2}{n_{eff}^2 + 2n_h^2} = f_1 \frac{n_1^2 - n_h^2}{n_1^2 + 2n_h^2} \qquad \text{(Eq.IV.27)}$$

As a result the effective RI of Maxwell-Garnett is given by:

$$n_{eff}^2 = \frac{n_h^2\left(1+2\left(f_1 \frac{n_1^2 - n_h^2}{n_1^2 + 2n_h^2}\right)\right)}{\left(1 - f_1 \frac{n_1^2 - n_h^2}{n_1^2 + 2n_h^2}\right)} \qquad \text{(Eq.IV.28)}$$

This corresponds to the Lorentz-Lorenz form if the host happens to be vacuum or air. Again, this is a good approximation if the inclusions make up a small fraction of the total volume [37]. The Maxwell-Garnett approximation thus includes the Lorentz-Lorenz model and no special support is required for the latter model.

c. Bruggeman model

Probably the most frequently used effective-medium theory is the one due to Bruggeman [21,38]. When the fractions of the host and inclusion are close, the Bruggeman approximation should be used. Bruggeman suggested making the host medium as the effective medium itself, i.e., making (n_h=n_{eff}). With this formulation, (Eq.IV.23) becomes [17,36]:

$$\sum_{i=1}^{N} f_i \frac{n_i^2 - n_{eff}^2}{n_i^2 + 2n_{eff}^2} = 0 \qquad \text{(Eq.IV.29)}$$

We limit the illustration of this model to two materials n_1, n_2 , where:

$$f_1 \frac{n_1^2 - n_{eff}^2}{n_1^2 + 2n_{eff}^2} + f_2 \frac{n_2^2 - n_{eff}^2}{n_2^2 + 2n_{eff}^2} = 0\,; \quad f_1 + f_2 = 1, \qquad \text{(Eq.IV.30)}$$

d. Chemical mixture model

The chemical mixture model is useful if the host medium and inclusions can not be treated as particles but as chemical compounds. It averages the dielectric constants by the fractions of inclusions and host. The effective RI is given by the following expression [36]:

$$n_{eff}^{2} = \frac{\sum_{i=1}^{N} f_i n_i^2}{\sum_{i=1}^{N} f_i} \qquad \text{(Eq.IV.31)}$$

IV.2.5.2.2 Models combination: Scalar PSF and EMA

For performance evaluation, we propose a PSF model that considers the aberrations due to the local variation of the RI inside a heterogeneous object by applying the various models of EMT described previously. The results were then compared to the results obtained with the Gibson-Lanni model which is already validated [8]. This latter model can be used to determine phase aberration in the experimental system due to RI mismatch (n_s/n_i) [31] and to thickness variation of the immersion medium [26]. In addition to these factors, the proposed model characterizes the phase aberration due to RI mismatch between microspheres and host medium, i.e., within the object itself. Therefore, the effective RI of the object replaces the refractive indices of both components. The aim of this work is to evaluate the Gibson-Lanni PSF model after the introduction of the effective medium approximations. To achieve this objective, we proposed a new formulation of the OPD in the (Eq.IV.21), by including the effective RI along the depth of the heterogeneous medium (polystyrene microspheres+ host medium). This effective RI n_{eff} leads to many changes in the optical path (depends on particle radius, RI and wavelength of the incident radiation...etc.) traced by the light rays. To model this, it was considered that the fluorescent microspheres are immersed in a host medium (either water n=1.33, or oil n=1.518) and that they have a RI of n_s=1.68. The adaptation of the effective RI in Gibson-Lanni model was performed by the substitution of the RI of the medium n_s in (Eq.IV.21) by an effective RI n_{eff}, calculated with the EMA mentioned previously [8]. An advantage of this approach is that it explicitly shows the RI of the host medium in the equation of the OPD proposed by Gibson and Lanni, the host medium being the environment in which the inclusions are immersed. The EMA can apply to a medium with N component. Whereas, in order to simplify the formalism, we shall give the demonstration for two components only (microspheres+ water, or microspheres+ oil). The volume fractions have been taken considering the limitations of these approximations (20% of inclusions, and 80% of host medium as optimal proportionality for applied approximations), and it assumes that all inclusion dimensions are much less than the wavelength of light. We have checked this approach in the two configurations commonly used for biological investigations (oil and water-immersion objectives).

IV.2.5.2.3 Numerical results and analysis

The implementation and simulation of the models were performed using the Matlab programming environment. This allowed us to provide images of the PSF and of the profiles which were plotted as different axial intensity curves for different microscope objectives (same excitation wavelength), and various immersion/hosts media.

Three types of microscope objectives (manufactured by Carl Zeiss [39]) have been chosen as below to trace and present the axial profiles and PSFs of this numerical study.

a) Objective Plan-Apochromat 63X/1.4 Oil M27, (WD=0.19mm at CG = 0.17mm), Immersol 518 F;

b) Objective LD LCI Plan-Apochromat 63X/1.2 Oil Corr M27, (WD=0.49mm at CG = 0.17mm), Immersol 518 F;

c) Objective C-Apochromat 63X/1.2 W Corr M27 (WD=0.28mm at CG=0.17mm), Immersol W.

Then, the RI of the host medium was defined to calculate the RI of the object using the different EMA for each setup. For each model, these parameters were defined as follows:

- *Lorentz-Lorenz model*
  - Host medium n_h=1; refractive index of microspheres n_1= 1.68, immersed in water n_2=1.33;
  - Host medium n_h=1; refractive index of microspheres n_1= 1.68, immersed in oil n_2=1.518;
- *Maxwell-Garnett model*
  - Host medium n_h=n_2=1.33 immersed in water; refractive index of microspheres n_1= 1.68.

  - Host medium $n_h=n_2=1.518$ immersed in oil; refractive index of microspheres $n_1= 1.68$.
- *Bruggeman and Chemical mixture model*
  - Refractive index of microspheres $n_1=1.68$, immersed in water $n_2=1.33$;
  - Refractive index of microspheres $n_1=1.68$, immersed in oil $n_2=1.518$;

In first step, we present the results achieved for the three types of microscope objectives used in different hosts medium.

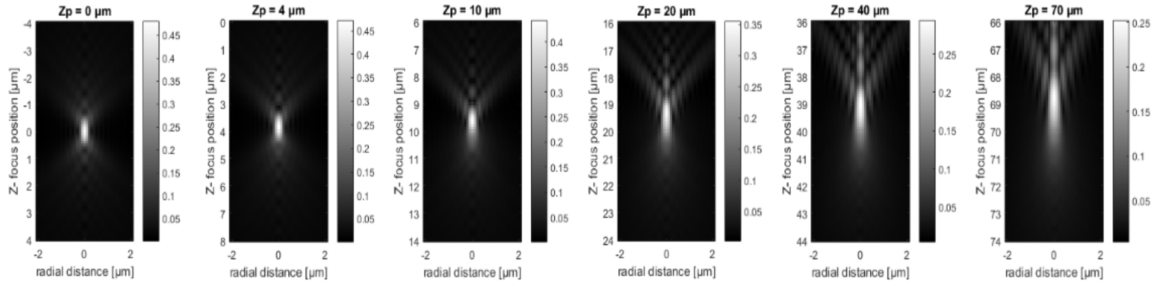

Fig.IV.11- XZ intensity profiles of PSF recorded with the water-immersion objective (NA=1.2) generated for various depths, in a sample of effective index n_{eff} given by the Lorentz-Lorenz model.

Tab.IV.4- FWHM of PSF at various focusing depths for Objective 63X/NA=1.2 Water, using the Lorentz-Lorenz model.

Zp [µm]	0	4	10	20	40	70
FWHM [µm]	0.6203	0.6506	0.6698	1.0807	1.3211	1.5777

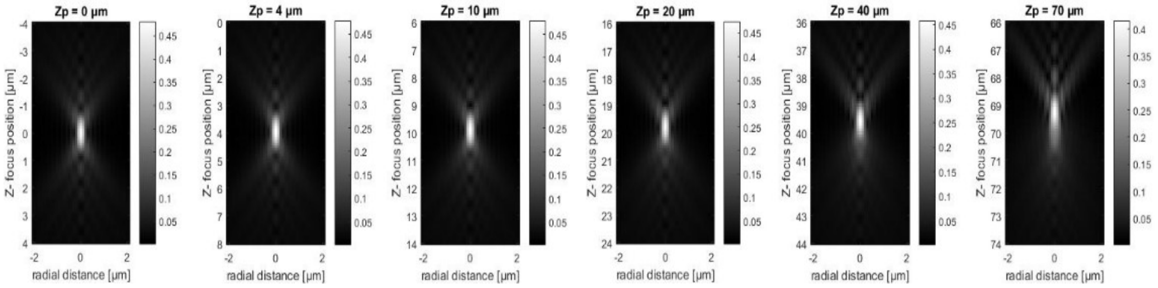

Fig.IV.12- *XZ* intensity profiles of PSF recorded with the oil-immersion objective (NA=1.2) generated for various depths, in a sample of effective index n_{eff} given by the Maxwell-Garnett model.

Tab.IV.5- FWHM of PSF at various focusing depths for Objective 63x/NA=1.2 Oil, using the Maxwell-Garnett model.

Zp [µm]	0	4	10	20	40	70
FWHM [µm]	0.7877	0.8062	0.7929	0.8012	0.8272	0.9076

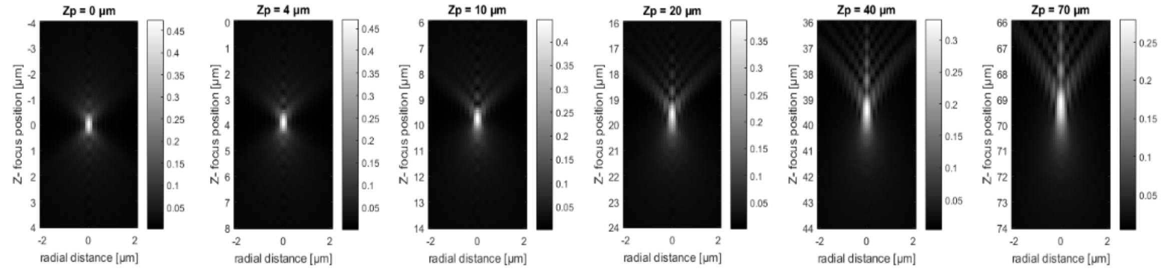

Fig.IV.13- XZ intensity profiles of PSF recorded with the oil-immersion objective (NA=1.4) generated for various depths, in a sample of effective index n_{eff} given by the Chemical mixture model.

Tab.IV.6- FWHM of PSF at various focusing depths for Objective 63X/NA=1.4 Oil, using the Chemical mixture model.

Zp [µm]	0	4	10	20	40	70
FWHM [µm]	0.5184	0.5200	0.5588	0.6999	0.8663	1.1343

Fig.IV.11, **Fig.IV.12** and **Fig.IV.13** show the evolution of the FWHM as a function of the depth for each approach of EMA with three types of microscope objectives **Tab.IV.9**, **10** and **11**. The aim is to study the influence of the mismatch between the RI of microspheres and of host medium in the object itself (heterogeneous object). Such heterogeneous medium results in a strong increase of the aberrations (loss in resolution and in signal intensity) as the point source move deeper into the object [32]. According to the calculated PSF with the different EMA, we can assume that the loss in the image resolution is the lowest when the object effective RI is closest to the RI of immersion medium of the microscope objective used. To quantify such results, we analyzed the FWHM of the PSF for each case.

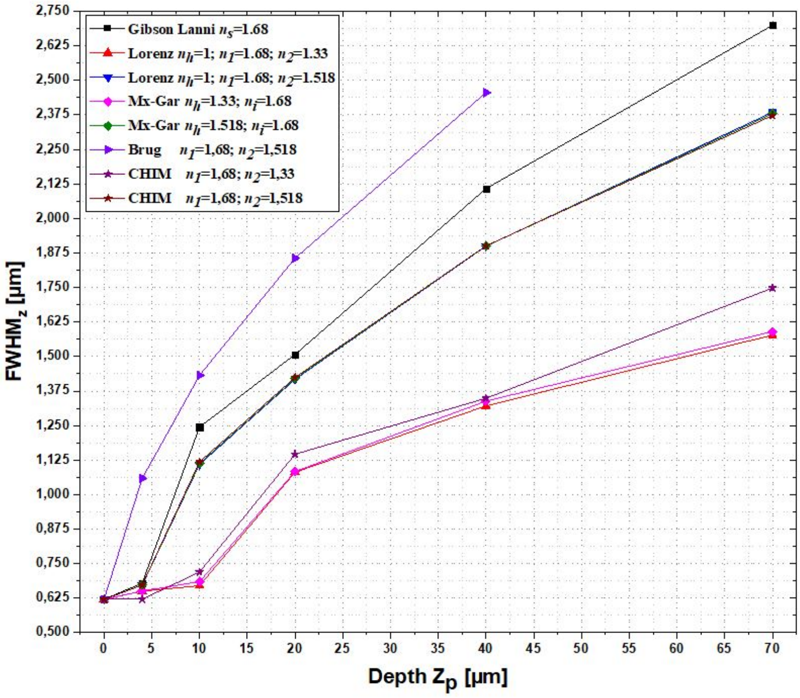

Fig.IV.14- FWHM of the PSF as a function of the depth for different effective medium models using a water-immersion 63X/NA=1.2 C-Apochromat W Corr M27 objective.

In **Fig.IV.14**, the in-depth variation of the FWHM is clearly observable. From a depth of 10µm, the PSF response exhibits a broadened and asymmetric axial FWHM which is characteristic of spherical aberrations [40,41]. As shown in **Fig.IV.14** we can observe an improvement of the resolution (decrease of the FWHM) when the Gibson and Lanni PSF model is combined with the Lorentz-Lorenz, Maxwell-Garnett and Chemical mixture models, and also when the host medium is water. For Lorentz-Lorenz (n_h=1; n_1=1.68; n_2=1.518), Maxwell-Garnett (n_h=1; n_i=1.518), and Chemical mixture (n_1=1.68; n_2=1.518) models, a superposition of curves has been noticed or each depth.

Whatever the depth was, these models still give a better FWHM than Gibson and Lanni's model. In fact, this can be justified by the decrease of the mismatch in depth between the immersion medium RI of the microscope objective and the effective RI (microspheres + host medium) developed by these latter models. On the basis of a comparison with the Gibson-Lanni results [8,29], the effective refractive indices calculated by Maxwell-Garnett, Lorentz-Lorenz and Chemical mixture models are better adapted (high dilution) for that the PSF being realistic and closest to the actual conditions. The Bruggeman model (all components involved in an asymmetrical manner) was not well adapted to our experimental setup (80% as host medium), that is why was recorded an incalculable spread from Z_p = 40 µm with the fast deterioration. The axial elongation factor was calculated with respect from Z_p = 0 µm to 70 µm depth. Under the Lorentz-Lorenz, Maxwell-Garnett and Chemical mixture models' conditions, we found a variation of 254% of the FWHM when the water is the host medium whereas this variation goes up to 384% when oil is the host medium.

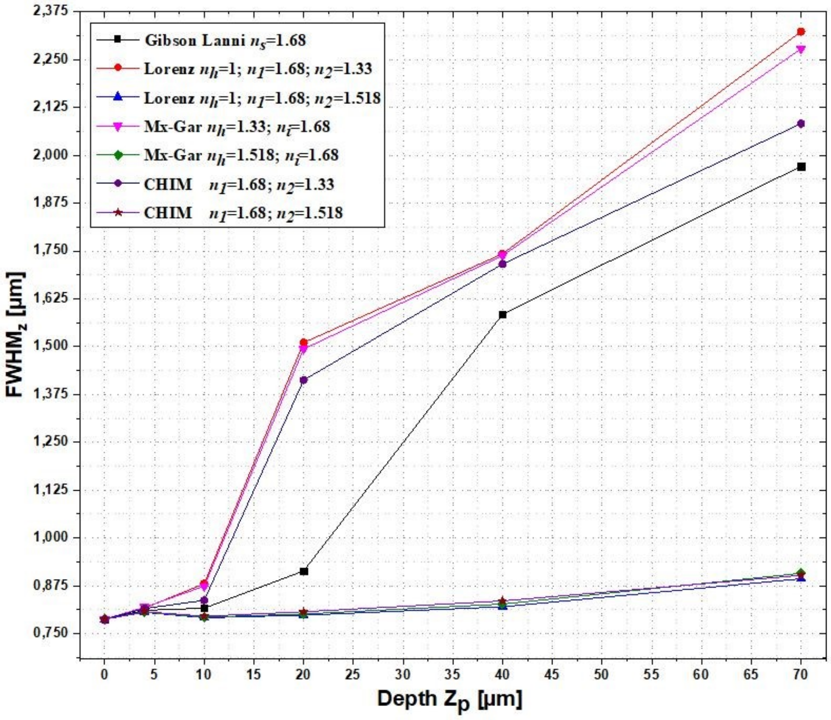

Fig.IV.15- FWHM of the PSF as a function of the depth for different effective medium models using an oil-immersion 63X/ NA=1.2 LD LCI Plan-Apochromat Oil M27 objective.

For the oil-immersion objective (NA=1.2, **Fig.IV.15**), the resolution is larger than the one calculated with the water-immersion objective (**Fig.IV.14**) for depth value below 10µm, but it has the advantage of providing a constant axial FWHM resolution (no distortion in PSFs) up to approximately 55 µm depth in the object as specified by its manufacturer that "has a high Strehl ratio, especially for Superresolution Microscopy". This time, when the inclusions (microspheres) are immersed in water, the RI mismatch effect appears and the models lose the axial resolution compared to Gibson- Lanni model. However, when the host medium is oil, a depth of Z_p = 55 µm can even be achieved with a good resolution using the Lorentz-Lorenz, Maxwell-Garnett and Chemical mixture models. As a consequence, the axial elongation factor of the FWHM, with respect to the focusing depth, ranges around 114% for the Oil as host medium, and 282% for the water as host medium. The new model results that used Gibson-Lanni model combined with the Bruggeman model have not presented above (**Fig.IV.14** and **Fig.IV.15**), because an incalculable spread from Z_p = 20 µm was found, i.e., this is extreme for Bruggeman model under these conditions (1.25 or 1.4 of NA, and 20% inclusions' volume fraction).

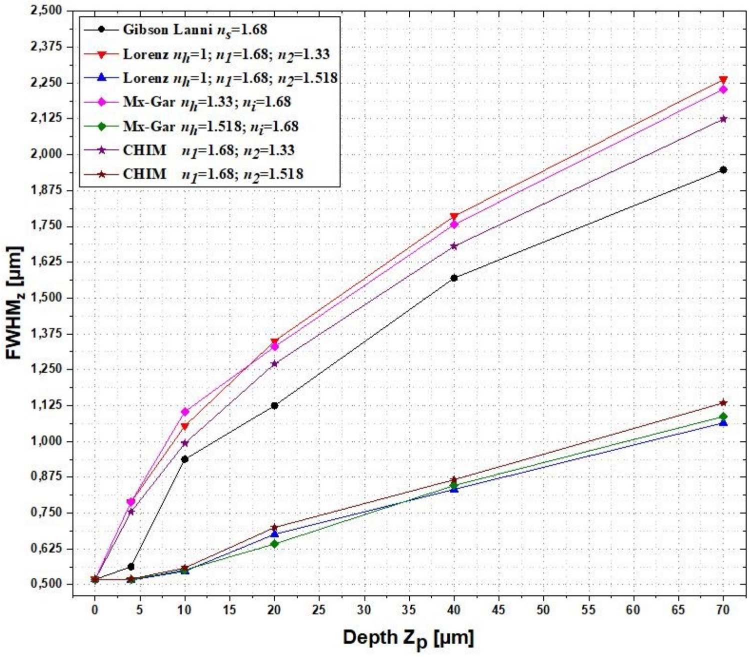

Fig.IV.16- FWHM of the PSF as a function of the depth for different effective medium models using an oil-immersion 63X/NA=1.4 Plan-Apochromat Oil M27 objective.

For the oil-immersion objective (NA 1.4, **Fig.IV.16**), we can observe a broadening of the FWHM and an asymmetric axial profile of the PSF as for the water objective (**Fig.IV.14**). Nevertheless, the FWHM is lower than 0.75µm up to 30 µm depth when the Lorentz-Lorenz, Maxwell-Garnett and Chemical mixture models have been used. Moreover, despite it presents a good resolution at the small depth, a rapid deterioration was found from 55µm comparing by the previous microscope objective (63X/1.2 NA Oil). When the effective indices developed by EMA are close to that of immersion medium RI of the microscope objective used (n_{eff}/n_i), the new approach gives the better resolution except when the immersion medium and host medium are identical and its indices close to that of the specimen under standard conditions. That is why we have found the EMA, that uses oil as a host medium for this microscope objective, has a smaller FWHM compared with the results of the Gibson-Lanni model.

At a focusing depth of 70 μm the calculated initial axial size (FWHM) of 0.51845 μm has increased by about 220% to 1.1343 μm. It is clear that the PSF and even the axial resolutions are more affected by the decrease of the reflectivity of the host medium when the focusing depth increases.

IV.2.5.2.4 Discussion

The PSF calculated by Gibson and Lanni with the water-immersion and oil-immersion objectives are clearly aberrated for depth higher than 10μm. The distortion of these PSF is due to the spherical aberrations that are introduced by the mismatch between the RI of the object and the coverslip. We have also noticed that the calculated PSF at the surface (depth 0 μm) was nearly identical for all EMA under the same numerical aperture and wavelength, which was the result of no mismatch effect of the RI (heterogeneous medium) on the PSF. Hence, this case at Z_p = 0 μm represents only the conventional microscope (no deeper imaging). In all the studied cases, the detected fluorescence intensity decreases during imaging deep and is shifted from the source point position into the object for larger depths, due to the spherical aberrations. The effect of these aberrations increases continuously for imaging deep inside the object. Furthermore, when the observed object has a different RI from one of the media, the image of each plane of the object will be affected by various aberrations thus complicating the image formation process. To solve this problem, the manufacturers have developed water or oil immersion microscope objectives. Examination of (Eq.IV.21) of the OPD showed that if the RI of the immersion medium (n_i) is equal to the RI of the object (n_s) (homogeneous specimen) and if the other experimental conditions match the recommended terms, the depth inside the object will have no more influence on the PSF. The second term is identically null whatever t_s, as a consequence, the PSF is invariant with depth. This is not the case of a heterogeneous object. Furthermore, it can be concluded that the PSF is inversely proportional to the numerical aperture since the PSF expands and the intensity decreases for a defined depth when the NA is reduced. The calculated PSF obtained using the Gibson-Lanni model combined with EMA (**Fig.IV.14**, **Fig.IV.15** and **Fig.IV.16**) is improved compared to the PSF calculated with the Gibson-Lanni model, especially for the effective medium approximations Lorentz-Lorenz, Maxwell-Garnett and Chemical mixture.

In design condition at depth $Z_p = 0$ µm, all PSFs are symmetrical with respect to z. As the depth increases the shape of the PSF becomes asymmetric. The PSF obtained using the Gibson-Lanni model is highly asymmetric, whenever there is an aberration (Non-use design conditions), this asymmetry is expected for a shift varying PSF. Therefore, the sample RI has to be taken into consideration to determine the quality of the imaging, especially for the imaging in depth of thick objects. The PSF is often measured using a fluorescent microsphere embedded in a medium that is approximated by an infinitely small point object in a homogeneous medium. However, thick biological objects are far from homogeneous. Heterogeneous refractive indices of the object can be replaced by an effective RI calculated by EMA. The structures around and in the focal plane can diffract the light and result in a PSF that deviates from the one expected in the design conditions. The proposed model presents variable performances, adaptable to the desired performance for a given application (i.e., cells, tissues...), to quantify these performances, we must consider all the parameters involved in the phase expression (see Eq.IV.22). Briefly, according to this study, we concluded that each microscope objective has its usefulness for a well-defined environment.

III.2.5.2.5 Recap

we have demonstrated that the application of EMA is useful for the modeling of the PSF in WFM and biophotonics application. We also have shown that the introduction of the effective RI provides a more realistic evaluation of the PSF in WFM. We note in particular that the PSF is limited by diffraction only under the conditions provided by the manufacturer and that the resolution of the microscope is rapidly deteriorated under other conditions, particularly due to spherical aberration. The use of the effective indices clearly improves the PSF estimation. The inclusion of the effective RI in the Gibson-Lanni model results in a model closer to the actual conditions of investigation of a heterogeneous object and induces an asymmetrical profile of the PSF. The Lorentz-Lorenz, Maxwell-Garnett and Chemical mixture models are well adapted for the modeling of the PSF in image microscopy in the case of small fractions of inclusions in the host medium.Whereas, when the fractions of the host and inclusions do not differ much (low dilution), the Bruggeman model should be used. A good knowledge of such imaging model should allow the development of specific experimental setups used to improve the axial resolution.

References

[1] J.B. Pawley, Fundamental Limits in Confocal Microscopy, in: Ed. by J.B. Pawley, Handbook Of Biological Confocal Microscopy, Springer US, Boston, MA (2006), pp. 20–42.

[2] M. Born and E. Wolf, Principles of Optics - 7th Edition.

[3] H. Olivier, "CEL - Cours en ligne - Imagerie optique microscopique en 3D: Calcul de la réponse impulsionnelle optique en microscopie de fluorescence.", MIPS - Modélisation, Intelligence, Processus et Système, Mulhouse, France (2013), pp.7–25.

[4] M. Mueller, "Introduction to Confocal Fluorescence Microscopy, Second Edition", 2 edition, SPIE Publications, Bellingham, Wash (2006).

[5] B.R. Masters, "Book Rvw: Handbook of Biological Confocal Microscopy, Second Edition. Edited by J. B. Pawley", Optical Engineering, (1996).

[6] H. Kirshner, F. Aguet, D. Sage, and M. Unser, *J Microsc*, **249**, 13–25 (2013).

[7] F. Aguet, Super-resolution fluorescence microscopy based on physical models, EPFL, 2009.

[8] S.F. Gibson and F. Lanni, *J. Opt. Soc. Am. A, JOSAA*, **9**, 154–166 (1992).

[9] F. Aguet, "Matlab MEX file: Microscope point spread function models.", Institute of Technology, Lausanne, (EPFL) (2013).

[10] H. Olivier, *OPT COMMUN*, **235**, 1–10 (2004).

[11] F. Aguet, D. Van De Ville, and M. Unser, An accurate PSF model with few parameters for axially shift-variant deconvolution - IEEE Conference Publication, in: Biomedical Imaging: From Nano to Macro. ISBI, IEEE, Paris, France (2008), pp. 157–160.

[12] H. Olivier, *OPT COMMUN*, **216**, 55–63 (2003).

[13] G.A. Niklasson, C.G. Granqvist, and O. Hunderi, *Appl. Opt., AO*, **20**, 26–30 (1981).

[14] D.E. Aspnes, *Phys. Rev. B*, **25**, 1358–1361 (1982).

[15] D.E. Aspnes, *Thin Solid Films*, **89**, 249–262 (1982).

[16] D.E. Aspnes, *American Journal of Physics*, **50**, 704–709 (1982).

[17] A. Feldman, Modeling Refractive Index In Mixed Component Systems, in: Modeling of Optical Thin Films, International Society for Optics and Photonics, (1988), pp. 129–133.

[18] A.-S. Keita, A.E. Naciri, F. Delachat, M. Carrada, G. Ferblantier, and A. Slaoui, *Journal of Applied Physics*, **107**, 093516 (2010).

[19] J.C.M. Garnett, *Phil. Trans. R. Soc. Lond. A*, **205**, 237–288 (1906).

[20] A. Wachniewski and H.B. McClung, *Phys. Rev. B*, **33**, 8053–8059 (1986).

[21] D. a. G. Bruggeman, *Annalen der Physik*, **416**, 636–664 (1935).

[22] R. Landauer, *Journal of Applied Physics*, **23**, 779–784 (1952).

[23] T.C. Choy, "Effective Medium Theory: Principles and Applications", Second Edition, Oxford University Press, Oxford, New York (2016).

[24] E. Abbe, *Archiv f. mikrosk. Anatomie*, **9**, 413–418 (1873).

[25] J.G. McNally, T. Karpova, J. Cooper, and J.A. Conchello, *Methods*, **19**, 373–385 (1999).

[26] S. Hiware, P. Porwal, R. Velmurugan, and S. Chaudhuri, Modeling of PSF for refractive index variation in fluorescence microscopy, in: 2011 18th IEEE International Conference on Image Processing, (2011), pp. 2037–2040.

[27] V.N. Mahajan, "Aberration theory made simple", Second Edition, SPIE optical engineering press, Washington, USA (2011).

[28] C.J.R. Sheppard, *Journal of Microscopy*, **149**, 73–75 (1988).

[29] D. Issaad, A. Medjahed, L. Lalaoui, M. Bouafia, M.L. de la Chapelle, and N. Djaker, *Optik*, **145**, 534–542 (2017).

[30] S. Ghosh and C. Preza, *J Biomed Opt*, **20**, 75003 (2015).

[31] A. Diaspro, F. Federici, and M. Robello, *Appl Opt*, **41**, 685–690 (2002).

[32] K. Carlsson, *Journal of Microscopy*, **163**, 167–178 (1991).

[33] A.V. Hershey, *Journal of Applied Mechanics-Transactions of the ASME*, **21**, 236–240 (1954).

[34] R. Hill, *Journal of the Mechanics and Physics of Solids*, **13**, 89–101 (1965).

[35] B. Budiansky, *Journal of the Mechanics and Physics of Solids*, **13**, 223–227 (1965).

[36] Richter Uwe., “Modeling, Simulation and Fits for enhancing discrete wavelength ellipsometers”, SENTECH Instruments GmbH, (2011).

[37] H.G. Tompkins, “A user’s guide to ellipsometry”, Courier Corporation, (2006).

[38] W. Theiß, The use of effective medium theories in optical spectroscopy, in: Ed. by R. Helbig, Advances in Solid State Physics 33, Springer Berlin Heidelberg, Berlin, Heidelberg (1993), pp. 149–176.

[39] Website:, Microscopy and Imaging, Objectives from Carl Zeiss, https://www.micro-shop.zeiss.com/?s=29770894ad989c&l=en&p=us&f=o (accessed July 21, 2017).

[40] A. Entwistle, *Journal of Microscopy*, **180**, 148–157 (1995).

[41] T. Wilson and R. Juškaitis, *Bioimaging*, **3**, 35–38 (1995).

CHAPTER V

General conclusion

V- General conclusion

In the context of the materials and structures characterization, we had a double objective, which is detailed well in the following flowchart below:

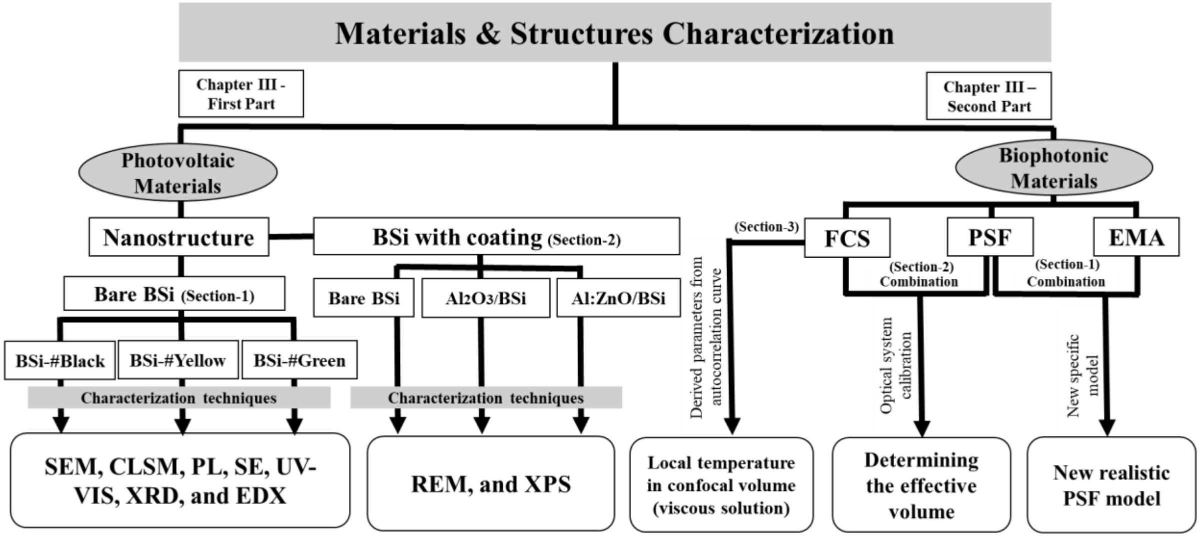

Fig.V.1- Overall project organization chart.

According to the flowchart shown above, it can be concluded that for:

- **Photovoltaic materials**

Firstly, we have introduced the materials for photovoltaic applications where silicon is the most used material then characterized it by means available and methods available at the host laboratory in CIS Erfurt, and Institut für Mikro- und Nanotechnologien MacroNano (**ZMN**) at Ilmenau Technical University of Ilmenau.

At the nanostructure scale, to increase light absorption (wider absorption band), a directed alternate deep reactive ion etching (DRIE) procedure created a nanostructured surface (black silicon) on all samples, which increases the absorption spectrum significantly (visible and infra-red) with low reflectance. It was possible to cover almost the entire visible range (400 to 800 nm) plus infra-red by simply modifying the surface structure of silicon Si (100).

The objectives of the first part concerning photovoltaic materials have been completely achieved thanks to different characterization methods (SEM, REM, CLSM, EDX, XRD, PL, UV-VIS, and XPS) which allowed us to characterize BSi samples. The electronic structure of a surface, as well as the elements and chemical bonds that exist inside it, were investigated using X-ray photoelectron spectroscopy.

Because no C-F bonds were identified in survey spectra for the black silicon sample, the procedure RIE was done by SF_6/O_2 plasma, according to the XPS data. The formation of Al:ZnO and Al_2O_3 thin films was verified by binding energy analysis.

Finally, the measurement of bandgap energies of both samples (Al:ZnO and Al_2O_3) which can be made by examining the onset of inelastic energy loss in core-level atomic spectra using X-ray photoelectron spectroscopy (XPS), will be the next task as a future work.

- Biophotonic materials

Two methods (FCS and PSF) of determining the effective volume have been investigated. All of the confocal volume methods presented can be applied. It was demonstrated that the diffusion coefficient could be measured with an accuracy of 10% using the microsphere scanning approach.

The method of selection should be determined by the sample's characteristics derived from the autocorrelation curve of FCS measurements. We carried out measurements of the fluorescence correlation spectroscopy which consists in recording for a few dozen seconds, the fluorescence emitted by a small number of molecules diffusing in a small volume of the collection which allowed us to characterize the lateral and axial resolution of the optical system (confocal microscope).

Next, we characterized the optical system with the method of the point spread function (PSF) which is a recording of a single fluorescent bead image of a smaller diameter (Φ170 nm) to the radial and axial elongations of the confocal volume.

The results obtained for the two methods (FCS) and (PSF) are in good agreement and a lateral resolution of 0.40 µm and an axial resolution of 1 µm have been achieved which leads us to volumes of the order of femtoliters.

A concrete application derived from the autocorrelation curve has been applied, which consists in determining the local temperature evolution versus light intensity (in the effective volume~ femtoliter) in a viscous solution starting with the Stokes-Einstein equation of diffusion.

It is noted that the FCS technique (determine the local temperature evolution in the confocal volume) is sensitive for less viscous solutions, as a future work to the study of the solutions with a high viscosity, the use of the technique of the dual-focus fluorescence correlation spectroscopy 2ffcs is more accurate and suitable, which is very sensitive for small temperature variations in a volume above of 270 zeptoliters (Bi-photon Microscopy technique).

Another main contribution of this work is an improved mathematical model (scalar model proposed by Gibson and Lanni) of the optical response (PSF) of the observed heterogeneous medium by integrating with the effective medium approximations (EMA), such as Lorentz-Lorenz, Maxwell Garnett, Bruggeman, and Chemical mixture models applicable for widefield microscopy.

The model of Gibson and Lanni uses the effective refraction index of the viewed object to construct the point spread function (PSF), which is expressed in terms of the optical path difference (OPD), which provides a more realistic evaluation of the PSF in widefield microscope.

Experimental perspectives

- Photovoltaic part

As a nanoscopic study, an additional characterization step for our BSi samples by the visualization with the high-resolution microscope, which allows us to calibrate dimensional measurements as well as the observation of specific areas (like needles, cross-sectional view, fluorescent microspheres, whiskers, etc.), it will give us accurate measurements that could also be compared to other characterization techniques that we have used before such as PSF (volume), REM, and SEM (depth, angle, height, roughness).

At the nanometric scale, we suggest to employing the effective medium approximation to model the optical properties of three black silicon samples (BSi-Black, Green, and Yellow) as a further work, whose black silicon will be treated as a mixture of monocrystalline silicon and air. Therefore, its effective optical constants can be correlated with the needles (nanostructure) through effective medium approximation (EMA).

Then, the study will be scaled up through an optical and electrical characterization (Sun simulator, Electroluminescence) of different manufacturing technology (monocrystalline, polycrystalline, and amorphous silicon) of photovoltaic modules (solar cells assembly), which will be carried out in collaboration with the CiS Forschungsinstitut für Mikrosensorik und Photovoltaik GmbH, SolarTestLab Laboratory, at Erfurt, Germany.

In order to develop a standardization of photovoltaic modules working in a specific operational environment (semi-humid at Erfurt-Germany, and arid at Ouargla-Algeria) by in-situ analysis of photovoltaic efficiency, it will be recommended to install the three photovoltaic modules of different technologies in different operating sites, then make a comparison between the impact of environmental conditions.

- Biophotonic part

In this perspective area, a vast study is to be done for biophotonics. Since the Metal-Enhanced Fluorescence (MEF) technique application for solutions with low molar concentration (picomolar) by local heating of the confocal volume using Urshines gold nanoparticles, will give us ideas to exploit this technique to explore the world of nano and single fluorescent molecule.

APPENDIX

Appendices

Appendix A -XRD results for 2θ and d-spacing

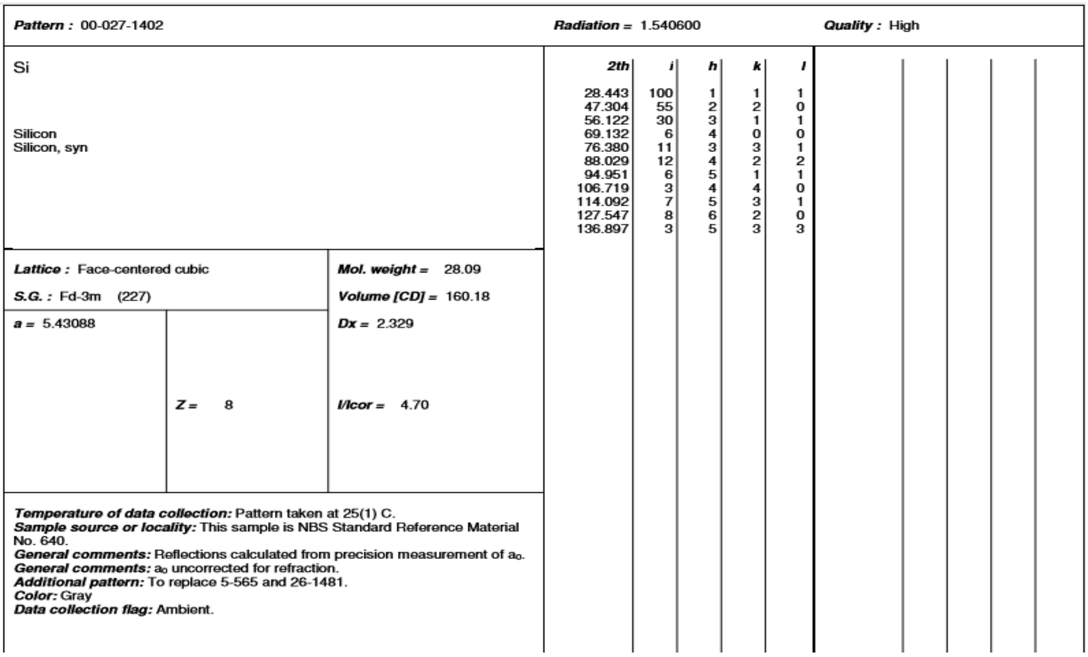

Pattern : 00-027-1402 **Radiation =** 1.540600 **Quality :** High

Si

Silicon
Silicon, syn

2th	i	h	k	l
28.443	100	1	1	1
47.304	55	2	2	0
56.122	30	3	1	1
69.132	6	4	0	0
76.380	11	3	3	1
88.029	12	4	2	2
94.951	6	5	1	1
106.719	3	4	4	0
114.092	7	5	3	1
127.547	8	6	2	0
136.897	3	5	3	3

Lattice : Face-centered cubic
S.G. : Fd-3m (227)
a = 5.43088
Z = 8
Mol. weight = 28.09
Volume [CD] = 160.18
Dx = 2.329
I/Icor = 4.70

Temperature of data collection: Pattern taken at 25(1) C.
Sample source or locality: This sample is NBS Standard Reference Material No. 640.
General comments: Reflections calculated from precision measurement of a_0.
General comments: a_0 uncorrected for refraction.
Additional pattern: To replace 5-565 and 26-1481.
Color: Gray
Data collection flag: Ambient.

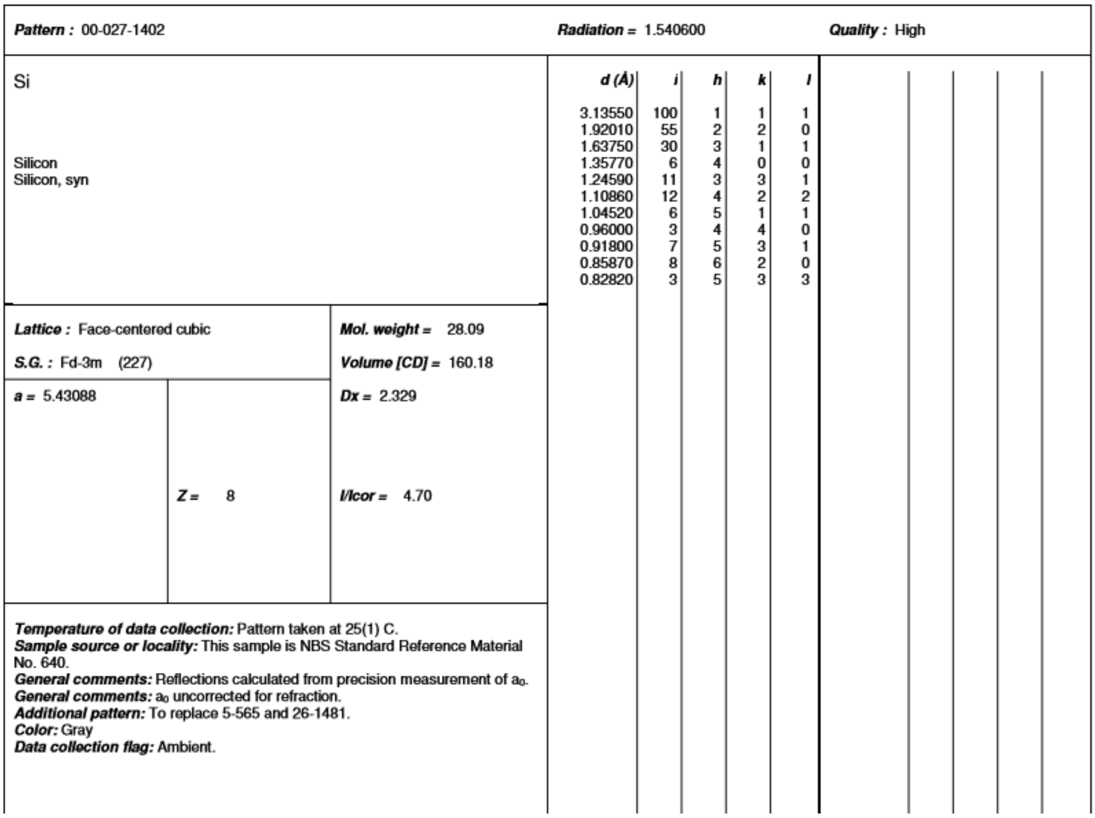

Pattern : 00-027-1402 **Radiation =** 1.540600 **Quality :** High

Si

Silicon
Silicon, syn

d (Å)	i	h	k	l
3.13550	100	1	1	1
1.92010	55	2	2	0
1.63750	30	3	1	1
1.35770	6	4	0	0
1.24590	11	3	3	1
1.10860	12	4	2	2
1.04520	6	5	1	1
0.96000	3	4	4	0
0.91800	7	5	3	1
0.85870	8	6	2	0
0.82820	3	5	3	3

Lattice : Face-centered cubic
S.G. : Fd-3m (227)
a = 5.43088
Z = 8
Mol. weight = 28.09
Volume [CD] = 160.18
Dx = 2.329
I/Icor = 4.70

Temperature of data collection: Pattern taken at 25(1) C.
Sample source or locality: This sample is NBS Standard Reference Material No. 640.
General comments: Reflections calculated from precision measurement of a_0.
General comments: a_0 uncorrected for refraction.
Additional pattern: To replace 5-565 and 26-1481.
Color: Gray
Data collection flag: Ambient.

Appendix B- PL measurements

Photoluminescence (PL) measurements were made using a blue laser at low temperature (T= -260°C) to be able to determine the concentration of the impurities (the doped materials), more precisely the concentration of the phosphorus P.

Appendices

We examined only the black and the yellow samples or the reason that we expect no new results for the investigation of the green sample, the PL spectra is shown in the following:

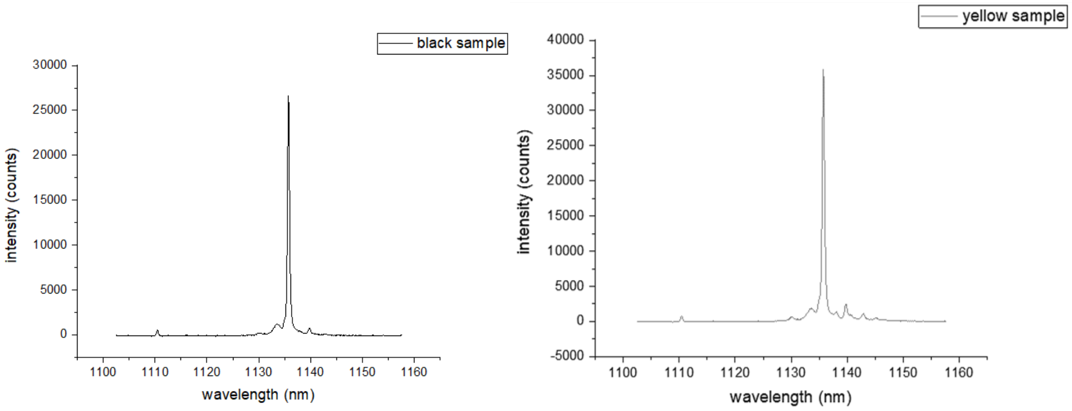

Fig.B.1- PL spectra at low temperature for the two indicated samples.

As expected, the highest peak for both the black and the yellow spectra refers to the phosphorus wavelength, because we have already said in section 1 of the experimental part, that all the samples are n-doped using the phosphorus (P). As known, the silicon wavelength is 1130 nm. The concentration of the impurities is related to the ratio between the highest intensity and the intensity of the center wavelength, which refers to the silicon wavelength. This impurity has an effect on the electronic behavior of the material by which the bandgap of the semiconductor is controllable.

Appendix C- IR Spectroscopy

In addition to the three samples used in this work, additional samples were used to properly study the behaviour of black silicon in the near-infrared (NIR) range. Sunselect and unstructured silicon samples (planner silicon) were used. The samples were examined in the infrared range (0 cm^{-1} to 800 cm^{-1}) as **Fig.C.1** shows:

Appendices

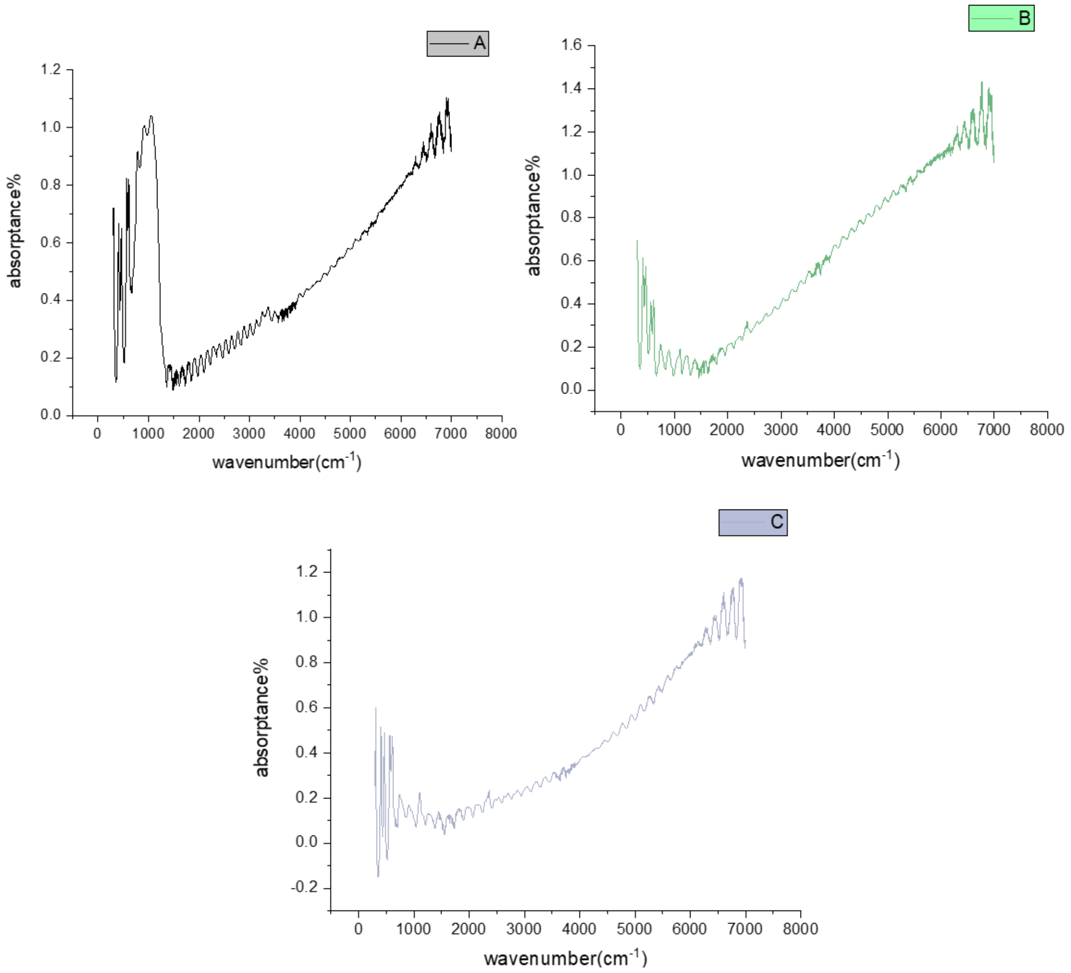

Fig.C.1- IR-Spectroscopy: (**A**)#Black sample, (**B**)#Green sample, and (**C**)#Yellow sample.

The three black silicon samples have nearly the same response, we can see the increase of absorption from the visible to the near-infrared range and this is due to the structure of B-Si samples.

Appendices

Appendix D

Parameter’s list of the MEX file package (*Scalar PSF* algorithm) to compute the Point Spread Function of a WF microscope (Objective lens C-Apochromat 63X/1.20 W Corr M27):

p.t_{i0}: 0.28	WD working distance of the objective in [mm]
p.n_{i0}: 1.33	immersion medium design refractive index
p.n_i: 1.33	immersion medium experimental refractive index
p.t_{g0}: 0.170	Cover glass design thickness in [mm]
p.tg: 0.170	Cover glass experimental thickness in [mm]
p.n_{g0}: 1.515;	Cover glass design refractive index
p.ng: 1.515;	Cover glass experimental refractive index
p.lambda: 0.000529	Fluorescence wavelength in [mm]
p.M: 63	Lateral magnification
p.NA: 1.20	The numerical aperture of the objective
p.pixelSize: 0.00645	Pixel size in image space in [mm]
nz: 81	size of the image in z (optical axis)
nxy: 41	size of the image in x and y
Z_p : [0 ~ 0.07]	position of source point in [mm]
p.sf: 3	oversampling factor to approximate the pixel integration (optional, default: 3)
p.mode: 1	(optional, default: 1)

Abstract-

The objective of this work was primarily to study the effective medium and materials through various characterization techniques (optical, structural, electronic) applied in the photovoltaic (PV) and the biophotonic (BP) domain.

The optical and electronic properties of monocrystalline Si (100) with a nanostructured surface "Black Silicon", obtained by an inductively coupled plasma (ICP) dry reactive ion etching (RIE) process in a gas mixture of SF_6 and O_2 (coated and not coated samples), were characterized using SEM, CLSM, XRD, EDX, SE, UV-Vis, PL, REM, and XPS, especially with regard to photovoltaic applications.

Thereafter, a biophotonics part is focused on optical characterization (axial resolution) of fluorescence correlation spectroscopy (FCS) configuration and widefield microscopy imaging of fluorescent molecules in a heterogeneous medium as well (effective medium). A systematic study using two different FCS methods with known (and unknown) concentration (or diffusion coefficient) has been implemented in parallel with the PSF method. So, based on the statical analysis of fluorescence fluctuations of fluorescent molecules, both FCS and PSF methods are in agreement with small uncertainties. Afterward, the optical response of the observed heterogeneous structure is modeled by a combination of the Gibson-Lanni (scalar model) and the effective medium approximations (EMA) such as Lorentz-Lorenz, Maxwell-Garnett, Bruggeman, and Chemical mixture models. The obtained results demonstrate that this model is not only effective to predict and interpret the image obtained by the widefield optical microscope but also to improve the PSF results.

Keywords: Photovoltaics (PV) materials, Biophotonics (BP) materials, Nanostructures, Black silicon (BSi), Effective medium approximations (EMA), PSF.

Résumé-

L'objectif de ce travail était principalement d'étudier les milieux effectifs et matériaux à travers différentes techniques de caractérisation tels que : caractérisation optique, structurale, électronique, appliquées dans le domaine photovoltaïque (PV) et biophotonique (BP).

Les propriétés optiques et électroniques du Si monocristallin (100) à surface nanostructuré « silicium noir », obtenu par un procédé de gravure ionique réactive sèche (RIE) plasma à couplage inductif (ICP) dans un mélange gazeux de SF_6 et O_2 (revêtu et non revêtu), ont été caractérisées par des moyens de CLSM, XRD, EDX, SE, UV-Vis, PL et SEM, en tenant compte leurs applications en photovoltaïques.

Par la suite, une partie biophotonique est basée sur la caractérisation optique (résolution axiale) de la configuration de spectroscopie de corrélation de fluorescence (FCS) et également de l'imagerie en microscopie à champ proche de molécules fluorescentes dans un milieu hétérogène (milieu effectif).

Une étude systématique selon deux méthodes différentes de FCS avec des concentrations (ou coefficient de diffusion) connus (et inconnus) a été mise en place en parallèle avec la méthode de PSF. Par la suite, la réponse optique de la structure hétérogène observée est modélisée par une combinaison de Gibson-Lanni (modèle scalaire) avec les approximations des milieux effectives (EMA) telles que Lorentz-Lorenz, Maxwell Garnett, Bruggeman et le modèle de mélange chimique. Les résultats obtenus démontrent que ce modèle est non seulement efficace pour prédire et interpréter l'image obtenue par le microscope optique à champ proche mais aussi pour améliorer les résultats de PSF.

Mots clés : Matériaux photovoltaïques (PV), Matériaux biophotoniques (BP), Nanostructures, Silicium noir (BSi), Approximations de milieu effectif (EMA), PSF.

ملخص -

يهدف هذا العمل بشكل أساسي على دراسة الوسائط والمواد الفعالة من خلال تقنيات التوصيف المختلفة مثل: التوصيف البصري، الإنشائي، الإلكتروني المطبقة في مجالات الخلايا الكهروضوئية والفوتونية الحيوية.

الخواص البصرية والإلكترونية للسيليكون أحادي البلورية (100) بسطح هيكل نانوي "السيليكون الأسود"، التي تم الحصول عليها من خلال عملية حفر الأيونات الجافة المقترنة بالحث (ICP) في خليط غازي مكون من SF_6 و2O (مغلفة وعينات غير مغلفة) باستخدام SEM، CLSM، XRD، EDX، SE، UV-Vis، PL، REM، وXPS مع مراعاة بشكل خاص تطبيقاتها في الكهروضوئية.

بعد ذلك، يتركز الجزء البصري الحيوي على التوصيف البصري (الدقة المحورية) لتكوين مطياف الارتباط الفلوري (FCS) وأيضًا التصوير بالميكروسكوب القريب من جزيئات الفلورسنت في بيئة غير متجانسة (وسط فعال).

أولاً، تم إعداد دراسة منهجية باستخدام طريقتين مختلفتين من FCS مع تركيز (معاملات انتشار) معروفة (أو غير معروفة) بالتوازي مع PSF. لذلك، بناءً على التحليل الستاتيكي لتقلبات التألق في جزيئات الفلورسنت، تتفق طريقتا FCS وPSF من حيث النتائج المتحصل عليها مع وجود نسبة خطأ صغيرة.

بعد ذلك ، يتم نمذجة الاستجابة الضوئية للبنية غير المتجانسة المرصودة من خلال مزج كل من نموذج Gibson-Lanni (النموذج القياسي) ونموذج التقريب للوسائط الفعالة (EMA) التي نذكر منها على سبيل المثال Lorentz-Lorenz ، و Garnett-Maxwell ، و Bruggeman ، و نموذج المزيج الكيميائي. توضح النتائج التي تم الحصول عليها أن هذا النموذج ليس فعالًا فقط للتنبؤ بالصورة التي تم الحصول عليها بواسطة الفحص المجهري واسع المجال وتفسيرها ولكن أيضًا لتحسين نتائج الاستجابة الضوئية PSF.

الكلمات المفتاحية: المواد الكهروضوئية (PV)، المواد الحيوية (BP)، الهياكل النانوية، السيليكون الأسود (BSi)، التقريبات المتوسطة الفعالة (EMA)، PSF.